Investigation on Different Aspects of the High-Power Coaxial Magnetron and RF Windows Operating in X-band

A

Thesis submitted

for the award of the degree of

DOCTOR OF PHILOSOPHY

By

MOHIT KUMAR JOSHI

DEPARTMENT OF ELECTRONICS AND ELECTRICAL ENGINEERING

INDIAN INSTITUTE OF TECHNOLOGY GUWAHATI

GUWAHATI - 781 039, ASSAM, INDIA

MAY 2020

Certificate

This is to certify that the thesis entitled "**Investigation on Different Aspects of the High-Power Coaxial Magnetron and RF Windows Operating in X-band**," submitted by **MOHIT KUMAR JOSHI** (146102002), a research scholar in the *Department of Electronics and Electrical Engineering, Indian Institute of Technology Guwahati*, for the award of the degree of **Doctor of Philosophy**, is a record of an original research work carried out by him under my supervision and guidance. The thesis has fulfilled all requirements as per the regulations of the institute and in my opinion, has reached the standard needed for submission. The results embodied in this thesis have not been submitted to any other University or Institute for the award of any degree or diploma.

Dated:

Guwahati.

Prof. Ratnajit Bhattacharjee
Professor
Dept. of Electronics and Electrical Engg.
Indian Institute of Technology Guwahati
Guwahati - 781 039, Assam, India.

To

Mother Nature

who has made Humankind capable of running long distances

Acknowledgements

First and foremost, I feel it as a great privilege to express my deepest and most sincere gratitude to my supervisor Prof. Ratnajit Bhattacharjee, for his excellent guidance throughout my Ph.D. tenure. My heartfelt thanks to my supervisor for his unlimited support and patience shown towards me. I sincerely thank him for scrutinizing every manuscript I presented to him and offering critical and valuable suggestions. I would like to express my gratitude to the Govt. of India, who helped me in terms of financial support during my research period. I am also thankful to Prof. R. S. Kshetrimayum and doctoral committee members for sparing time out of their busy schedule to evaluate my progress and enrich this work with their valuable suggestions and feedback. I thank Dr. Mahima Arrawatia for her suggestions in meliorating the manuscript.

I would like to acknowledge all those who provided multi-dimensional support to complete this thesis. I thank Dr. Tiwari, Program Director in charge of SAMEER Guwahati for allowing me to utilize simulation facilities of SAMEER center. I also acknowledge Dr. Sandeep Vyas, Shri Narugopal, Shri Manoj of SAMEER Guwahati for their significant help and support. The technical discussions with Dr. Vyas were really helpful. I would like to acknowledge my colleagues and friends to Dr. Deepak, Gaurav, Dr. Karam Singh, Kaushik, Ramanand, Prateek, Anoop, Arijit, Vijith, Dr. Pawan, Mohit Mishra, Rahul Sharma for their significant help and encouragement during the research.

I also acknowledge Dr. J. Medhi ("captain") and every member of Amateur Runners Guwahati (ARG), a group of enthusiastic runners for their steadfast support and inspiration. Long-distance morning runs helped me to keep myself high on peace and health. Running also helped me to channelize my thoughts and kept me more focused on my research. If nothing goes right in the labs, but surely it goes right on the roads. A morning run energies me for the day-long brainstorming time in the labs. I give my heartfelt thanks to Shri Manjil Das for his inspiration and for providing me many early morning rides to the city for participation in marathon events.

I attribute this research to my parents and friends for their altruistic encouragement. I thank the God almighty for this wonderful experience.

Mohit Kumar Joshi

Abstract

This thesis deals with various aspects of the design of megawatt-class X-band pulsed power coaxial magnetron and RF windows. X-band magnetrons have a wide range of applications such as cargo scanning, linear accelerator (LINAC) for medical application, and non-destructive testing and evaluation (NDT&E). A systematic design procedure of coaxial magnetron is presented, which includes primary sub-parts such as a coaxial cavity, anode resonator, cathode, output section, unwanted mode suppressors, and frequency tuner. The simulation studies are performed using CST Studio, and some of the results are verified by comparing with the results of HFSS simulations. The output performance of the coaxial magnetron is analyzed using particle-in-cell (PIC) simulations. Peak output power of 2.12 MW with 62.04% total efficiency is achieved for a 28-vane magnetron at 9.2987 GHz. The frequency tuning range is obtained as 9.2987 GHz $\pm$ 20 MHz.

This thesis also examines high-power overmoded RF windows in X-band. Four ingenious designs of RF windows are proposed; three windows are based on the excitation of TE_{011} mode, and one window is based on the excitation of TE_{022} mode. Multiphysics analyses are performed for the proposed RF windows. In these analyses, EM, thermal, and structural analyses are coupled together to study the temperature distribution on window dielectric and structural deformation caused by the thermal and mechanical stresses. Multipactor study of RF windows is carried out in SPARK3D, and the multipactor threshold is determined for the safe operating power level.

Next, a new approach for high-power coaxial magnetron using stacked anode resonators is proposed. A modified design of coaxial magnetron is presented with multiple anode resonators placed in a stack and multiple cathodes for high-power microwave

generation. Since the output power of the conventional coaxial magnetron (with single anode resonator) is limited, for high-power requirements, magnetron array is used. The phase-locking mechanism is essential for combining the output powers of multiple magnetrons because of their intrinsic phase inconsistency in the output signal. The proposed design enhances the output power of a coaxial magnetron substantially without requiring complex external circuitry for power combining. The modified coaxial magnetron is designed using two different arrangements of the cathodes. In one arrangement, two separate cathodes are employed with two anode resonators. This design can have two types of cathode excitation: both cathodes are excited simultaneously, and only one of the cathode is excited at a time. Three different output power levels can be obtained. In the second arrangement, both cathodes are connected. In the connected cathode arrangement, more than two anode resonators can also be employed. In the present work, the proposed magnetron configuration has been tested up to three anode resonators. The output powers of the magnetrons with double anode and triple anode resonator are found to increase about 2.73 times and 3.68 times, respectively as compared to the coaxial magnetron with a single anode resonator. A wide frequency tuning range of 30.5 MHz (from 9.2840 GHz to 9.3145 GHz) is obtained for coaxial magnetron with two anode resonators.

Contents

List of Figures

List of Tables

List of Acronyms

CAD	Computer-Aided Design
CEM magnetron	Circular Electric Mode magnetron
CST	Computer Simulation Technology
CVD	Chemical Vapor Deposition
CW	Continuous Wave
EM	Electromagnetic
HFSS	High Frequency Structure Simulator
ICEM magnetron	Inverted Circular Electric Mode magnetron
LINACs	Linear Accelerators
MW	Megawatt
NDT & E	Non Destructive Testing and Evaluation
ns	Nanosecond
PIC	Particle-in-Cell
RF	Radio Frequency
TE mode	Transverse Electric mode
TEM mode	Transverse Electromagnetic mode
TM mode	Transverse Magnetic mode
TiN	Titanium Nitride
VEDs	Vacuum Electron Devices

1

Introduction

Contents

1.1 Introduction

A magnetron is a widely used microwave frequency source for high-power applications. Although magnetron was invented almost 100 years ago, to date, the research activities in this device are continuing to improve its efficiency, extending its power and frequency range. Magnetron has high demand in multitude of applications such as LINACs, radars, cargo scanning, heating, and radiotherapy in X-band, because of its performance. LINACs are widely used in the detection and treatment of deadly diseases like cancer, scientific studies, and non-destructive testing and evaluation (NDT&E). With the availability of the commercial particle-in-cell (PIC) codes such as CST Particle Studio [4], MAGIC3D [5], in recent times, there has been renewed interest in research activities concerning efficient design of magnetrons, which can be seen from various recent publications in this domain [6–11].

In spite of a lot of progress in research and development in the field of magnetron, still there exists scopes to develop a systematic design procedure for such devices. There are a lot of interdependencies among the critical design parameters of a magnetron, and from an initial design, fine-tuning of these parameters further for obtaining targeted outputs is quite involved and time-consuming. Many designs regarding the sub-systems of a magnetron have been proposed from time to time. There are variations based on the fundamental principles of operations. High-power magnetrons operating in higher frequencies, such as X-band, have not been investigated comprehensively in the literature. RF window is a crucial component of vacuum electron devices (VEDs) and systems. High-power operation at high-frequencies requires specially designed RF windows so that multipactor, surface flashover and breakdown can be avoided for the desired operation. For this, overmoded RF windows are required to be investigated in detail in the X-band. Magnetron arrays are used for the generation of high-power microwaves from multiple magnetrons using power combining techniques. However, the output power combining is a cumbersome process because of the random phase of the output signal of a magnetron. Phase-locking techniques such as injection locking and phase-locked loop require additional complex circuitry, which makes the overall system bulky and costly. There is a scope to find the high-power microwave generation technique without complex external circuitry. The thesis

investigates in detail the various issues related to the design of high-power coaxial magnetron and its components operating in the X-band along with the high-power overmoded RF windows and output power combining technique.

1.2 Coaxial Magnetron

Military demand in the early 20^{th} century gave rise to the early stage microwave magnetrons' development. In 1921, A. W. Hull proposed the idea of the magnetron and later around 1940, multicavity cylindrical magnetron was developed by John Randall and Henry Boot at the University of Birmingham for radar application. Post World War II, magnetrons were also developed for civilian applications such as heating, radiotherapy, plasma creation. The cavity magnetron faces challenges at high-frequency operations because of reduction in dimensions.

The invention of coaxial magnetron by J. Feinstein at Bell Laboratories around 1954 is considered as major advancement in the field of cavity magnetron. Coaxial magnetron or Circular Electric Mode magnetron (CEM magnetron) overcomes the limitations of the conventional cavity magnetron. In a coaxial magnetron, a high quality-factor coaxial cavity operating in TE_{011} mode is located outside of the anode shell as shown in Fig. 1.1(a). TE_{011} mode is also known as the circular electric mode because of its circulating electric field pattern. Every alternate vane cavity of the anode resonator is coupled to the outer coaxial cavity through longitudinal slots. The circulating electric field of the TE_{011} mode provides the π-mode stability in the anode resonator by keeping the electric field in the alternate vane resonators the same. This avoids the unwanted mode jumping in the start-up time of the coaxial magnetron. The requirement of the straps is overcome in the coaxial magnetron, while that is an essential part of the conventional magnetrons for avoiding mode jumping. In a conventional magnetron, strapping and rising-sun type resonators provide mode stability when the magnetron has already reached in the desired mode but don't ensure the stability in the start-up time when competing modes may also significantly affect the desired oscillation.

Another variant of the coaxial magnetron is inverted coaxial magnetron or Inverted Circular Electric Mode magnetron (ICEM magnetron), used for the millimeter-wave frequencies applications. As the name suggested, the cathode is located outside the anode, and vane-type resonators are placed at

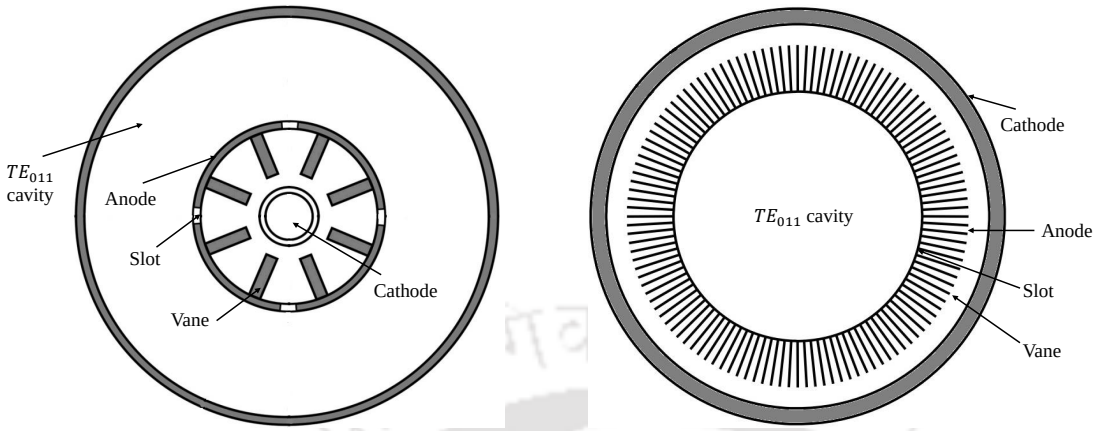

Figure 1.1: Schematic diagram (a) Coaxial magnetron (CEM magnetron) [1]. (b) Inverted coaxial magnetron (ICEM magnetron) [2].

Table 1.1: The performance characteristics of a typical coaxial magnerton and inverted coaxial magnetron [2]

Type	Freq.	No. of resonators	P_{out} (peak)	V_a	I_a	η_T	$\Delta f/f_0$
CEM magnetron	9.3 GHz	40	1.5 MW	33 kV	83 Amp	50%	10
ICEM magnetron	37.5 GHz	120	0.1 MW	23 kV	22 Amp	25%	6

the outer surface of the cylindrical cavity, as shown in Fig. 1.1(b). The inverted structure can accommodate more number of resonators. The cathode can have lower current density because of the larger radius. The output is taken axially from the circular waveguide instead of rectangular waveguide. Thus, inverted coaxial magnetron can handle more power than the coaxial magnetron. However, the efficiency of the inverted coaxial magnetron is lower. ICEM can have slot-type resonators instead of vane-type; slot-type resonators have lower quality-factor (Q) [12]. The frequency tuning range of the ICEM is lower than the CEM. The performance characteristics of a typical coaxial magnetron and inverted coaxial magnetron are presented in Table 1.1 [2].

Some of the advantages of coaxial magnetron are as follows:

☞ High-Q of the coaxial cavity provides frequency stability to the desired mode. High unloaded Q gives rise to the high loaded Q, high circuit efficiency, and thus, high total efficiency.

- ☞ Coaxial magnetron also provides *frequency agility* since it has a wide frequency tuning range.
- ☞ Lower *frequency pushing*: The change in frequency with the variation in beam current is called as *frequency pushing*. Lower interaction fields and high-Q cavity of coaxial magnetron reduces the frequency pushing [13].
- ☞ Lower *frequency pulling*: The change in frequency with the mismatch in the output load is called as *frequency pulling*. The high-Q cavity of coaxial magnetron reduces the reactive effects of the output mismatch and hence reduces frequency pushing [13].
- ☞ It can house more number of anode resonators, which leads to higher anode and cathode size as compared to the conventional magnetron. Thus, high peak output power can be obtained.

Apart from the advantages of the coaxial magnetron, the addition of the outer coaxial cavity and coupling slots also introduce the excitation of unwanted modes. The suppression of these unwanted modes is challenging and crucial for the desired operation.

1.3 RF Windows

RF window is an essential component of not only magnetron but of any vacuum electron device (VED). RF window acts as a barrier between the vacuum and the external environment in VEDs. RF window should exhibit high return loss and low insertion loss to transmit the RF power without any reflection and losses [3, 14, 15]. RF window is critical because a failure of it can damage the vacuum electron device. RF window should be made sustainable for thermal and structural stresses. Thermal expansion and pressure gradient across the dielectric disk produce structural stress in the structure.

A dielectric material is used as a barrier material in RF windows. High-purity alumina is preferred over glass because of the lower dielectric losses [1]. A window gets heated up because of its non-zero dielectric losses and give rise to failure possibilities, high dielectric losses of the dielectric disk can cause thermal run-away in a window [1]. For high-average power applications, beryllia is used as it has better thermal conductivity than alumina [16]. However, beryllia is toxic in nature. Chemical vapor deposited diamond (CVD) is also used because of its high electrical and mechanical properties

[1]. The power handling capability of an RF window is often limited by the RF breakdown caused by the multipactor discharge [17]. Multipactor effect can generate RF noise in the output signal and excess heat produced by the consistent electron bombardment can cause thermal stress in an RF window. Multipactor threshold can be enhanced by either putting an antimultipactor coating of TiN on the surface of the dielectric disk or by structural modifications. TiN coating on the dielectric surface is used to reduce the secondary electron yield (SEY), which lowers the multipactor breakdown [18]. However, the introduction of TiN coating has the disadvantage of causing surface flashover at the dielectric disk [19]. Therefore, structural modification in an RF window is an alternate way of handling both multipactor and surface flashover, where the window is operated in the overmoded condition. Overmoded RF windows are proposed to increase the diameter of the dielectric barrier, which further reduces the average power density on the dielectric disk [3, 15, 20, 21]. Apart from the design modifications, the power handling capability of the RF windows can also be enhanced by using superior dielectric materials such as CVD diamond window. CVD diamond has high thermal conductivity and negligible thermal loss and can be used for high-power applications [22, 23].

Recently, the TE_{012} mode RF window having an operating bandwidth of 5 MHz is proposed for high-power klystron [3]. RF window operating in TE_{012} mode (higher-order mode) has the advantage in terms of larger radius and lower electric field strength as compared to the conventional pillbox-type RF window. TE_{012} mode has a circulating electric field pattern along the length of the cylindrical cavity of the window. The multipactor threshold levels of such overmoded RF windows are higher even without the antimultipactor coating of TiN [3]. Another advantage of avoiding TiN coating on the dielectric surface is to overcome the possibility of surface flashover or breakdown on the coating surface. Apart from surface flashover and multipactor, there are other phenomena which limit the high-power operation of the RF windows are such as avalanche and breakdown at the dielectric of the RF window or at the metal and metal-dielectric junctions. However, the multipactor is the primary cause of the breakdown in high-power RF windows [17].

As the dielectric constant of the window disk material is high, higher-order modes can also get generated in or nearby dielectric disk because of the reduction in their cutoff frequencies. Such modes are called as ghost-modes or trapped-modes [24]. The high-electric field strength of the ghost-modes

can lead to window failure. Half-wavelength widows are much vulnerable to ghost-modes. Resonant RF windows have a narrowband operation. The bandwidth of the RF windows can be increased by the multimode operation or by introducing reactive elements [25].

1.4 Thesis Motivation and Objective

As discussed earlier, a magnetron is used as an RF source in linear accelerators (LINACs) for various applications such as radiotherapy for cancer treatment, cargo scanning, scientific study, non-destructive testing and evaluation (NDT&E) [1]. Megawatt-class magnetrons operating in X-band are in demand for portable LINAC applications because of their compact size, high efficiency, better frequency tuning range, and lightweight [26]. The design of high-power magnetron becomes challenging at high operating frequencies. At high operating frequency, geometrical dimensions decrease, and this leads to a higher possibility of voltage breakdown in a high-power conventional magnetron. Efficient heat management is needed in high-power devices for the proper operation. However, smaller dimensions of conventional magnetron have inadequate provision for the heat sink.

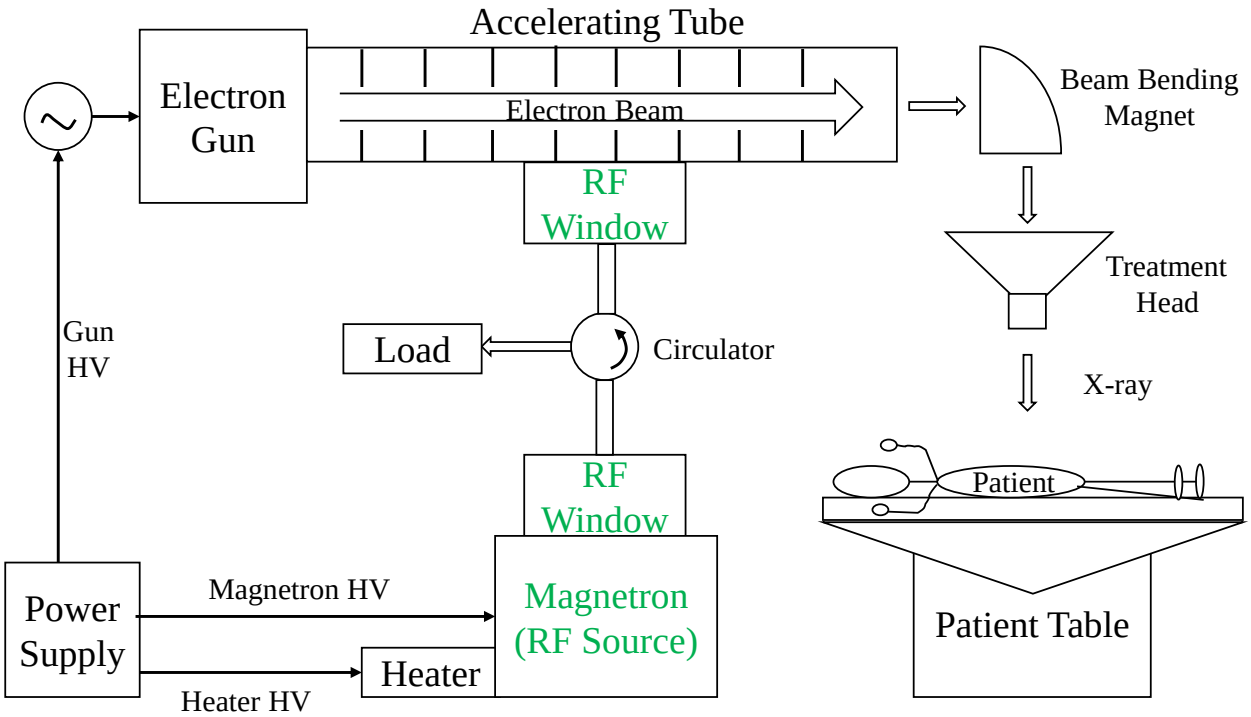

Figure 1.2: The schematic diagram of a typical medical LINAC.

Moreover, a higher quality factor (Q-factor) is desirable in magnetrons as it reduces the mode jumping and provides frequency stability for the desired mode. The quality factor (Q-factor) depends on the volume of the cavity, and the size of the cavity becomes smaller at higher frequencies in the conventional magnetron. In such situations, coaxial magnetrons are preferred over conventional cavity-type magnetrons. The coaxial magnetron has higher Q-factor because of external coaxial cavity. A systematic design procedure of megawatt-class peak output power coaxial magnetron with high-efficiency is in demand.

RF window is a critical component of magnetron as well as the LINAC system. High-power RF windows become vulnerable because of breakdown, surface flashover, and multipactor. The operating power level of the RF window is limited by the multipactor threshold. Thus, the RF window needs to be designed in such a way that it can be operated at high-power levels without multipaction at the desired frequency. Further, a wider bandwidth of the RF window can be useful for various applications. One of the application areas of the thesis work is a medical LINAC, schematic diagram of which is shown in Fig. 1.2.

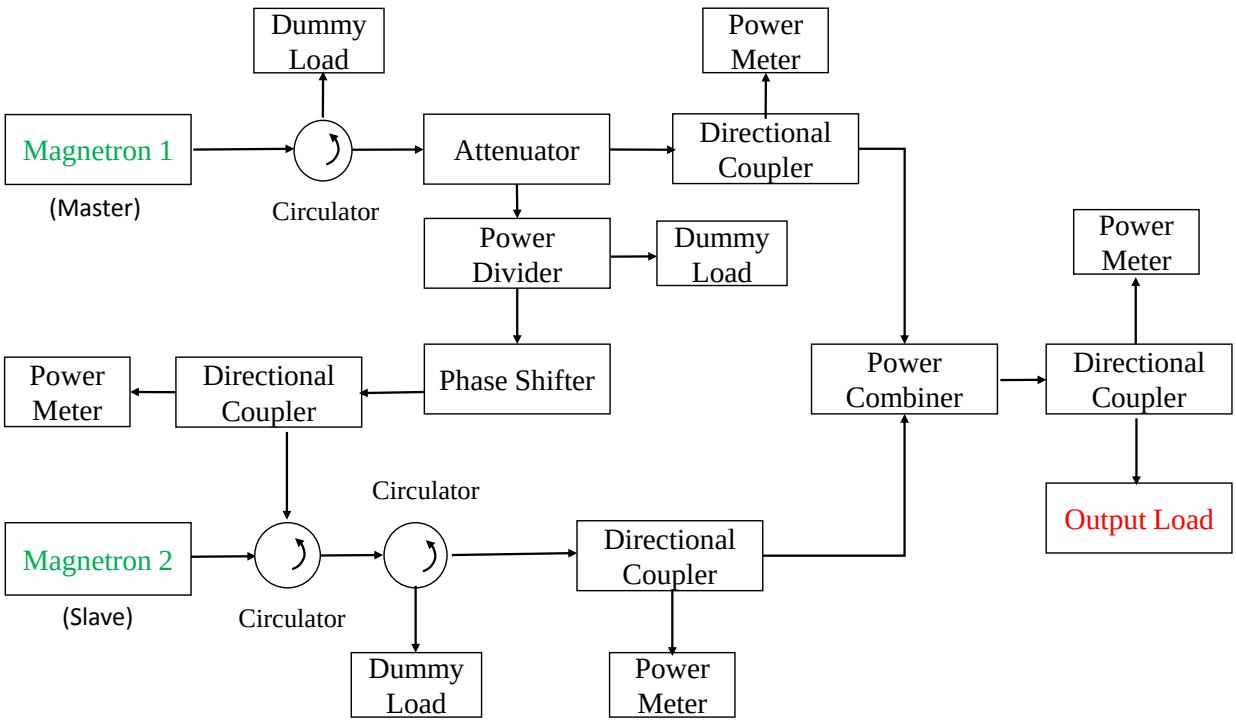

Figure 1.3: Block diagram of a typical master-slave power combining using injection-locking magnetron.

The magnetron arrays are used for high-power microwave generation. A higher output power level is achieved by combining the output powers of multiple magnetrons. Since magnetron is an oscillator with random phased output, it makes the output power combining cumbersome for the realization of magnetron arrays. Complex external circuitry is required for phase-locking. An example of master-slave power combining of two magnetrons using the injection-locking technique is shown in Fig. 1.3. The complex circuitry makes the overall system bulky and costly. There exists a scope of improving such systems by finding ways to generate high-power microwave without using external power combining techniques, at the same time keeping the system compact.

1.5 Brief Review of Literature

The conceptual design of megawatt-class magnetron is presented at the lower frequencies of 175 MHz [6] and 655 MHz [7], using conventional vane-type anode. Later on, a non-relativistic megawatt-class magnetron is developed at 912 MHz with a high-efficiency of 87% [8]. A 3D computer model of the conventional vane-type 13 kW CW magnetron operating in X-band is presented and results are compared with the experimental data [9]. A rising-sun magnetron having 250 kW power with 53% efficiency at 9.5 GHz is designed using a 3D particle-in-cell (PIC) code [10]. The design of a magnetron becomes challenging at high frequencies because of the smaller dimensions, and so, the coaxial magnetron is preferred over conventional magnetron. Strapping of vanes is not required in the coaxial magnetron and it has a stable output with reduced mode jumping because of the stabilizing outer coaxial cavity with high-quality factor.

A summary of the recent works in the non-relativistic magnetrons is presented in Table 1.2. Conventional magnetrons based on continuous wave (CW) output and pulsed power output have been investigated from 912 MHz to 10.2 GHz frequencies. A synthesis procedure of the vane type conventional magnetron is presented in [27]. However, conventional magnetrons are not preferred in X-band and applications involving higher frequencies. Coaxial magnetrons are suitable for high-frequency operations; a brief summary of the available coaxial magnetrons is presented in Table 1.3. Coaxial magnetrons operating in L-band [28] to Ku-band [29, 30] have been reported. As already mentioned, a detailed systematic procedure of design of a coaxial magnetron, including its various sub-parts, is

not readily available in literature.

Available megawatt-class pulsed power coaxial magnetrons in X-band are presented in Table 1.4. Commercial coaxial magnetrons, L6170 (L3 Technologies [39]) and VMX3095 (Communications & Power Industries Inc. [40]) are available with peak powers of 1.75 MW, and 1.5 MW, respectively. Recently, X-band pulsed power coaxial magnetrons with 40-vane are designed (in 2010 [11], and in 2019 [41]). Peak output powers are reported as 1.61 MW with 50.8% efficiency [11] and 1.88 MW with 53% efficiency [41] at 9.3 GHz. The high-power coaxial magnetron operating in X-band is not investigated adequately. It is still an active research area, and scope exists to find a systematic design procedure of the megawatt-class coaxial magnetron delivering high peak output power at high-efficiency.

As mentioned earlier, an RF window is a vital component of the vacuum electron device (VED). A brief summary of the works in RF windows is presented in Table 1.5. This includes the pillbox-type, mixed-mode, overmoded RF windows. A failure in the RF window can cause permanent damage to the VED. The exponential growth of electrons due to the multipactor discharge is one of the primary causes of the failure of RF windows; other factors are surface flashover and breakdown. Multipactor discharge limits the power handling capability of the window [42]. For high-power applications, the multipactor threshold limit can be enhanced by either putting an antimultipactor coating such as TiN coating on the surface of the dielectric barrier or by the structural modifications in the RF window. However, antimultipactor coating has disadvantage and can also cause surface breakdown or surface flashover on the dielectric disk [19].

Therefore, to overcome both multipactor and surface flashover, the structural modification technique is preferred, which is based on the overmoded operation. The overmoded RF window has larger diameter of the dielectric disk, and thereby reducing the average power density on the dielectric [3, 20, 21]. The power handling capability of RF windows can also be enhanced by employing superior dielectric materials such as CVD windows [22].

Recently, an overmoded S-band RF window based on TE_{012} mode is proposed for the high-power klystron application [3]. TE_{012} mode has the circulating electric field pattern along the length of the cylindrical cavity of the RF window. TE_{012} mode RF window has a larger radius and lower

Table 1.2: Summary of the recent works in non-relativistic magnetrons

Reference	Summary	Remarks
Ma *et al.* [9], 2003	• X-band, 9.4 GHz, 13.75 kW • MG5241 modeled in 3D MAGIC • Conventional vane-type	• Simulation results verified with available experimental data • Not preferable in X-band for high-power
Araz *et al.* [31], 2011	• X-band, 10.2 GHz, 18 Vanes • Frequency spectrum is obtained by PIC solver of CST • Conventional magnetron	• Straps are not considered • Simulation results are compared with available measured results • Not preferable in X-band for high-power
Isenlik *et al.* [32], 2013	• X-band (8.96 GHz) • 8 hole and slot type resonators • Conventional magnetron	• Systematic design procedure of hole and slot magnetron • Not preferable in X-band for high-power
Fleming *et al.* [33], 2014	• Low L-band (912 MHz), 1 MW • 14 vanes, 85% efficiency • Conventional magnetron	• Output power extraction mechanism include 6 coaxial waveguides • Not preferable in X-band for high-power
Vyas *et al.* [27], 2015	• S-band (2.45 GHz), 10 kW (CW) • 10 vanes, 71% efficiency • Conventional magnetron	• Synthesis of vane-type magnetron is presented • High-power CW magnetron
Han *et al.* [34], 2019	• L-band (1.3 GHz) • 12 hole and slot resonators, • 1.26 MW pulsed power • Conventional magnetron	• Output section includes TE_{11} to TE_{10} mode converter • Simulation is verified by measurement • Not preferable in X-band for high-power

Table 1.3: Summary of the available coaxial magnetrons in literature

Reference	Summary	Remarks
Cook *et al.* [35], 1961	• X-band, 1.5 MW pulsed power • Frequency stability is 4 times better than conventional magnetron	• Low pushing and pulling figure • High peak power at long pulse length
Bamford *et al.* [28], 1967	• L-band (1.3 GHz), 1.1 MW pulsed • 12 vanes, 40% efficiency • Low anode voltage, Light-weight	• Only inner circuit is evacuated • Large size of TE_{011} cavity at lower frequencies
Johnson *et al.* [36], 1991	• X-band, 8.6 to 9.6 GHz, 250 kW pulsed • Linear motor increases life and reliability • Improves system tuning capability	• Long life and reliability • Frequency agility • Minimized mechanical wear
Victor *et al.* [37], 2004	• X-band, 10 kW pulsed, 25% efficiency • Cold cathode arrangement	• Field emitters are used • Experimental studies performed
Blanchette *et al.* [29], 2006	• Ka-band, 32.0 GHz to 33.2 GHz • 30 kW, 20% efficiency • Inverted coaxial magnetron • VMA2054 is modeled in HFSS	• Larger cathode area • More resonators in anode shell • Long life and reliability • PIC analysis not performed
Victor *et al.* [38], 2010	• X-band, 25 kW pulsed, 41% efficiency • 30 vanes, cold cathode arrangement • Secondary emission cathode	• Field emitters are used • 3D PIC simulation performed • Compared with measured data
Song *et al.* [30], 2019	• Ka-band, 35 GHz • Asymmetrical tuning • Simulated in CST MW Studio	• Coaxial cavity studied • Tuning characteristics analyzed • For Ka-band magnetron

Table 1.4: Summary of the output performances of various available megawatt-class coaxial magnetrons in X-band

Reference	**Freq.**	**No. of vanes**	V_a	B	P_{out} **(peak)**	η_T
Lee *et al.* [41]	9.3 GHz	40	36 kV	5900 G	1.88 MW	53%
Qiu *et al.* [11]	9.3 GHz	40	41 kV	4800 G	1.61 MW	50.8%
L6170 [39]	9.275 GHz	-	38 kV	-	1.75 MW	52%
VMX3095 [40]	9.3 GHz	-	37 kV	-	1.5 MW	50.6%

electric field strength at the dielectric barrier as compared to the conventional pillbox window. The lower electric field strength at the dielectric surface reduces the breakdown possibilities, normalizes the temperature distribution and avoids localized heating. The multipactor threshold levels for such TE_{012} mode overmoded RF windows are higher even without using antimultipactor coating of TiN [3]. Another advantage of not using TiN coating in TE_{012} mode RF window is to avoid the breakdown on the coating surface or surface flashover. There is a lot of scope in the RF window design with a high multipactor threshold so that the RF window can be operated safely at high-power levels in X-band.

Output powers generated by the available pulsed power coaxial magnetrons are less than 2 MW, as presented in Table 1.4. High-power microwave is generated by power combining of multiple magnetrons in a magnetron array. Phase-locking techniques are required in the high-power magnetron arrays to make coherent sources [17, 50–55]. Power combining techniques of two pulsed power magnetrons have been introduced long before by using hybrid couplers [50]. Phase-locking of magnetrons for high-power LINACs using the injection locking technique is presented [51]. External injection phase-locking of S-band magnetrons is presented in [52, 53]. A different approach based on the quasi-locking of the slave magnetron is proposed in [54], and the power combining with phase-shifterless asymmetric injection in S-band magnetron is proposed in [17]. Recently, the phase-locking technique is also presented for millimeter-wave structures using Ka-band rising-sun magnetrons [55]. However, these phase-locking methods require complex external circuitry, including solid-state devices, hybrid couplers, and that increase the cost of the system and make the whole system bulkier. Thus, an effective power combining method is required for the high-power microwave generation without using

Table 1.5: Summary of the recent works in RF windows

Reference	Summary	Remarks
Mitiailichenko *et al.* [43], 1995	• S-band and X-band • Based on multihole couplers • Each hole is covered with dielectric	• Difficult to handle mechanical stress • Multiphysics analyses not performed • Multipactor analysis not performed
Otake *et al.* [44], 1995	• X-band, TE_{11} mode • Circular-waveguide tapers	• TiN coating at ceramic disk • Multipactor analysis not performed
Fowkes *et al.* [45], 1999	• X-band window • Overmoded window • TE_{01} mode window	• Field reduction at disk • Multiphysics analyses not performed • Multipactor analysis not performed
Tokumoto *et al.* [46], 2000	• X-band window • Mixed-mode window • TE_{11} + TE_{12} and TE_{11} + TM_{11}	• Field reduction at junction of dielectric and metal • TiN coating is used
Lamba *et al.* [47], 2008	• S-band window • Simulated results compared with measured data	• Asymmetric pill-box window • Multiphysics analyses not performed • Multipactor analysis not performed
Christie *et al.* [48], 2016	• X-band window • Single block, Multilayer, and thin disc pillbox window studied • Equivalent circuit model	• Simulation results are compared with analytical results • Multiphysics analyses not performed • Multipactor analysis not performed
Jain *et al.* [49], 2017	• S-band, pill-box window • Multiphysics analyses performed	• BeO, AlN, Al_2O_3 performance compared
Joo *et al.* [3], 2017	• S-band, TE_{01} mode • Multiphysics analyses • Compared with measured results	• TiN coating is not required • Multipactor analysis performed

complex external circuitry.

1.6 Problem Formulation

In Sections 1.1-1.3 various issues related to the design of magnetrons and RF windows are highlighted. Discussions have been made about the scopes that exist in extending the research activities in these fields. The motivations for the present work and the goals have been discussed in Section 1.4. In order to achieve these goals, key tasks, which need to be accomplished, are as follows:

- Investigation of the issues related to the improvement of the design and realization of the different parts of the coaxial magnetron.
- A systematic procedure for designing coaxial magnetron for a given specification. Improvement in the peak output power and total efficiency of the coaxial magnetron in X-band.
- Investigation of the unwanted modes such as slot modes and TE_{121} mode in the coaxial magnetron and their suppression technique.
- Investigation of the overmoded RF windows in X-band for megawatt-class applications and having a wider bandwidth.
- Method for generating high-power microwave without using the complex external mechanism for output power combining of magnetrons.

1.7 Thesis Contributions

A systematic approach for the design of a coaxial magnetron is proposed in this thesis. The work can be divided into two parts. The first part is related to the design procedure of a high-power coaxial magnetron in X-band. Such magnetrons have a wide range of applications in linear accelerators for radiotherapy, cargo scanning, and non-destructive testing and evaluation (NDT&E). In the second part of the work, high-power RF windows are designed. The proposed RF windows find application in LINAC systems, gyrotron, klystron, and magnetron. The key contributions of this thesis are as follows:

- ✓ A systematic design procedure of a coaxial magnetron is presented. This work also presents the design procedure of many sub-parts of coaxial magnetron such as a coaxial cavity, anode resonator, output section, frequency tuner, and RF window.

- ✓ A megawatt-class pulsed power 28-vane coaxial magnetron operating in X-band with high-efficiency is designed and analyzed with 3D Particle-in-Cell (PIC) simulations. Output peak power of 2.12 MW with 62.04% total efficiency is achieved at 9.2987 GHz. As shown in the literature survey (Table 1.4) that all previously reported works have output power < 2 MW around this frequency range. The output efficiency enhancement method is also introduced. A wide frequency tuning range of 9.2987 GHz $\pm$ 20 MHz is obtained in the proposed design.

- ✓ The effect of modified cathode end hats on the output efficiency of a coaxial magnetron is also presented. The introduction of conical end hats instead of conventional end hats is found to improve the total efficiency of a coaxial magnetron by 2.74%.

- ✓ Four ingenious designs of overmoded RF windows for high-power applications in X-band are proposed. The multiphysics performance analyses of the proposed RF windows are carried out using coupled EM, thermal, and structural simulation. The maximum peak power of up to 20 MW can be handled without a multipactor occurrence by the proposed RF window.

- ✓ A novel technique for high-power microwave generation from a coaxial magnetron using stacked anode resonators' arrangement is proposed in this thesis. A drastic improvement of 2.73 times and 3.68 times in the output peak powers is achieved in dual and triple anode resonators, respectively as compared to the conventional coaxial magnetron with single anode resonator without using complex external circuitry.

The modified coaxial magnetron is designed using two different arrangements of the cathodes. In one arrangement, two separate cathodes are employed with two anode resonators. This design can have two types of cathode excitation: both cathodes are excited simultaneously, and only one of the cathode is excited at a time. Three different output power levels can be obtained. In the second arrangement, both cathodes are connected. In the connected cathode

arrangement, more than two anode resonators can be employed. In this thesis, the proposed magnetron configuration has been tested up to three anode resonators.

1.8 Thesis Organization

A structural organization of the thesis is shown in 1.4. The thesis is organized into eight chapters. The brief summary of each chapter is as follows:

Chapter 1: Introduction

Background of the conventional magnetron, coaxial magnetron, and RF window is discussed in this chapter. Some of the existing works on the high-power coaxial magnetron, RF window, and

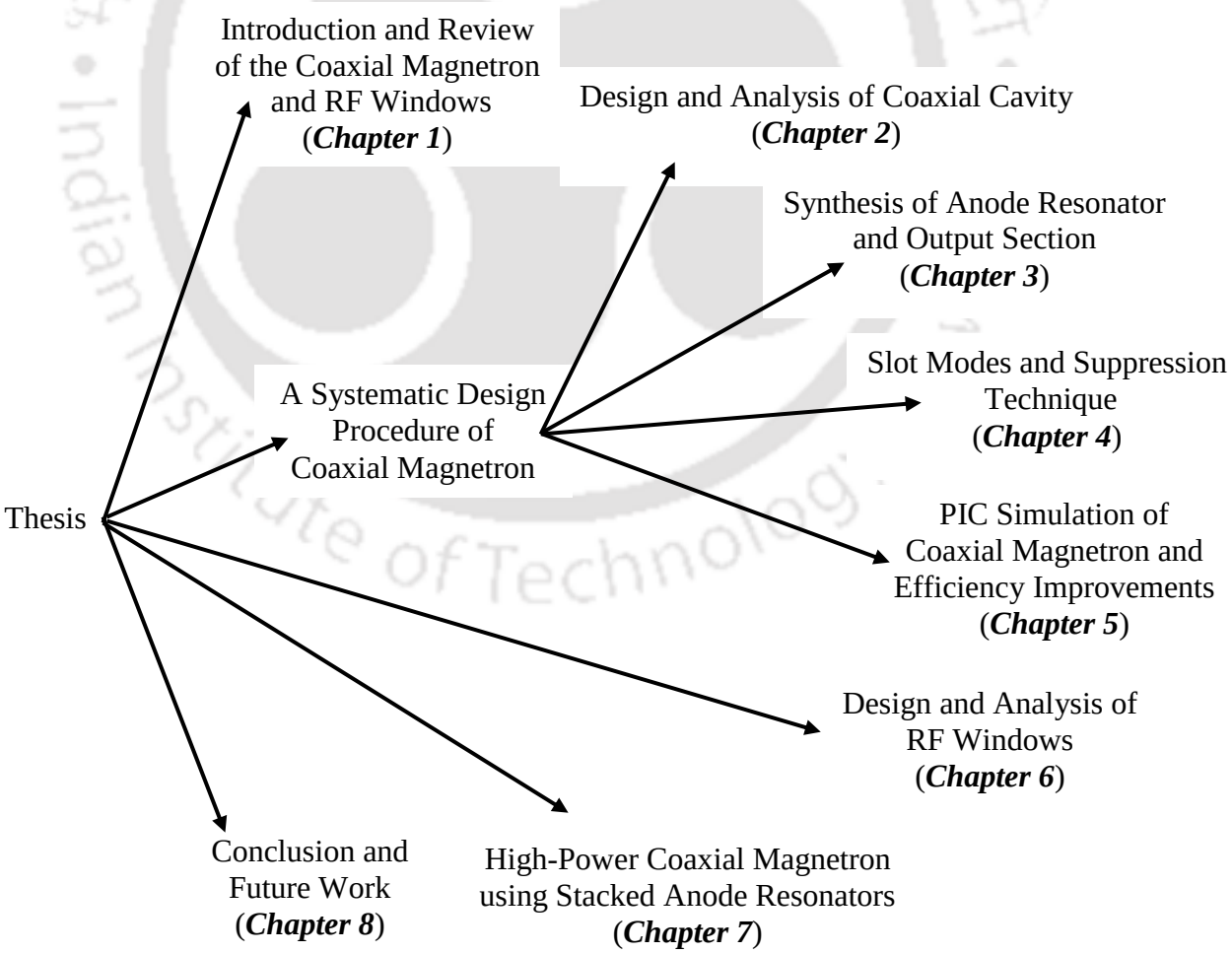

Figure 1.4: Thesis organization.

output power combining of multiple magnetrons are reviewed. The motivation and objective of the proposed thesis work are presented along with the problem identification. The summary of the thesis contribution is provided, and a chapter-wise thesis organization is presented.

Chapter 2: Design and Analysis of Coaxial Cavity

In this chapter, the design and analysis of the coaxial cavity are discussed. The expression of the quality-factor of TE_{011} mode of the coaxial cavity is derived, and synthesis of the coaxial cavity based on the maximum quality-factor is presented. The mode diagram of the proposed coaxial cavity is determined to study the occurrence of resonant modes in the coaxial cavity. The competing modes of the desired TE_{011} mode are identified. Suppression of the unwanted mode is necessary for the proper operation of a coaxial magnetron. The suppression technique of the unwanted TE_{121} mode is presented as this mode is the most likely infringing mode to the desired TE_{011} mode.

Chapter 3: Synthesis of Anode Resonator and Output Section

This chapter presents the synthesis of the anode resonator and output section of the coaxial magnetron. The cold test analysis of the proposed coaxial magnetron is carried out by performing eigenmode and frequency domain simulation. The eigenmode simulation is performed to determine the operating mode at the desired frequency, and the coupling of the coaxial magnetron is analyzed by frequency domain simulation. The dispersion diagram of the coaxial magnetron is determined.

Chapter 4: Slot Modes and Suppression Technique

In this chapter, the identification and suppression technique of the unwanted slot modes are discussed.

Chapter 5: Particle-in-Cell (PIC) Simulation of Coaxial Magnetron and Efficiency Improvements

This chapter presents the particle-in-cell (PIC) simulation of the proposed coaxial magnetron. Operating point of the magnetron is determined from the Hull-Hartree diagram. The effects of the dielectric constant and loss tangent of the slot mode suppressor on the performance of the coaxial

magnetron are analyzed by PIC simulation. The frequency tuning range of the proposed coaxial magnetron is determined. The efficiency of the magnetron is enhanced by the technique of cathode end hats' shaping.

Chapter 6: Design and Analysis of RF Windows

This chapter presents the design and analysis of RF windows. Background of the conventional pillbox-type RF window is discussed. Four designs of overmoded RF windows are proposed for high-power applications in X-band based on the excitation of TE_{012} mode and TE_{022} mode. Three designs of the overmoded RF window are presented based on the excitation techniques of TE_{012} mode, and one design based on TE_{022} mode. The performance of the proposed RF windows is studied by multiphysics and multipactor analyses.

Chapter 7: A New Approach of High-Power Coaxial Magnetron using Stacked Anode Resonators

In this chapter, a novel technique for the output power enhancement in coaxial magnetron using stacked anode resonators' approach is presented. The concept and design of a coaxial magnetron with stacked anode resonators are discussed. Two designs are proposed based on the cathode arrangements. The simulation results of both the designs are presented. Eigenmode, frequency domain, and PIC simulation are carried out to study the output performance of the proposed design. The frequency tuning range is determined. The performance of both designs is compared.

Chapter 8: Conclusion and Future Work

This chapter summarizes the proposed works in the thesis. Future work, along with the various possible applications, are discussed.

The appendices included in the thesis provide some information and studies which supplement the works presented in this thesis.

- **Appendix A**

  The solution of the wave equation for TE_{nsp} mode in the coaxial cavity is discussed.

- **Appendix B**

  The calculation of the quality factor for TE_{011} mode of the coaxial cavity is presented.

- **Appendix C**

  The design of a rectangular waveguide to cylindrical cavity mode launcher for TE_{011} mode with the maximum quality factor is presented. This mode launcher is proposed to optimize the longitudinal coupling slots present in the intervening wall of the anode cavity and outer coaxial cavity.

- **Appendix D**

  Computational information such as number of mesh cells, number of emission points, computational time, and computational platform specifications are presented.

- **Appendix E**

  For the feasibility of fabrication, CAD designs of the proposed RF windows and the impact of tolerance of position and radius of the inductive coupling post are discussed.

2

Design and Analysis of Coaxial Cavity

Contents

This chapter presents the synthesis and analysis of a coaxial cavity for high-power X-band coaxial magnetron. The coaxial cavity is an essential part of a coaxial magnetron. Two methods, namely method 1 and method 2, are presented for determining coaxial cavity design parameters: method 1 is based on solving characteristic equation for the TE mode and the method 2 is based on the quality factor maximization. Since high-quality factor is required in the coaxial magnetron, second method is preferred for determining dimensions of the coaxial cavity. The quality factor of the coaxial cavity for the desired TE_{011} mode is obtained analytically and verified by CST [4] and HFSS [56] simulations. Resonant frequencies of various competing modes (such as TE_{121}, TE_{221}, *etc*.) of the operating TE_{011} mode are also determined and shown using a mode-diagram. The suppression mechanism of the unwanted mode is also discussed. The dominant interfering mode, TE_{121}, is suppressed considerably using an auxiliary cavity filled with the lossy dielectric material.

2.1 Introduction

The design of a magnetron with high output power operating at high frequency is a very challenging task because of the reduction in the geometrical dimensions of the device with the increase in the operating frequency [14]. Smaller dimensions lead to voltage breakdown in a conventional high-power magnetron. Smaller dimensions have poor provision for the heat sink. The efficient heat management is a major requirement in high-power devices. Moreover, a higher quality factor is desirable for magnetrons as it provides frequency stability and reduces the mode jumping. Quality factor depends on the volume of the cavity, which becomes very small at higher operating frequencies. In such situations, coaxial magnetrons are preferred over conventional magnetrons [14]. A coaxial magnetron having an outer cavity attached to the anode of the conventional magnetron stores energy and hence, enhances the quality factor (Q) of the device [14]. Coaxial magnetron can support a large number of resonators, and that increases the space charge region between cathode and anode, which further reduces the chances of voltage breakdown.

Recently, investigations of magnetrons based on the simulation techniques have been reported in the literature [11, 32, 57]. Anode cavities of the conventional magnetron have also been analyzed analytically [58]. However, analytical study and systematic design procedure of a coaxial magnetron

have not been dealt adequately in the literature. Synthesis of the outer coaxial cavity is vital for the design of a coaxial magnetron. The systematic design procedure of a outer coaxial cavity operating in TE_{011} mode is presented in this chapter. Two methods of the coaxial cavity synthesis are presented in this chapter. In the first method, the dimensions of a coaxial cavity are determined by solving the transcendental characteristic equation for the TE mode. The second method is based on the quality factor (Q) maximization. It may be noted that in this chapter, maximization of unloaded Q of the coaxial cavity has been considered. The coaxial cavities designed based on method 1 and method 2 are represented by *design 1* and *design 2*, respectively. Q calculated from the analytical technique is compared with the results obtained from CST and HFSS simulations. Q-factors of the coaxial cavities for *design 1* and *design 2* are compared. The resonant frequencies of competing modes (neighboring modes) of desired TE_{011} mode have been calculated analytically, and verified with the simulation results of CST. The occurrence of consecutive modes has been presented in the form of a mode diagram. This chapter also presents the unwanted mode suppression technique in which quality factors of the unwanted modes are reduced.

This chapter is organized into seven sections. Field analysis of the outer coaxial cavity is discussed in Section 2.2. In this section, determination of the generalized TE mode fields and from that TE_{011} mode fields are determined. The synthesis of the coaxial cavity based on method 1 is presented in Section 2.3. Design of the outer coaxial cavity based on the quality factor maximization technique (method 2) is presented in Section 2.4. In this section, Q-factor of *design 1* (based on method 1), is compared with the optimal design technique, *design 2* (based on method 2). Significant improvement is achieved in Q-factor of TE_{011} mode in coaxial cavity. The proposed *design 2* approach is more systematic than *design 1*. Analytical results are verified with the results obtained from CST and HFSS simulations for both designs. Resonant frequencies of the competing modes (neighboring modes) of the desired TE_{011} mode are determined analytically and verified with the results obtained from CST simulation in Section 2.5. In Section 2.6, suppression technique for unwanted TE_{121} mode (most interfering mode of the desired TE_{011} mode), based on the Q-factor reduction is presented. Section 2.7 concludes this chapter. Solution of wave equation for TE_{nsp} mode in a coaxial cavity and calculation of Q-factor of TE_{011} mode is presented in Appendix A, and Appendix B, respectively for

the sake of completeness.

2.2 Field Analysis of Coaxial Cavity

A coaxial cavity is formed when a section of coaxial transmission line is short-circuited at both the ends. An axial cross-sectional view of the coaxial cavity is shown in Fig. 2.1. The coaxial cavity has three design parameters; inner radius (a), outer radius (b), and length (l), as shown in Fig. 2.1. The coaxial cavity length is assumed to be in the z-direction for this analysis. In order to determine fields of the desired TE_{011} mode of the coaxial cavity, field analysis for generalized TE modes is carried out in this chapter. Although field analysis for coaxial transmission lines for higher-order modes is available in the literature [59, 60], the analysis for the coaxial cavity is presented here briefly. The field solution of TE_{011} mode is also available in [61].

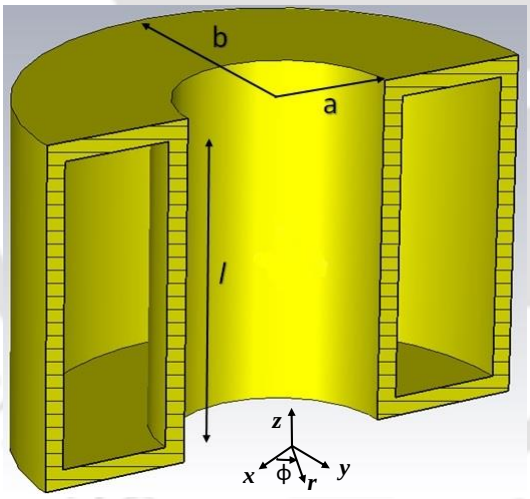

Figure 2.1: Cross-sectional view of a coaxial cavity.

For TE modes, the electric field component $E_z = 0$ and the magnetic field component H_z satisfies the wave equation. This can be expressed as [59]:

$$\left[\nabla^2 + k^2\right] H_z = 0, \tag{2.1}$$

where k is the wavenumber of the coaxial cavity.

Fields of TE_{nsp} mode can be expressed as:

$$E_r = \frac{jn\omega\mu A_0}{k_c^2 r}\left[J_n(k_c r)Y_n'(k_c a) - J_n'(k_c a)Y_n(k_c r)\right]\sin(n\phi)\sin(\frac{p\pi}{l}z), \tag{2.2}$$

$$E_\phi = \frac{j\omega\mu A_0}{k_c}\left[J_n'(k_c r)Y_n'(k_c a) - J_n'(k_c a)Y_n'(k_c r)\right]\cos(n\phi)\sin(\frac{p\pi}{l}z), \tag{2.3}$$

$$E_z = 0, \tag{2.4}$$

$$H_r = \frac{p\pi A_0}{lk_c}\left[J_n'(k_c r)Y_n'(k_c a) - J_n'(k_c a)Y_n'(k_c r)\right]\cos(n\phi)\cos(\frac{p\pi}{l}z), \tag{2.5}$$

$$H_\phi = \frac{-np\pi A_0}{rlk_c^2}\left[J_n(k_c r)Y_n'(k_c a) - J_n'(k_c a)Y_n(k_c r)\right]\sin(n\phi)\cos(\frac{p\pi}{l}z), \tag{2.6}$$

$$H_z = A_0\left[J_n(k_c r)Y_n'(k_c a) - J_n'(k_c a)Y_n(k_c r)\right]\cos(n\phi)\sin(\frac{p\pi}{l}z), \tag{2.7}$$

where $k_c^2 = \omega^2\mu\epsilon - (p^2\pi^2)/l^2$. A_0 is the amplitude of the field. The amplitude of the field physically signifies the energy storage. In TE_{nsp}, n, s, and p refer to the number of circumferential (ϕ), radial (r), and longitudinal (z) variations, respectively. ω, ϵ, and μ represent operating frequency, permittivity, permeability of medium, respectively. In this analysis, the coaxial cavity is considered to be air filled. $J_n(.)$ and $Y_n(.)$ are the n^{th} order Bessel's functions of the first and second kind, respectively. $J_n'(.)$ and $Y_n'(.)$ are the first derivatives of Bessel's functions of the first and second kind with respect to their arguments, respectively. k_c can be determined by the s^{th} root of the characteristic equations of TE mode and TM mode, which are given as [59]:

$$J_n'(k_c a)Y_n'(k_c b) = J_n'(k_c b)Y_n'(k_c a), \text{ for TE mode,} \tag{2.8}$$

$$J_n(k_c a)Y_n(k_c b) = J_n(k_c b)Y_n(k_c a), \text{ for TM mode,} \tag{2.9}$$

respectively.

Fields corresponding to the TE_{011} mode can be obtained from (2.2 to 2.7) by putting values of n,

s, and p as 0, 1, and 1, respectively:

$$E_r = 0, \quad E_z = 0, \quad H_\phi = 0, \tag{2.10a}$$

$$E_\phi = \frac{j\omega\mu A_0}{k_c}\left[J_0'(k_c r)Y_0'(k_c a) - J_0'(k_c a)Y_0'(k_c r)\right]\sin(\frac{\pi}{l}z), \tag{2.10b}$$

$$H_r = \frac{\pi A_0}{l k_c}\left[J_0'(k_c r)Y_0'(k_c a) - J_0'(k_c a)Y_0'(k_c r)\right]\cos(\frac{\pi}{l}z), \tag{2.10c}$$

$$H_z = A_0\left[J_0(k_c r)Y_0'(k_c a) - J_0'(k_c a)Y_0(k_c r)\right]\sin(\frac{\pi}{l}z), \tag{2.10d}$$

where $k_c^2 = \omega^2\mu\epsilon - \pi^2/l^2$ and k_c can be determined by the 1^{st} root of the characteristic equation for TE_{011} mode. The characteristic equation for TE_{011} mode is obtained from (2.8), that is

$$J_0'(k_c a)Y_0'(k_c b) - J_0'(k_c b)Y_0'(k_c a) = 0. \tag{2.11}$$

2.3 Synthesis of Coaxial Cavity (*design 1*): Method 1

As TE_{011} mode provides high energy storage [14], a coaxial cavity should be designed to operate in this mode. In TE_{011} mode, the electric field is circulating which has its maximum in the middle of the coaxial cavity and the field vanishes at the inner and outer walls of the cavity. Anode cavity structure is housed inside the proposed coaxial cavity. Direction of the electric field in the coaxial cavity is same as that of the operating π-mode of the alternate resonators of the anode cavity. Unwanted modes of the coaxial cavity can be suppressed easily by putting attenuators at appropriate locations [14]. Use of TE_{011} mode also makes mechanical tuning reliable.

Length (l) of the coaxial cavity is determined by the integer multiple of half the guide wavelength *i.e.*

$$l = m\frac{\lambda_g}{2}, \tag{2.12}$$

where $m = 1, 2, 3...$ and λ_g is guide wavelength at operating frequency of coaxial magnetron. The operating frequency is greater than the cut-off frequency of the coaxial transmission line [59]. In the proposed coaxial cavity design, m is chosen as 1 to support desired TE_{011} mode. The cut-off frequency and operating frequency are chosen as 8.6 GHz and 9.32 GHz, respectively. The value of

l is determined from 2.12 as 41.76 mm. For TE mode, azimuthal component of electric field can be obtained from the wave equation. Wave equation can be expressed in cylindrical coordinates [59] as

$$E_\phi = \frac{j\omega\mu}{k_c}(A\sin(n\phi) + B\cos(n\phi))(CJ_n^{'}(k_c\rho) + DY_n^{'}(k_c\rho))\exp(-j\frac{2\pi}{\lambda_g}z), \tag{2.13}$$

where $A,\ B,\ C,\ D$ are arbitrary constants. In the case of coaxial transmission line, $a \leq \rho \leq b$. After applying boundary condition ($E_\phi(\rho, \phi, z) = 0$ for $\rho = a, b$) in (2.13), following relations are obtained as

$$CJ_n^{'}(k_c a) + DY_n^{'}(k_c a) = 0, \tag{2.14}$$

$$CJ_n^{'}(k_c b) + DY_n^{'}(k_c b) = 0. \tag{2.15}$$

Here, n is an integer and represents mode number. $J_n(.)$ and $Y_n(.)$ are n^{th}-order Bessel's functions of the first and second kind, respectively. $J_n^{'}(.)$ and $Y_n^{'}(.)$ are first derivatives of Bessel's function. Order of Bessel function is chosen as 0 for the desired TE_{011} mode. k_c and λ_g represent propagation constant and guide wavelength, respectively. Non-trivial solution of (2.14) and (2.15) exists, only if

$$J_n^{'}(k_c a)Y_n^{'}(k_c b) = J_n^{'}(k_c b)Y_n^{'}(k_c a). \tag{2.16}$$

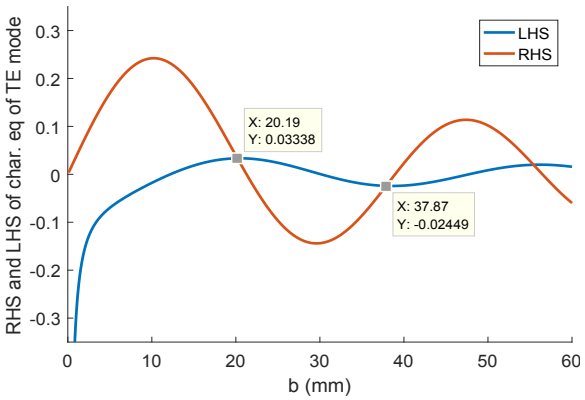

Figure 2.2: Graphical solution of outer radius (b) (mm) from (2.16).

Equation (2.16) is called the transcendental characteristic equation for the TE mode of coaxial transmission line, same as (2.8). Typically, numerical techniques are used to solve such transcendental equations. These methods are quite complex and cumbersome. In this particular case, outer radius (b) is the only unknown geometrical parameter, because inner radius (a) of the cavity is considered as a known parameter, and length l is already determined from (2.12). Inner radius (a) of the coaxial cavity is actually the outer radius of the anode shell of the coaxial magnetron, and it is assumed as 20.19 mm in this analysis. This assumption is based on the dimensions of the anode shell, which are determined in the next chapter of this thesis. Graphical approach is more convenient for this type of solution as compared to numerical techniques. Solution can be determined by the intersection points of LHS and RHS plots of (2.16), as shown in Fig. (2.2). The first intersection point is the trivial solution when both inner and outer radii of the coaxial cavity are same. Thus, this solution is discarded. The desired solution for outer radius (b) is determined as 37.87 mm from the second intersection point the plots, as depicted in Fig. 2.2. Thus, all three design parameters of the coaxial cavity have been determined.

In this method, we have to specify a cut-off frequency (f_c) (8.6 GHz in this case) while determining the dimensions of the coaxial cavity (*design 1*). Different sets of coaxial cavity dimensions can be obtained based on the values of f_c. Moreover, this method doesn't ensure the maximum quality factor of the coaxial cavity. High Q-factor coaxial cavity is required for the coaxial magnetron application. Thus, *design 2* based on method 2 is presented with the maximum Q-factor in the next section.

2.4 Synthesis of Coaxial Cavity (*design 2*) Based on Quality Factor Maximization: Method 2

The determination of Q-factor, and based on the Q-factor maximization, synthesis procedure of coaxial cavity is presented. The section is organized into following two subsections.

2.4.1 Determination of Q-factor

The Q-factor is an important parameter of the microwave cavity synthesis. The coaxial cavity is considered to be filled with air in this analysis. The cavity walls are made of copper, and the finite conductivity of the cavity walls leads to losses in the coaxial cavity. The expression of Q-factor in

terms of average stored electric energy (W_e) and average power loss in conducting walls of the coaxial cavity (P_c) is given as [59]:

$$Q = \frac{2\omega_0 W_e}{P_c}, \tag{2.17}$$

where ω_0 is the resonant frequency of the TE_{011} mode. Average stored electric energy in cavity volume (V) and average power loss over the surface area of lossy walls (S) can be represented as:

$$W_e = \frac{\epsilon_0}{4} \iiint_V |E|^2 \, dV, \tag{2.18}$$

$$P_c = \frac{R_s}{2} \oint_S |H_{tan}|^2 \, dS, \tag{2.19}$$

where H_{tan} is the tangential component of the magnetic field. R_s is the surface resistivity and expressed as $R_s = \sqrt{(\omega_0\mu_0)/(2\sigma)}$, where σ represents the conductivity of the walls of the coaxial cavity.

In this analysis, since the cavity walls are considered to be made of copper, therefore, σ is chosen as 5.8×10^7 Sm^{-1}. Using (2.10), (2.18) and (2.19), W_e and P_c can be obtained as presented in Appendix B:

$$W_e = \frac{\omega_0^2\epsilon_0\mu_0^2\pi A_0^2}{4k_c^2} l \left[\frac{-2}{\pi^2 k_c^2} + \frac{(at)^2}{2} G(z)^2\right], \tag{2.20a}$$

$$P_c = \frac{R_s}{2}\frac{\pi A_0^2}{k_c^2}\left[\frac{4\pi^2}{l^2}\left[\frac{-2}{\pi^2 k_c^2} + \frac{(at)^2}{2} G(z)^2\right] + \frac{4l}{\pi^2 a} + l(at)k_c^2 G(z)^2\right], \tag{2.20b}$$

where $G(z) = Y_1(z)J_0(tz) - J_1(z)Y_0(tz)$, and t is the ratio of outer and inner radii of the coaxial cavity ($t = b/a$) and $z = k_c a$. Using (2.17), (2.20a), and (2.20b) expression of Q-factor can be determined as:

$$Q = \frac{\frac{\omega_0^3\epsilon_0\mu_0^2}{2} l \left[\frac{-2}{\pi^2 k_c^2} + \frac{(at)^2}{2} G(z)^2\right]}{\frac{R_s}{2}\left[\frac{4\pi^2}{l^2}\left[\frac{-2}{\pi^2 k_c^2} + \frac{(at)^2}{2} G(z)^2\right] + \frac{4l}{\pi^2 a} + l(at)k_c^2 G(z)^2\right]}. \tag{2.21}$$

2.4.2 Synthesis Procedure of Coaxial Cavity

For synthesis of a coaxial cavity, three design parameters are required, which are inner radius (a), outer radius (b), and length (l). As discussed in method 1, the inner radius (a) of the coaxial

cavity is considered as a known parameter, and it depends on the outer radius of the anode shell of coaxial magnetron. Remaining two unknown design parameters, b and l are required to be determined. Length of the cavity (l) is determined from the first root of the characteristic equation for TE_{011} mode. Characteristic equation of the TE_{011} mode is expressed in terms of t and z as:

$$J_0'(z)Y_0'(tz) - J_0'(tz)Y_0'(z) = 0. \tag{2.22}$$

The first root ($z_{01}^{'}$) of (2.22) is expressed in a closed form, as [62]:

$$z_{01}' = \sqrt{\left(\frac{\pi^2}{(t-1)^2} + \frac{3}{(t+1)^2}\right)}. \tag{2.23}$$

Length of the coaxial cavity (l) can be determined by the expression of k_c used in (2.11), that is

$$l = \frac{\pi}{\sqrt{\omega^2\mu_0\epsilon_0 - k_c^2}}. \tag{2.24}$$

where k_c is a known parameter and can also be expressed in terms of the first root of the characteristic equation (2.22), $k_c = z_{01}'/a$. Cavity length expressed by (2.24) is a real quantity only if,

$$\begin{aligned} k_c^2 &< \omega^2\mu_0\epsilon_0, \quad \Rightarrow k_c < \frac{\omega}{\frac{1}{\sqrt{\mu_0\epsilon_0}}} \\ \Rightarrow a &> \frac{\lambda}{2\pi}\sqrt{\left(\frac{\pi^2}{(t-1)^2} + \frac{3}{(t+1)^2}\right)}, \text{ as } k_c = \frac{z_{01}'}{a}. \end{aligned} \tag{2.25}$$

For specified inner radius (a = 20.19 mm) and operating frequency of the coaxial magnetron (f_0 = 9.32 GHz), condition on t for which coaxial cavity length (l) is a real quantity, can be obtained as: $t > 1.81$.

The variation of Q-factor and cavity length (l) with respect to radii ratio (t) is plotted in Fig. 2.3. Here, t is chosen according to the condition ($t > 1.81$). The outer radius (b) and length (l) of the coaxial cavity (unknown parameters) are determined by maximizing Q-factor. The maximum Q-factor for TE_{011} mode is obtained at t = 2.13 and corresponding l is obtained as 23.13 mm as depicted in Fig. 2.3. The outer radius of the cavity is determined as 43 mm for the known inner radius (a = 20.19 mm). The coaxial cavity with these design parameters is denoted as *design 2* in this chapter.

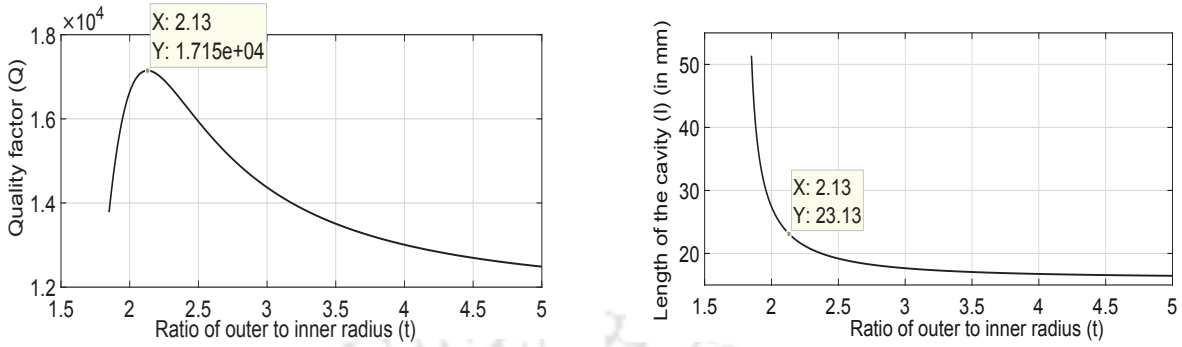

(a) (b)

Figure 2.3: Determination of the length and radius ratio of the coaxial cavity for the maximum quality factor. (a) Variation of Q-factor with respect to t. (b) Variation of length (l) with respect to t.

Table 2.1: Comparison of Q-Factors of Coaxial Cavities for TE_{011} Mode

Coaxial cavities	Operating freq.(f_0)	$Q_{analytical}$	Q_{CST}	Q_{HFSS}
Design 1 (Method 1)	9.32 GHz	14635	14482	14302
Design 2 (Method 2)	9.32 GHz	17150	17123	17093

Design parameters of the coaxial cavity for *design 1* are obtained using the method 1, as discussed in the previous section. In method 1, the dimensions of *design 1* are obtained by solving the transcendental characteristic equation of TE mode (2.8). However, *design 1* does not ensure the maximum Q-factor. A comparison between the Q-factors of *design 1* and *design 2* is presented in Table 2.1. Q-factor determined by using (2.21) is referred as $Q_{analytical}$. Quality factors obtained from analytical approach are compared with the Q-factors obtained from the simulation in CST and HFSS, for this comparison, dimensions of coaxial cavity obtained from method 1 and method 2 are considered. Q-factors determined by CST and HFSS are represented by Q_{CST} and Q_{HFSS}, respectively. While performing simulations in HFSS and CST, wall thickness of 2 mm is considered. The operating frequency of TE_{011} mode are kept as same (9.32 GHz) for both the coaxial cavities. It can be concluded from Table 2.1 that *design 2* has higher Q-factor as compared to *design 1*, and also analytical and simulation results are in good agreement. The minor variation occurs due to the higher losses in simulations as skin depth effect is also considered in surrounding walls of the coaxial cavity.

Table 2.2: Comparison of the Resonant Frequencies of Different Modes in the Proposed Coaxial Cavity

Modes	f_r(analytical)	f_r(simulation)
TE_{011}	9.32 GHz	9.32 GHz
TE_{121}	9.49 GHz	9.48 GHz
TE_{221}	9.96 GHz	9.95 GHz
TE_{321}	10.71 GHz	10.71 GHz
TM_{011}	9.2 GHz	9.19 GHz
TM_{111}	9.32 GHz	9.32 GHz
TM_{211}	9.71 GHz	9.7 GHz
TM_{311}	10.30 GHz	10.29 GHz

2.5 Determination of Resonant Modes and Mode Diagram

Identification of resonant frequencies of the adjacent modes (neighboring modes) and their sequence of occurrence is crucial for the design of a microwave cavity. In this study, potential competing modes are determined for the desired mode excitation. The resonant frequency ($f_{r,nsp}$) of TE_{nsp} and TM_{nsp} modes is determined as [63]:

$$f_{r,nsp} = \begin{cases} \frac{c}{2}\sqrt{\left(\frac{z'_{ns}}{\pi a}\right)^2 + \left(\frac{p}{l}\right)^2}, & \text{for TE mode,} \\ \frac{c}{2}\sqrt{\left(\frac{z_{ns}}{\pi a}\right)^2 + \left(\frac{p}{l}\right)^2}, & \text{for TM mode,} \end{cases} \tag{2.26}$$

where z'_{ns} and z_{ns} are the s^{th} roots of the characteristic equations (2.8) and (2.9), respectively. c is the speed of light in free space. Resonant frequencies of the adjacent modes are determined from (2.26) (f_r (analytical)) and listed in Table 2.2.

Resonant frequencies determined from analytical approach are compared with the resonant frequencies obtained from the eigenmode solver of the proposed coaxial cavity in CST. The frequencies obtained from simulation and analytical method are in good agreement, as presented in Table 2.2. The mode diagram based on the data presented in Table 2.2 for the proposed coaxial cavity is plotted

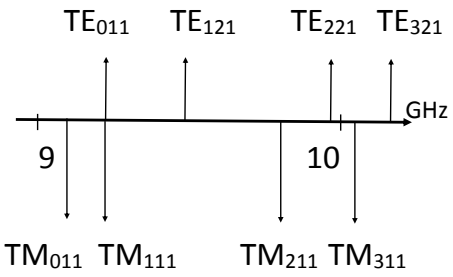

Figure 2.4: Mode diagram of the proposed coaxial cavity.

in Fig. 2.4. Mode diagram illustrates the sequence of the resonant modes occurring in the neighborhood of the desired TE_{011} mode. Some of the resonant modes are in the vicinity of TE_{011} mode. Thus, the possibility of excitation of unwanted modes is quite high even for a small perturbation in the operating conditions of the coaxial magnetron. Since the outer coaxial cavity is coupled to the anode shell, and the excitation of unwanted modes in the outer cavity can also influence the mode excitation in vane cavities of the anode shell. Number of electron spokes in a coaxial magnetron are formed in accordance with the operating mode of vane cavities, which decides the effectiveness of wave-particle energy transfer. Thus, the excitation of unwanted modes in the outer coaxial cavity can disturb the coaxial magnetron operation and therefore, degrades the performance of the device. Hence, the suppression of unwanted modes is needed for the proper operation of coaxial magnetron.

2.6 Suppression Technique for the Unwanted TE_{121} Mode

The desired mode of operation in the coaxial cavity is TE_{011} mode. TM_{011}, TM_{111}, TE_{121}, TM_{211}, TE_{221}, and TM_{311} modes are the competing modes for the desired TE_{011} mode, as illustrated by mode diagram in Fig. 2.4. Output of the coaxial magnetron is taken from the rectangular waveguide through longitudinal slot coupling in the outer coaxial cavity wall. Here, the rectangular waveguide operates in the dominant TE_{10} mode. The field pattern of the TM modes in the coaxial cavity does not match the field pattern of TE_{10} mode of rectangular waveguide [63]. Thus, all competing TM modes of coaxial cavity automatically get suppressed by such output mechanism of the coaxial magnetron. The resonant frequency of TM_{111} mode is same as the TE_{011} mode, but TM_{111} mode automatically gets suppressed by the output mechanism. Among remaining competing modes, which are TE modes,

the TE_{121} mode is the most likely infringing mode to the TE_{011} mode. TE_{121} mode required to be suppressed for proper operation of the coaxial magnetron.

The electric field patterns of both TE_{011} mode and TE_{121} mode are shown in Fig. 2.5. Here, the mode designation follows the convention, given in [64]. According to the convention, the electric field of TE_{011} mode has no phase shift along circumferential direction, and π phase shift along radial and axial directions. But electric field of TE_{121} mode has π phase shift along axial direction, and 2π phase shift along radial and circumferential directions. Based on the surface current distribution profiles of TE_{011} mode and TE_{121} mode, the position of the unwanted mode suppressor is chosen. Surface current distribution of the unwanted TE_{121} mode along with the desired TE_{011} mode of the proposed coaxial cavity is shown in Fig. 2.6. TE_{011} mode has circulating surface current distribution because only E_ϕ component is non-zero. The coaxial magnetron is also known as circular electric mode (CEM) magnetron because of the circulating electric field pattern of TE_{011} mode [61]. TE_{011} mode has negligible surface current at the junctions between each end plate and the cylindrical surface, as shown in Fig. 2.6. This makes the TE_{011} mode unique among competing modes. However, significant surface current exists at the inner and outer junctions for the TE_{121} mode. This difference is utilized in order to reduce the Q-factors of the unwanted modes in this chapter. Competent modes having lower

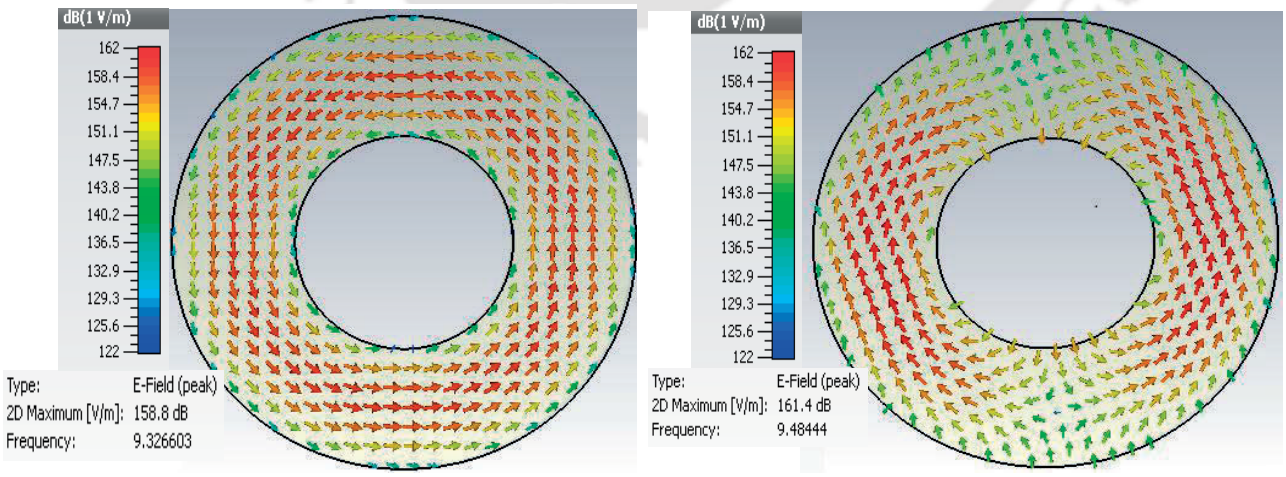

(a) (b)

Figure 2.5: Electric field patterns of a coaxial cavity (top view). (a) TE_{011} mode at 9.32 GHz. (b) TE_{121} mode at 9.48 GHz.

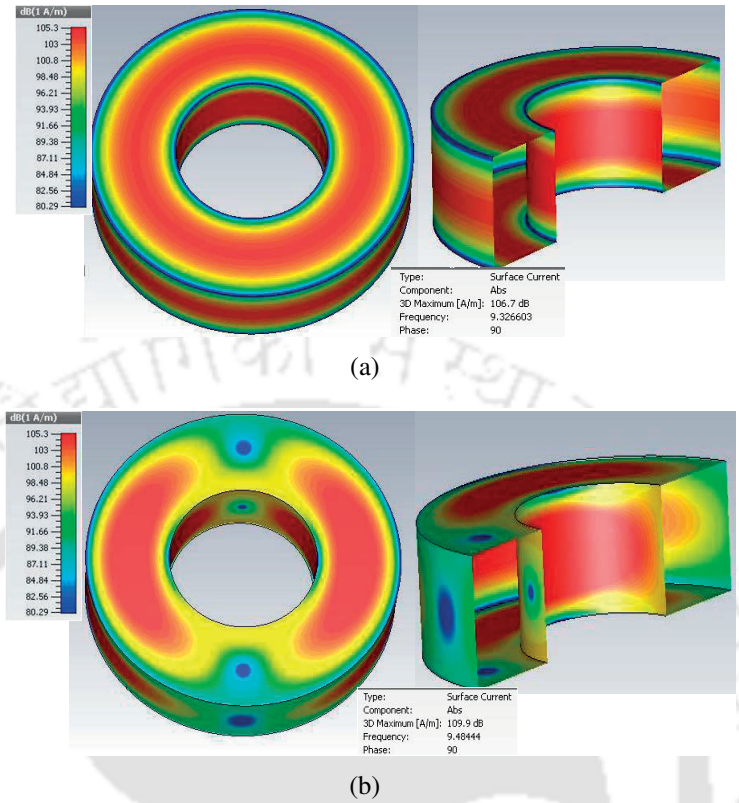

Figure 2.6: Surface current distribution of the coaxial cavity obtained from the eigenmode solver of CST simulator. (a) TE_{011} mode at 9.32 GHz. (b) TE_{121} mode at 9.48 GHz.

Q-factor, have less likely to get excited. Thus, significant suppression in the Q-factor of the TE_{121} mode will improve the excitation in the desired TE_{011} mode.

The unwanted modes are damped out by introducing auxiliary cavities with lossy dielectric materials in the coaxial cavity, as shown in Fig. 2.7. The suppressor need to be placed in such a manner that it does not affect the desired TE_{011} mode. In order to suppress the undesired modes, one suppressor (lossy dielectric) is placed near the inner wall of the cavity and another near the outer wall of the cavity. The step impedance transformers are employed to couple the outer coaxial cavity and the auxiliary cavities. The dimensions of impedance transformers are further optimized to couple the surface current of unwanted TE_{121} mode to the lossy materials of auxiliary cavities. The coupling of TE_{121} mode suppress it and reduces the Q-factor. Similarly, the Q-factors of other undesired modes also get reduced, which have the nonzero surface current at the inner or outer junctions of coaxial cavity walls. However, Q-factor of the desired TE_{011} mode remains unaffected due to the unique

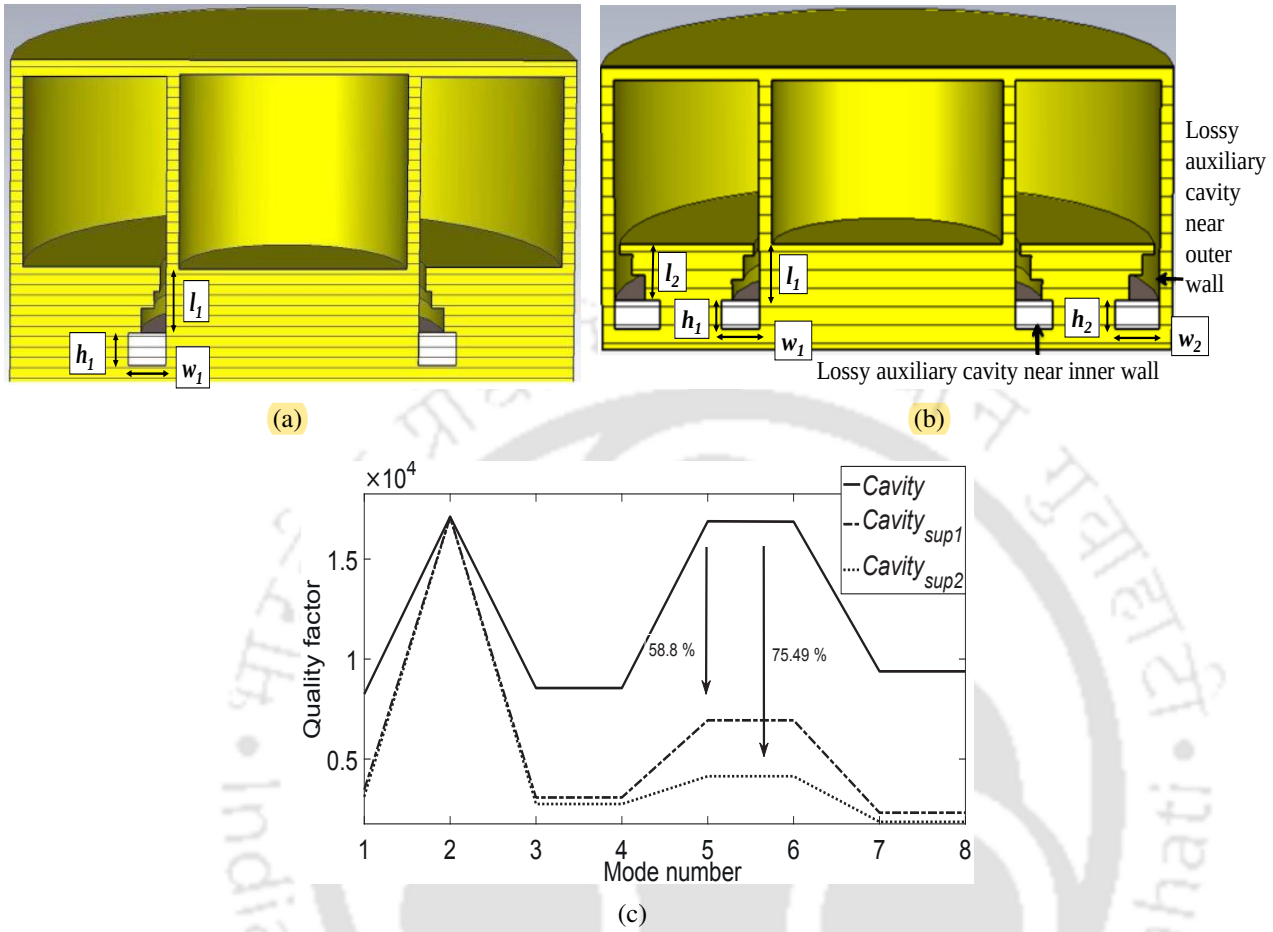

Figure 2.7: Unwanted mode suppression mechanism in coaxial cavity. (a) Cross-sectional view of the coaxial cavity with lossy auxiliary cavity near inner wall [l_1 = 7.5 mm, w_1 = 5 mm, h_1 = 4.8 mm]. (b) Cross-sectional view of the coaxial cavity with lossy auxiliary cavities both at near inner and outer walls of the cavity [l_1 = 7.5 mm, w_1 = 5 mm, h_1 = 4.8 mm, l_2 = 7.5 mm, w_2 = 6 mm, h_2 = 4.8 mm]. (c) Suppression of the Q-factors of unwanted modes after applying suppression technique.

property of current distribution; it has zero surface current distribution at the junctions. Effects of mode suppressors mechanism on the Q-factors of various modes are shown in Fig. 2.7(c). Q-factors are plotted with respect to the mode numbers in Fig. 2.7(c). Here, Q-factors of the various modes of coaxial cavity without any mode suppressor are denoted as *Cavity*. Similarly, Q-factors of the coaxial cavity with lossy auxiliary cavity near inner wall is denoted as $Cavity_{sup1}$, and coaxial cavity considering lossy auxiliary cavities near both inner and outer walls are denoted as $Cavity_{sup2}$. TM_{011} and TE_{011} modes are represented by mode no. 1 and 2, respectively. Mode no. 3, 4 represent TM_{111} mode, 5, 6 represent TE_{121} mode, and 7, 8 represent TM_{211} mode of the coaxial cavity. Mode patterns

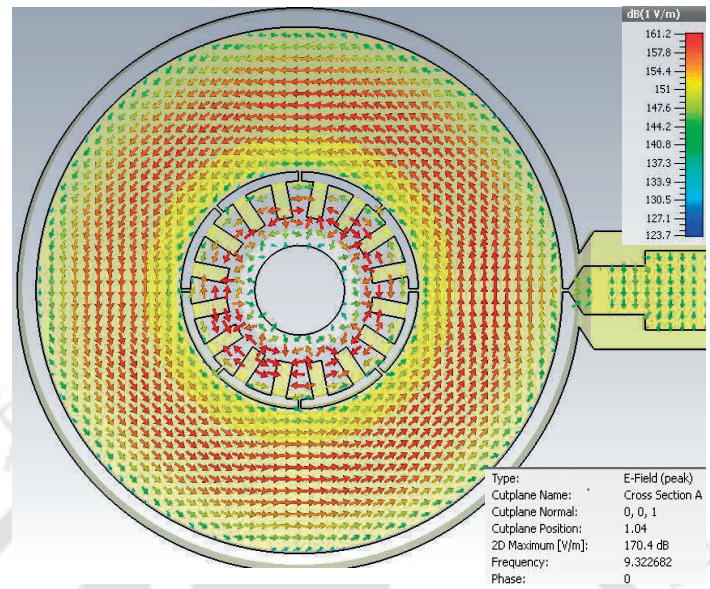

(a)

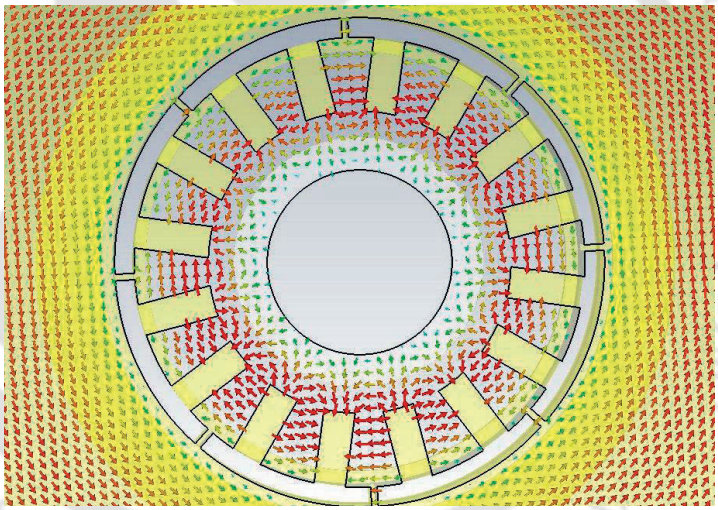

(b)

Figure 2.8: Electric field pattern of π-mode in anode shell and TE_{011} mode pattern in the external cavity. (a) Cross-sectional view of the coaxial magnetron. (b) π-mode pattern in the zoomed view of anode shell.

of TM_{011} mode (mode no. 1) and TE_{011} mode (mode no. 2) are symmetrical in azimuth, and have single occurrence. However, because of the different polarization, remaining illustrated modes occur in pairs, as depicted in Fig. 2.7(c). CST considers both x and y polarization while displaying the field pattern and current distribution pattern of a mode. From Fig. 2.7(c), Q-factor of the undesired TE_{121} mode is reduced by 58.8% by use of inner auxiliary cavity near inner wall ($Cavity_{sup1}$) and it further

reduced to 75.49% when both auxiliary cavities are considered ($Cavity_{sup2}$). Q-factor of the desired TE_{011} mode is not affected by the proposed mode suppression technique for unwanted modes. A significant reduction in the Q-factors of other competing modes of the coaxial cavity is also observed.

The coaxial cavity proposed in this chapter has application in designing coaxial magnetrons. A cross-section of typical 16-vane coaxial magnetron is shown in Fig. 2.8. The coaxial cavity is placed outside of the anode shell subsystem in the coaxial magnetron, as shown in Fig. 2.8. Anode shell consists of multitude of vanes (in this case 16). The RF generated in the anode shell is further coupled to the external coaxial cavity through coupling slots present in alternate vane resonators, as shown in Fig. 2.8. Coaxial magnetron is operated in the π-mode for efficient operation. Eigenmode analysis is carried out to verify the simultaneous mode occurrence of TE_{011} mode in the outer coaxial cavity and π-mode in the anode shell of the coaxial magnetron at the desired operating frequency. The desired π-mode in the anode shell has 180° phase difference in the electric field pattern of adjacent vanes cavities, which is illustrated in Fig. 2.8 (b). π-mode and TE_{011} mode occur simultaneously at the operating frequency of 9.32 GHz. The output is taken from the standard rectangular waveguide (WR112) from the outer coaxial cavity through slot coupling. The rectangular waveguide is operating in the dominant TE_{10} mode, as depicted in Fig. 2.8(a).

2.7 Summary

This chapter presents the design methods of coaxial cavity, an essential part of coaxial magnetron. Two methods are presented for coaxial cavity design. Synthesis of the coaxial cavity based on the Q-factor maximization (method 2), which is a better approach than method 1, where dimensions are determined by solving the transcendental characteristic equation of TE mode. Method 1 doesn't ensure the maximum Q-factor. The Q-factor of a coaxial cavity for TE_{011} operating mode is determined analytically and verified by CST and HFSS simulations. The walls of coaxial cavity are considered to be made of copper and cavity is filled with air. The optimum value of quality factor is obtained analytically as 17150 for TE_{011} mode operating at 9.32 GHz. Various competing modes or infringing modes of the desired TE_{011} mode are determined using analytical and simulation methods. The excitation of TE_{011} mode, which has circulating electric field, is required for the proper operation

of coaxial magnetron. TE_{121} mode is the most likely infringing mode to TE_{011} mode, and a suppression technique for the unwanted mode is presented by employing auxiliary cavity filled with the lossy dielectric material. Unwanted modes are suppressed by utilizing the surface current distribution property of the desired TE_{011} mode. By this unwanted mode suppression technique, quality factor of TE_{121} mode is reduced by 75.49% while keeping quality factor of the desired TE_{011} mode unaffected. The significant reduction in quality factors of other unwanted modes is also observed. The coaxial cavity with optimum quality factor is utilized later in this thesis for design of coaxial magnetron. The performance of coaxial cavity is also verified using the PIC simulation of overall coaxial magnetron presented in later chapters.

3

Synthesis of Anode Resonator and Output Section

Contents

The previous chapter provided the design procedure of the outer coaxial cavity for the coaxial magnetron. This chapter presents the systematic design procedure of a 28-vane anode resonator. The design of other sub-parts of the coaxial magnetron is also discussed. Eigenmode analysis, dispersion diagram, and cold test analysis of the coaxial magnetron are presented in this chapter. The effects of surface roughness of metal are also analyzed considering frequency-dependent effective conductivity.

3.1 Introduction

Anode resonator is a critical part of a coaxial magnetron, where similar to a conventional magnetron, RF oscillations get generated. An anode resonator consists of multitude of vane-type cavities placed coaxially surrounded to the cathode. However, strapping of the vanes is not required in a coaxial magnetron, as the outer coaxial cavity operating in the circulating TE_{011} mode provides stability to the π-mode of the anode resonator. Alternate vane cavities are coupled to the outer coaxial cavity through longitudinal slots. Apart from the anode resonator and an outer coaxial cavity, a coaxial magnetron also houses unwanted mode suppressors, output section, and frequency tuner.

This chapter is organized into six sections including introduction. Section 3.2 is about the coaxial magnetron design in which the synthesis of anode resonator is presented in detail. A systematic design procedure is provided for determining the initial dimensions of the anode resonator from the empirical design equations. Section 3.3 deals with the cold test analysis of coaxial magnetron. Eigenmode simulation is carried out to determine the operating modes, mode separations between competing modes, and the dispersion diagram. Frequency-domain simulation is performed to analyze coupling and to determine the cold test parameters such as Q-factors, coupling coefficient, and circuit efficiency. A rectangular waveguide to cylindrical cavity mode launcher is proposed in Section 3.4 to analyze the coupling between anode resonator and outer coaxial cavity, and also to optimize the dimensions of longitudinal coupling slots. The design and performance analysis of the proposed mode launcher is discussed in Appendix C in detail. The effects of surface roughness of copper on the cold test parameters are presented in Section 3.5. Section 3.6 concludes this chapter.

3.2 Design of the Coaxial Magnetron

A coaxial magnetron chiefly consists of many subparts. These subparts include an external coaxial cavity, anode resonator, cathode, mode suppressors for undesired modes such as slot modes and TE_{121} mode, output section, and frequency tuner. In this section, the systematic design procedure of a coaxial magnetron is presented. Initial dimensions of anode resonator are determined from the empirical relations. In this chapter, the coaxial magnetron's walls are considered to be made of copper with finite bulk conductivity of 5.8×10^7 Sm^{-1}.

3.2.1 Anode Resonator Design

The anode shell houses multiple vane-type resonators, as shown in Fig. 3.1. Dimensions l_v, t_v, h, and r_a represent length, thickness, height of the vanes, and anode radius, respectively. The initial dimensions of anode resonator can be determined by using (3.1 - 3.9) [27, 65].

$$B = b\frac{42400}{(1-\sigma^2)\lambda N} \tag{3.1}$$

$$r_a = \frac{\lambda N}{6320}\sqrt{V_a/v} \tag{3.2}$$

$$h = 2.39\lambda\left(\frac{v}{V_a}\right)\left(\frac{I_a}{i}\right)\left(\frac{N}{A}\right) \tag{3.3}$$

$$r_c = \sigma\frac{\lambda N}{6320}\sqrt{V_a/v} \tag{3.4}$$

$$\sigma = \frac{r_c}{r_a} \approx \frac{N-4}{N+4} \approx 0.85 - \frac{3.83}{N} \tag{3.5}$$

$$\eta_t = \eta_e\eta_c \tag{3.6}$$

$$B/B_0 = \frac{\eta_e - 2}{2\eta_e - 2} \tag{3.7}$$

$$t_v = [(0.64 \times 2\pi r_a)/N)] \tag{3.8}$$

$$l_v = 0.11\lambda \tag{3.9}$$

here B, r_a, r_c, σ, h, V_a, I_a, t_v, l_v are magnetic field density (Gauss), anode radius (cm), cathode radius (cm), the ratio of cathode and anode radii, anode height (cm), anode voltage (Volt), anode current (Amp), vane thickness (cm), and vane length (cm), respectively. λ is the wavelength (cm)

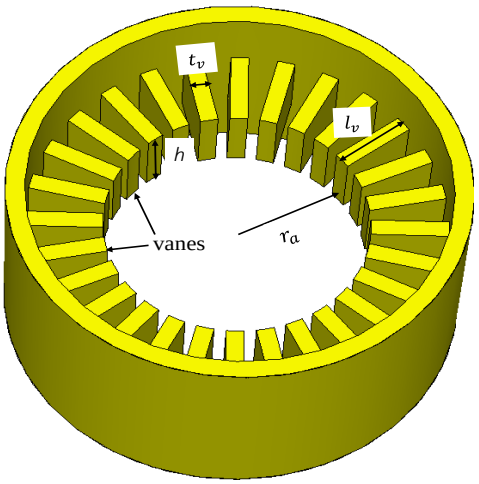

Figure 3.1: Anode resonator of the coaxial magnetron with 28 vanes

corresponding to the operating frequency (f_0). v, b, i are dimensionless parameters and called as reduced variables. A is a variable and a function of σ. These parameters are determined by the empirical relations [27, 65].

Desired specifications of the coaxial magnetron primarily include operating frequency (f_0), peak power (P_{peak}), average power (P_{avg}), anode voltage (V_a), and total efficiency (η_T). The values of f_0, P_{peak}, P_{avg}, V_a, and η_T are considered in this chapter as 9.32 GHz, 2 MW, 2 kW, 45 kV, and 70%, respectively. Megawatt-class coaxial magnetrons operating in 9.3 GHz have application in medical linear accelerators, as discussed in chapter 1. All reported coaxial magnetrons operating in X-band have output peak powers less than 2 MW, as shown in Table 1.4. Therefore, operating frequency and output peak power are considered as 9.32 GHz, and 2 MW, respectively. f_0 is considered as slightly higher than the desired frequency (9.3 GHz) because the introduction of coupling slots reduces the resonant frequency.

Step-by-step procedure for the determination of initial dimensions of the anode resonator is as follows:

☞ **Step 1:** To initiate the design, it is essential that values of certain parameters are chosen appropriately. Anode current (I_a), circuit efficiency (η_C), and number of vanes (N) are chosen as 80 Amp, 80%, and 28, respectively. These parameters are chosen based on the available literature [11, 41] and experience gained from initial simulations.

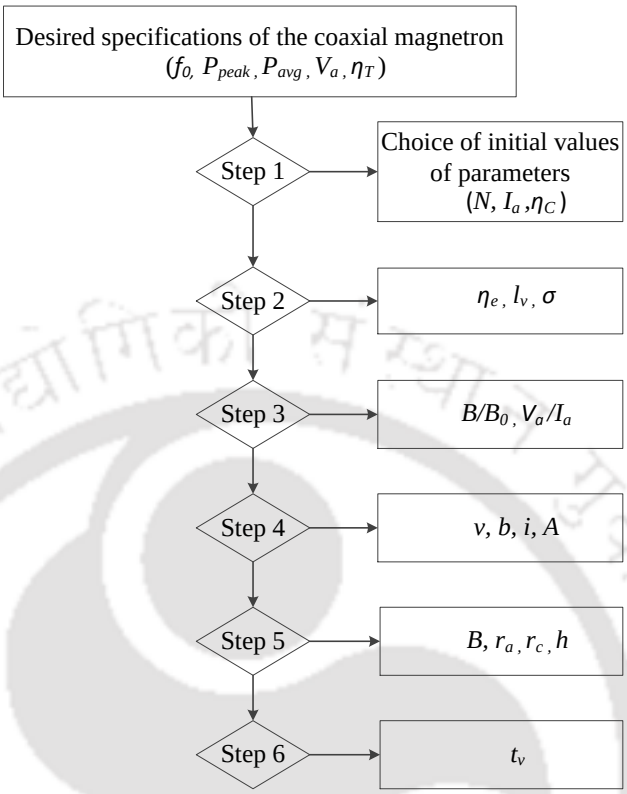

Figure 3.2: Stepwise procedure for determining initial dimensions of anode resonator.

- **Step 2:** Electronic efficiency (η_e), vane length (l_v), and ratio of cathode and anode radii (σ) are determined from (3.6), (3.9), and (3.5), respectively.

- **Step 3:** In this step, B/B_0 is determined by using the η_e value (from step 2) in (3.7). The value of impedance (V_a/I_a) is also obtained (V_a is specified and I_a from step 1).

- **Step 4:** In this step, reduced variables such as v, b, i, and A are determined from the empirical relations given in [27, 65]. The value of parameter A is obtained by using the value of N. Impedance calculated in step 3 is used to obtain i, and using the value of B/B_0 (from step 3), parameters v and b are determined.

- **Step 5:** B, r_a, r_c, and h are obtained by (3.1, 3.2, 3.4), and (3.3), respectively using values of the parameters obtained in previous steps.

- **Step 6:** In this final step, t_v is calculated from (3.8) using the values of r_a and N obtained from

Table 3.1: Design Parameters of the Anode Resonator

Parameters	Initial values	Optimized values
Vane thickness (t_v)	1.5 mm	1 mm
Vane height (h)	5.2 mm	8.2 mm
Vane length (l_v)	3.54 mm	5.96 mm
Anode diameter ($2r_a$)	20.76 mm	20.76 mm
Cathode diameter ($2r_c$)	14.8 mm	16.4 mm
σ	0.71	0.78

previous steps.

Based on chosen values of selected parameters and following the design procedure outlined, initial dimensions are determined and presented in Table 3.1. The dimensions are further optimized considering the loading effect of the outer coaxial cavity and based on the results of particle-in-cell simulation of the coaxial magnetron.

3.2.2 Design of Coaxial Cavity and Output Section

The external coaxial cavity of magnetron is designed as per the method 2 discussed in chapter 2. The coaxial cavity is optimized for the maximum Q-factor for the TE_{011} operating mode. In chapter 2, the coaxial cavity is designed considering the 16-vane anode resonator. However, the desired power and efficiency couldn't be achieved from 16-vane coaxial magnetron, and therefore a 28-vane anode resonator is considered here which could deliver the desired output power as discussed in the PIC simulation of the coaxial magnetron in chapter 5. The same design procedure is followed for designing the coaxial cavity for the 28-vane anode resonator. Dimensions of the coaxial cavity are represented by coaxial cavity length (l_{cavity}), outer radius of the cavity (r_o), and inner radius of the cavity (r_i), as shown in Fig. 3.3. The inner radius of coaxial cavity (r_i) is also the outer radius of anode shell. The value of r_i depends on the dimensions of anode shell, and is considered as a known design parameter of the coaxial cavity in method 2, as discussed in chapter 2. r_i is the summation of anode radius (r_a), vane length (l_v), and the material thickness of anode shell. In this thesis, the thickness

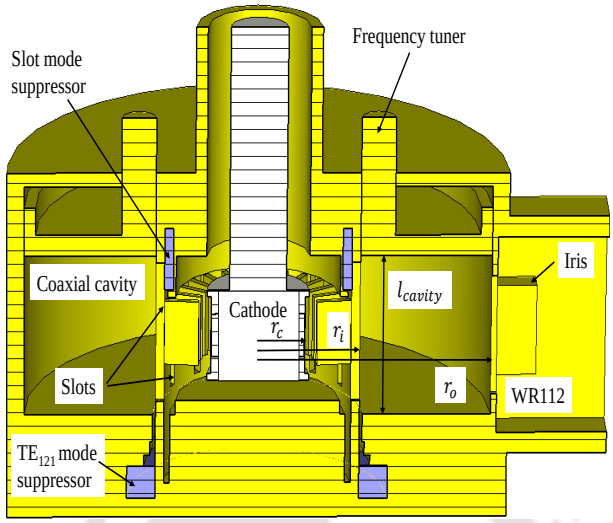

Figure 3.3: A cross-sectional view of the proposed coaxial magnetron with unwanted mode suppressors.

of anode shell is considered as 1.5 mm. The values of coaxial cavity dimensions (r_i, r_o, and l_{cavity}) are determined from method 2 as 17.84 mm, 40.81 mm, and 23.1 mm, respectively. In the coaxial magnetron, alternate vane cavities are coupled to the external coaxial cavity through longitudinal rectangular coupling slots present in the common wall of anode shell and outer coaxial cavity, as shown in Fig. 3.3. The dimensions of coupling slots, namely length, width and thickness are taken as 20.1 mm, 1.4 mm, and 1.5 mm (same as the thickness of anode shell), respectively. The dimensions of coupling slots can be further optimized while performing frequency-domain and PIC analyses of the coaxial magnetron. The introduction of the coupling slots in the anode shell requires re-optimization of the dimensions for obtaining the desired resonant frequency.

The output section of a coaxial magnetron is used to deliver generated RF signal. In this work, a standard rectangular waveguide WR112 section is used as the output port. The output is taken via a rectangular coupling slot, which is placed at the external wall of the coaxial cavity, as shown in Fig. 3.3. For obtaining efficient coupling, this coupling slot is placed where the maximum electric field strength exists. Since the outer coaxial cavity operates in the TE_{011} mode, the maximum electric field strength occurs in the middle of the cavity along the length. Thus, the output is taken from the middle of the cavity along the length through a rectangular slot in outer wall, as shown in Fig. 3.3. For the impedance matching between the coaxial cavity (or coaxial magnetron) and output waveguide,

irises are introduced near the coupling slot, as shown in Fig. 3.3. Generally, in the conventional magnetron, loop coupling is used instead of slot coupling in the output section. The power handling capability of slot coupling is much higher than the loop coupling. The coaxial magnetron also has a wider frequency-tuning range as compared to the conventional magnetron. The operating frequency can be tuned by adjusting length of the coaxial cavity, which is denoted by l_{cavity}, as shown in Fig. 3.3. With the mechanical frequency tuner as shown in Fig. 3.3, the frequency of the magnetron can be adjusted by moving the tuner along the length of the cavity. Frequency-tuning in the coaxial magnetron is relatively easy because tuning process doesn't affect the fields of anode cavities. The operating frequency of the coaxial magnetron is controlled by the high-Q external cavity.

3.2.3 Unwanted Mode Suppressors

The excitation of undesired modes affects the functioning of a coaxial magnetron adversely. TE_{121} mode and slot modes are primary interfering modes out of many competing modes of the desired TE_{011} mode. These unwanted modes affect the operating frequency, output power, and stability of operation. Thus, suppression of such modes are essential for the proper magnetron operation. TE_{121} mode occurs due to the external coaxial cavity, and single or double auxiliary cavities with lossy material are used to suppress it, as discussed in chapter 2. In this analysis, single auxiliary cavity with lossy dielectric is considered near the junction of anode shell and external cavity. Excitation of slot modes occurs due to the longitudinal coupling slots present in the common wall of the anode shell and external coaxial cavity. Identification and analysis of slot mode suppression mechanism is presented in detail in the next chapter, chapter 4. In this chapter, eigenmode and cold test analyses are carried out considering both slot modes and TE_{011} mode suppressors in the coaxial magnetron structure.

3.3 Cold Test Analysis of Coaxial Magnetron

The coaxial magnetron simulation is performed in three steps: eigenmode, frequency-domain, and particle-in-cell (PIC) analyses. In the first step of eigenmode analysis, desired mode operation at the given frequency, neighboring modes or competing modes, and dispersion diagram are determined using eigenmode simulation. Frequency-domain simulation is performed in the second step. In this

step, coupling of the coaxial magnetron is analyzed. Various cold test parameters such as coupling coefficient, Q-factors, and circuit efficiency are determined. In the final step, PIC simulation is performed to determine the output performance. Only eigenmode and frequency-domain analyses are presented in this chapter. PIC analysis is discussed in chapter 5. All these simulations in this chapter are performed in CST studio.

3.3.1 Eigenmode Simulation

The desired operating mode of a coaxial magnetron is the π-mode in the anode resonator and TE_{011} mode in the the external coaxial cavity. The operating mode of a magnetron is identified by analyzing electric field patterns at the resonant frequency. Electric field patterns of various modes of coaxial magnetron are studied and the desired mode pattern is shown in Fig. 3.4. π-mode having 180° phase shift in the electric fields of the adjacent vane cavities is observed and circulating electric field pattern of TE_{011} mode is also observed simultaneously at the desired operating frequency of 9.3 GHz, as shown in Fig. 3.4.

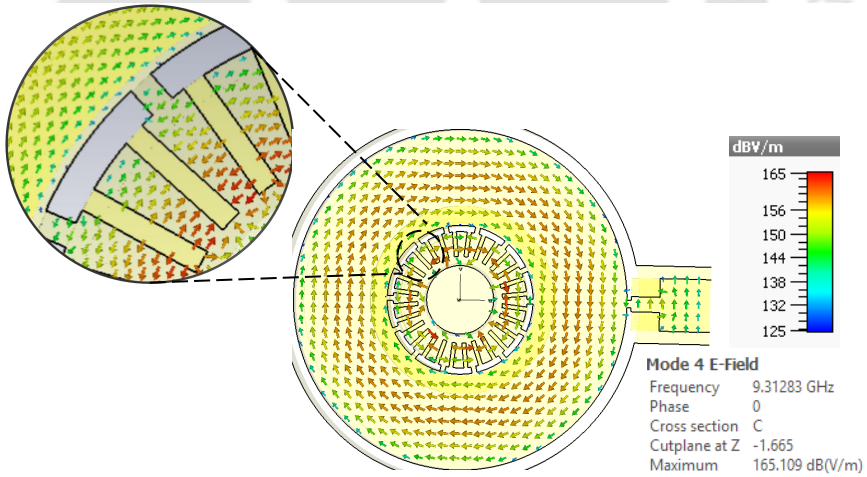

Figure 3.4: E-field vector plot of the coaxial magnetron showing the π-mode in the anode resonator and TE_{011} mode in the external coaxial cavity at the same operating frequency.

Dispersion diagram of the coaxial magnetron is shown in Fig. 3.5. The resonant frequencies of various modes of the magnetron are plotted with respect to the mode numbers in the dispersion diagram. In the diagram, plot A represents the occurrence of resonating modes in anode resonator without considering the external coaxial cavity, similar to conventional magnetron. Corresponding

to 28 number of vane cavities (N=28), 14^{th} mode number represents π-mode in the dispersion diagram. Plot A is similar to the conventional magnetron, and very small mode separation (4 MHz) is observed in the resonant frequencies of neighboring modes of π-mode. This small frequency separation makes the mode competition high in a conventional magnetron, and strapping is used to improve mode separation. However, in a coaxial magnetron, introduction of external coaxial cavity reduces the mode competition significantly without the need of strapping of vanes. Plot B and C represent the dispersion curves of magnetron with external coaxial cavity, as shown in Fig. 3.5. Moreover, introduction of outer coaxial cavity and longitudinal coupling slots in anode shell's wall generate multiple additional resonant modes. Some of these additional modes are represented by plot B and plot C in the dispersion diagram. The coupling slots in the anode shell's wall shift the resonant frequency of the desired π-mode. In this analysis, dimensions of coaxial magnetron are optimized to achieve the π-mode frequency the same as it was before the introduction of the outer coaxial cavity. The resonant frequency of slot mode is also shown in Fig. 3.5. Slot modes occur in the pair: lower slot mode and upper slot mode. The lower slot mode has resonant frequency less than the π-mode frequency, and higher slot mode has higher resonant frequency than π-mode frequency. The identification and suppression of slot mode is discussed in detail in the next chapter. Lower slot mode is shown in plot C in Fig. 3.5.

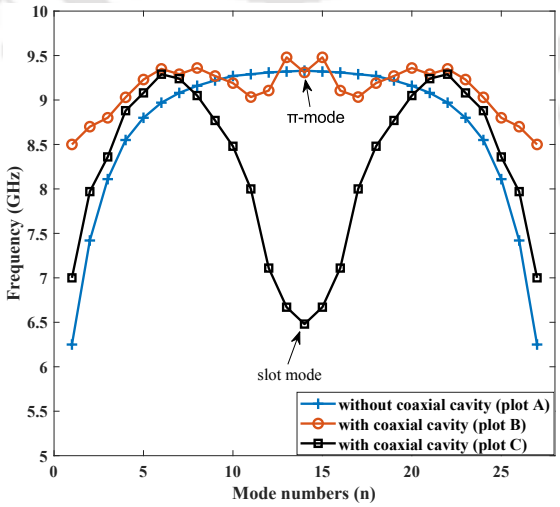

Figure 3.5: Dispersion diagram of the proposed coaxial magnetron. Plot A represents resonant modes of anode resonator without considering the external coaxial cavity. Plot B and C represent resonant modes of whole coaxial magnetron structure, including the external coaxial cavity.

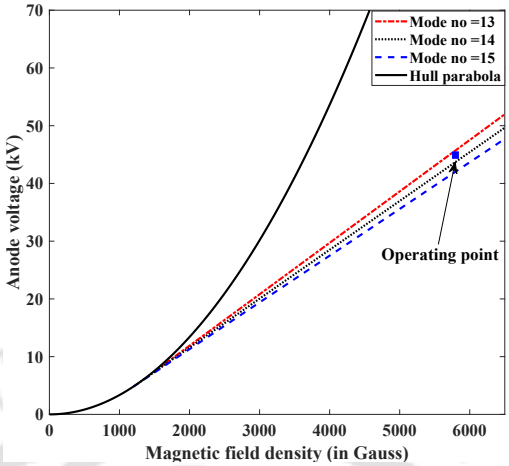

Figure 3.6: Hull-Hartree diagram of the coaxial magnetron with operating point.

Hull-Hartree diagram of the proposed coaxial magnetron is plotted in Fig. 3.6. Hull-Hartree diagram is plotted based on the expressions of the Hull cutoff voltage and Hurtree threshold voltage, given in (3.10) and (3.11) [66]. Hartree line for π-mode (mode no 14), ($\pi \pm 1$) mode (mode no 13, 15) are depicted in Fig. 3.6. The operating point of the coaxial magnetron is chosen in the operating region as per the π-mode. The operating point can be further optimized using PIC analysis. Magnetic field density (B) is obtained as 5795 Gauss for a specified anode voltage (45 kV).

$$V_c = \frac{e}{8m} B^2 r_a^2 \left(1 - \frac{r_c^2}{r_a^2}\right)^2 \tag{3.10}$$

$$V_H = \frac{r_a^2}{2}\left(1 - \frac{r_c^2}{r_a^2}\right)\frac{\omega}{n}B - \frac{r_a^2}{2}\left(\frac{m}{e}\right)\left(\frac{w}{n}\right)^2 \tag{3.11}$$

where e, m, r_c, r_a, B, V_c, and V_H are charge on electron, electron mass, cathode radius, anode radius, external magnetic field, Hull cutoff voltage, and Hartree threshold voltage, respectively. n and ω are mode number and corresponding resonant frequency of mode, respectively.

3.3.2 Frequency-domain Simulation

Coupling of a microwaver resonator can be categorized into three types: under coupling, critical coupling, and over coupling based on the values of coupling coefficient (β). Coupling coefficient (β) can be defined in terms of unloaded and external Q-factors (Q_0, Q_{ext}) as [67]: $\beta = \frac{Q_0}{Q_{ext}}$. Further, β is related to $VSWR$ as expressed in (3.12). Over coupling ($\beta > 1$) is desired for magnetron applications

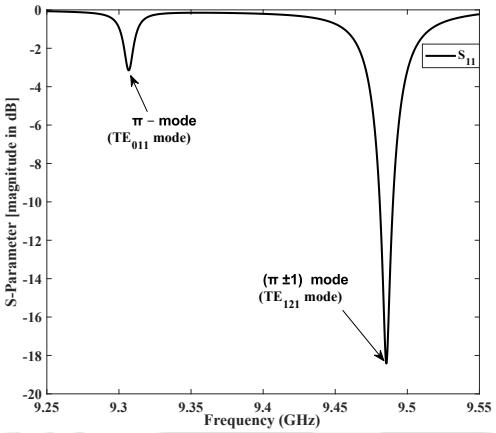

Figure 3.7: S_{11} parameter of the coaxial magnetron.

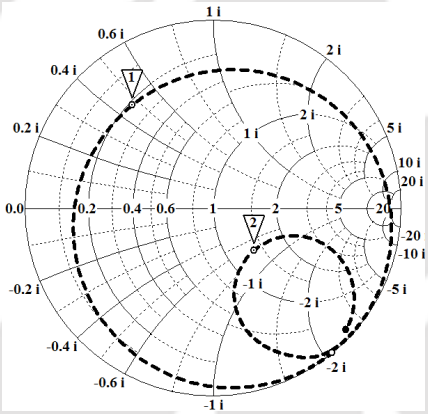

Figure 3.8: S_{11} parameter in the impedance smith chart. Marker 1 denotes circle representing TE_{011} mode and marker 2 denotes circle representing TE_{121} mode.

as high β leads to high quality factor (Q).

$$VSWR = \begin{cases} 1/\beta & \text{for under coupling} \\ 1 & \text{for critical coupling} \\ \beta & \text{for over coupling.} \end{cases} \tag{3.12}$$

The type of coupling and return loss of magnetron are calculated from frequency-domain analysis. The output section of coaxial magnetron consists of WR112 waveguide section. A waveguide-port is applied at the opening of the WR112 section for determining S-parameter in frequency-domain analysis. waveguide-port is a matched termination and it absorbs the incident power. Return losses of

the desired π-mode (TE_{011} mode) and competing modes ($\pi \pm 1$ mode) are shown in Fig. 3.7. π-mode and TE_{011} mode occur at the same resonant frequency. A significant frequency difference of 180 MHz is observed in the neighboring mode and π-mode. The type of coupling or nature of coupling is identified by impedance Smith chart, which is shown in Fig. 3.8. In impedance Smith chart, circle 1 represents over coupling which refers to TE_{011} mode. TE_{121} mode is represented by circle 2, and indicates under coupling. The circle passing through the center of Smith chart represents critical coupling in the resonator. Similarly, when circle doesn't contain the center of Smith chart (center is outside of the circle) indicates undercoupled circuit. For overcoupled circuit, circle contains the center of Smith chart. In magnetron operation, over coupling condition is desired in the operating mode. Cold test parameters such as coupling coefficient (β), circuit efficiency (η_c), and Q-factors (Q_0, Q_l, and Q_{ext}) are determined using S-parameter (S_{11}) and expressions given in (3.13).

$$Q_l = \frac{Q_0}{1+\beta} = \frac{f_r}{f_+ - f_-}, \tag{3.13}$$

where f_r is resonant frequency of TE_{011} mode and $\beta = \frac{Q_0}{Q_{ext}}$. f_+ and f_- are upper and lower 3 dB frequencies, respectively.

Coupling coefficient (β), circuit efficiency (η_C), unloaded quality factor (Q_0), loaded quality factor (Q_l), and external quality factor (Q_{ext}) are obtained as 5.57, 84%, 5883, 895, 1055, respectively. The obtained η_C from the frequency-domain analysis is slightly higher than the assumed η_C (80%) in the calculation of anode dimensions.

3.4 Optimization of Coupling Slots in the Anode Shell

The coupling slots in the common wall of the anode shell and outer coaxial cavity are shown in Fig. 3.3. The dimensions of longitudinal coupling slots present in the anode shell need to be optimized. RF coupling from the vane cavities to the outer coaxial cavity should be proper for sustaining oscillations in a coaxial magnetron. When the magnetron geometry is realized in 3D EM simulator like CST, the coupling of the slots may not be analyzed separately, as these slots become inaccessible for placement of waveguide-ports. This problem has motivated us to propose and design a mode launcher which will

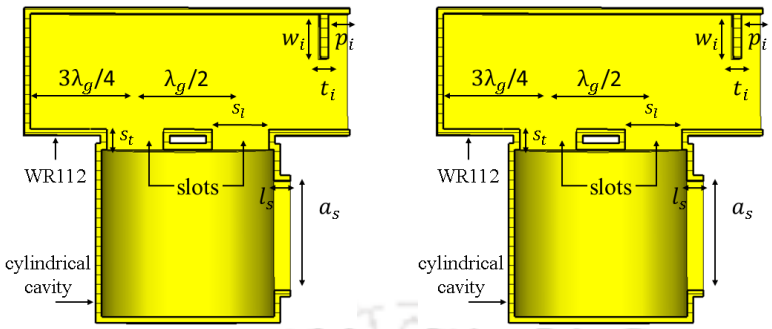

Figure 3.9: Design of TE_{011} mode launcher to a cylindrical cavity. (a) A cut-view of the design with geometrical parameters. (b) Side-view of the design with port definition.

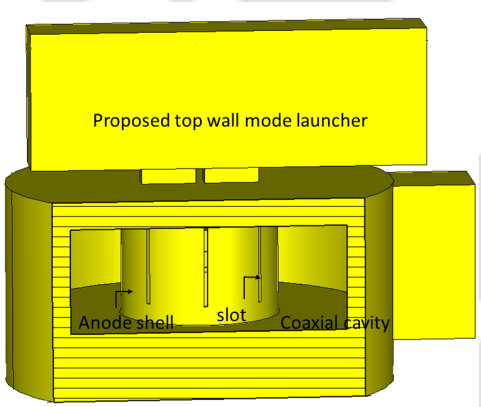

Figure 3.10: A cut-view of the proposed top wall mode launcher applied to coaxial magnetron structure.

have the similar field configuration inside the cavity, as that of the coaxial magnetron anode and the slots' coupling parameters can be studied independently by placement of a waveguide-port at the outer wall of the cavity where the slot is present. For this analysis, a rectangular to cylindrical cavity top wall mode launcher is proposed for launching TE_{011} mode in the cylindrical cavity, as shown in Fig. 3.9.

Anode shell in a coaxial magnetron can be considered as a cylindrical cavity, and the electric field present in the slot containing vane cavity for π-mode operation is similar to the circulating TE_{011} mode in the cylindrical cavity. As the anode shell is surrounded by the outer coaxial cavity, sidewall excitation from WR112 is cumbersome. This is the reason why a top wall mode launcher is proposed for the desired TE_{011} mode excitation. Also, the performance of the top wall mode launcher is better in terms of return loss, insertion loss, tunability range and quality factors, as discussed in detail in

Appendix C.

This independent study of coupling helps to fine-tune the coupling slot dimensions and positions to be used in the actual coaxial magnetron. The proposed top wall mode launcher applied to the coaxial magnetron structure is shown in Fig. 3.10. From this Fig. 3.10, it is clear that sidewall mode launching is not feasible because of geometrical constraints.

3.5 Effects of Surface Roughness on the Cold Test Parameters

The effects of surface roughness of copper are also analyzed considering the manufacturing tolerance of the device. The finite conductivity of copper is considered as 5.8×10^7 Sm^{-1}, which is actually the bulk conductivity. For high-frequency operations, skin effect needs to be taken into consideration. The effect of skin depth is considered by the field solvers in commercial EM simulators such as CST Studio. However, the effects of surface roughness need to be studied and specified separately to the field solvers. The effects of surface roughness on the performance of magnetron is presented in this section.

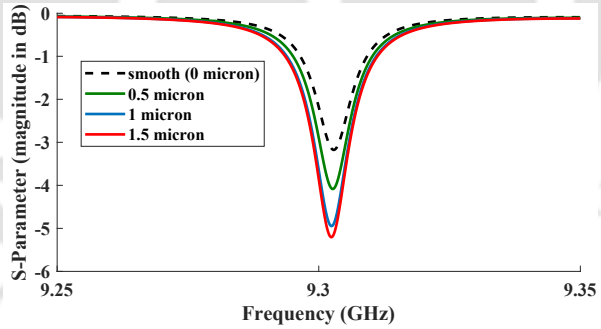

Figure 3.11: Effects of surface roughness on return loss.

Table 3.2: Effects of surface roughness on cold test parameters

R_q	f_r	Q_0	Q_l	Q_{ext}	β	η_C
0 μm	9.303 GHz	5883	895	1055	5.57	84%
0.5 μm	9.303 GHz	4351	816	1004	4.33	81.2%
1 μm	9.303 GHz	3512	762	973	3.61	78.3%
1.5 μm	9.303 GHz	3329	750	968	3.44	77.5%

The bulk conductivity remains constant but the effective conductivity changes when surface roughness is also considered in the simulation. A frequency-dependent effective conductivity is introduced in a smooth surface conductor to account for surface roughness [68]. The effective conductivity of a particular rough copper wall is $\sigma_c = \sigma/\kappa$, where σ = 5.8 $\times$ 10^7 Sm^{-1} is the bulk conductivity of the smooth conductor. The parameter $\kappa = (\alpha_c/\alpha_{c0})^2 \geq 1$. α_c and α_{c0} are the attenuation constants due to conductor losses for smooth conductor surface and rough conductor surface, respectively [69].

The effects of surface roughness are incorporated in terms of the effective conductivity [69] for broadband simulation frequencies in CST. Effective conductivity is determined based on the gradient model of surface roughness [68]. Variations in return loss are shown in Fig. 3.11, and cold test parameters are presented in Table 3.2. Here, surface roughness is represented by R_q, which is a root-mean-square roughness. R_q=0 μm roughness means smooth copper surface is considered. Q-factor decreases with the increase in surface roughness, as shown in Table 3.2. Typically, up to 0.3-0.5 μm surface finishing can be achieved and for mm-wave applications, nanoscale surface roughness can also be achieved [70, 71].

3.6 Summary

This chapter presents the design of primary sub-parts of a coaxial magnetron. A systematic design procedure of anode resonator synthesis is given along with the output section and frequency tuner design. Eigenmode simulation is carried out to determine the desired operating mode, competing modes, and dispersion diagram of the coaxial magnetron. Cold test parameters such as return loss, quality factors (Q_0, Q_l, Q_{ext}), coupling coefficient, and circuit efficiency are determined from the frequency-domain analysis. A rectangular waveguide to cylindrical cavity mode launcher is proposed to fine-tune the coupling slots present in the anode shell's wall. Effects of surface roughness on the cold test parameters are also studied considering the effective conductivity of copper.

4

Slot Modes and Suppression Technique

Contents

In this chapter, identification of slot modes and their suppression technique is presented. The analysis is carried out for X-band coaxial magnetron. It is found that slot modes occur in pair, and the slot mode having lower operating frequency is more likely to interfere with the operation of desired π-mode of coaxial magnetron. A technique for such slot mode suppression is presented, which can suppress the unwanted mode without affecting the desired mode excitation significantly. In this approach, a lossy dielectric ring is placed near the longitudinal coupling slots inside the anode shell. The effects of slot mode suppression are analyzed in eigenmode solver of CST. The slot mode suppressor also suppresses the electric field strength of fringing field of the slot mode without affecting the electric field strength of the desired π-mode. In this chapter, 16 vanes are considered in anode resonator for illustrating the method of slot mode suppression, same technique is also followed for 28-vane coaxial magnetron discussed later in chapter 5.

4.1 Introduction

Effective suppression of spurious mode excitation is a key concept of a coaxial magnetron design. The operation of coaxial magnetron suffers with the excitation of unwanted modes such as slot modes and TE_{121} mode [64, 72]. Suppression of these spurious modes is vital for operating coaxial magnetron in the desired mode. TE_{121} mode occurs because of external coaxial cavity and slot modes occur because of the coupling slots between vane resonators and external coaxial cavity. Suppression technique of TE_{121} mode has already been discussed in chapter 2, but slot mode suppression requires further investigation.

This chapter presents the identification and suppression technique for the unwanted slot modes. The electric field pattern of slot modes replicates the electric field pattern of the desired π-mode. As stated earlier, it is found that slot modes occur in pair, one mode occurs at the lower operating frequency than π-mode, and other mode occurs at a higher frequency than π-mode. Based on their operating frequencies, slot modes are referred to as lower slot mode and higher slot mode in this chapter. In order to suppress slot modes, a lossy dielectric ring is placed near to the coupling slots in anode shell. The unwanted mode suppressor should not affect the excitation of desired mode. Therefore, dimensions and dielectric properties such as dielectric constant and loss tangent of the

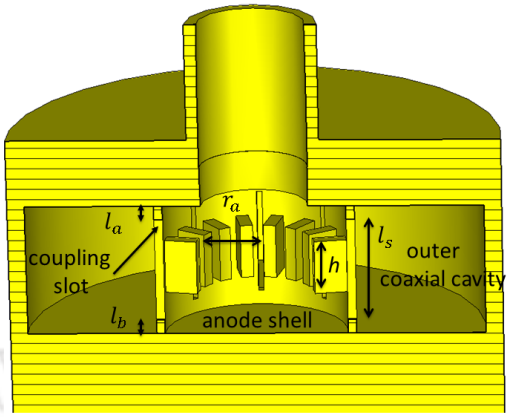

Figure 4.1: Axial cross-sectional view of the coaxial magnetron showing anode shell and outer coaxial cavity.

dielectric material are optimized. The effects of mode suppressor are analyzed in eigenmode solver of CST by determining the quality factor of slot modes and π-mode. Apart from reducing quality factors, the unwanted mode suppressor also significantly reduces the electric field strength of the fringing field produced by the slot modes.

This chapter is organized into four sections. Section 4.2 presents the slot mode identification by analyzing electric field patterns. For this, analysis is performed in eigenmode solver. Slot mode suppression technique is discussed in Section 4.3, and Section 4.4 concludes this chapter.

4.2 Identification of Slot Modes

A coaxial magnetron contains one additional outer coaxial cavity, which surrounds the anode shell. A cross-sectional view of the coaxial magnetron is shown in the Fig. 4.1. In the coaxial magnetron structure, anode shell has multitude of vane-type resonators. These vane-type resonators are coupled to the outer coaxial cavity through coupling slots in the common wall of the alternate vane-type resonators. The dimensions of coaxial magnetron related to this analysis are represented by anode radius (r_a), vane height (h), and coupling slot length (l_a). Slots are l_a and l_b distance apart from the top and bottom walls of the coaxial cavity, respectively, as shown in Fig. 4.1. Coaxial magnetron operates in TE_{011} mode in the external coaxial cavity and π-mode in anode shell, as discussed in chapter 3. The operating modes of coaxial magnetron can be determined by the electric field pattern at the desired operating frequency, as shown in Fig. 4.2.

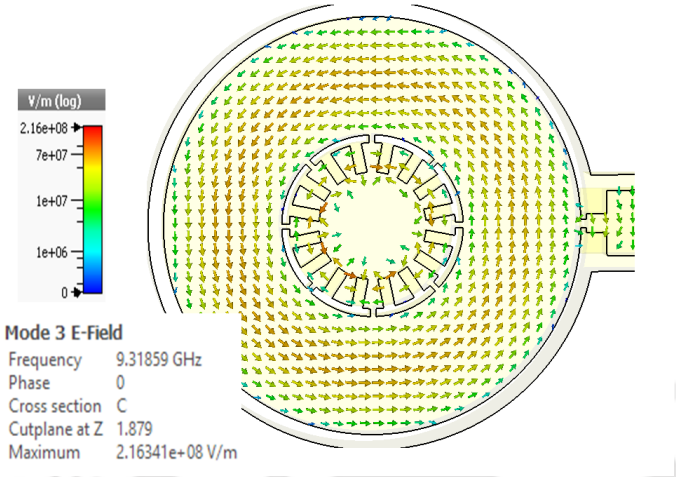

Figure 4.2: E-field vector plot of the desired mode of coaxial magnetron at the operating frequency of 9.3 GHz.

Suppression of the spurious modes is required for the proper operation of coaxial magnetron, such modes primarily include slot modes and TE_{121} mode. TE_{121} mode occurs due to the outer coaxial cavity in the magnetron. Suppression technique of TE_{121} mode has already been discussed in detail in chapter 2. However, unwanted slot modes get excited because of the coupling slots present in the common wall of anode shell and outer coaxial cavity. It is found from the analysis of simulation results that if length of the slot, $l_s \leqslant h$, no slot mode occurs but these smaller coupling slots are also not able to excite desired TE_{011} mode in the external coaxial cavity. However, the excitation of TE_{011} mode is needed for efficient operation of coaxial magnetron.

For the efficient coupling of EM fields from the anode shell to external coaxial cavity in the desired TE_{011} mode, coupling slot lengths (l_s) should be larger than the height of vanes (h). But increased slot length also generates unwanted modes, which are known as slot modes. Electric field patterns of slot modes are similar to the field pattern of desired π-mode. However, slot modes occur in pair: lower slot mode and higher slot mode [72].

Identification of slot modes and π-mode can be carried out by analyzing electric field pattern obtained from eigenmode analysis. Electric field patterns of the π-mode, lower slot mode and higher slot mode at the operating frequencies of 9.3 GHz, 7 GHz, and 11.6 GHz, respectively are shown in Fig. 4.3. In π-mode field pattern, the electric field in the slot containing vane cavity of anode (shown by a smaller circle) and external coaxial cavity (shown by a larger circle) are 180° out of phase, as

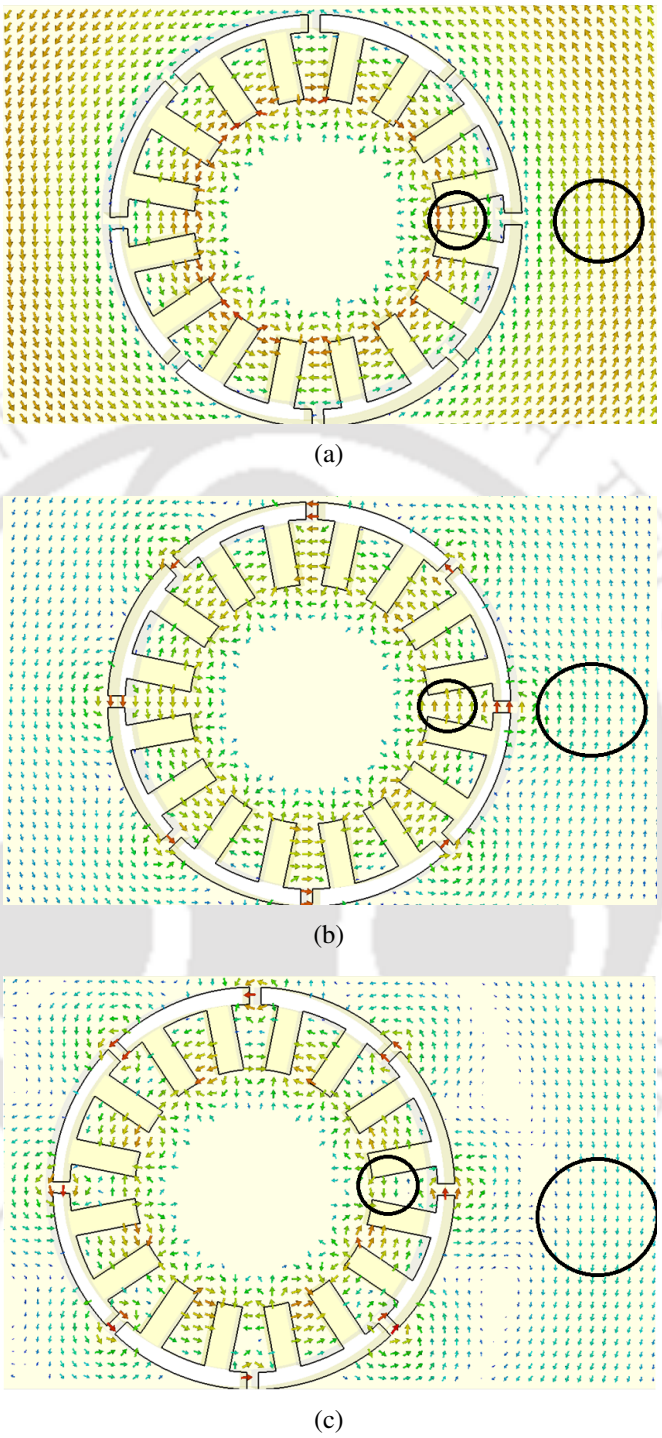

Figure 4.3: Zoomed-view of the anode shell showing E-field vector plot of various modes. (a) π-mode at 9.3 GHz. (b) Lower slot mode at 7 GHz. (c) Higher slot mode at 11.6 GHz.

depicted in Fig. 4.3 (a). However, slot modes have electric field in the same phase, as shown in Fig. 4.3 (b) and 4.3 (c). Moreover, the lower slot mode is prominent and more likely to excite, out of the

two slot modes. This is found by analyzing the Hull-Hartree diagram. The operating condition of a magnetron is obtained from the Hull-Hartree diagram analysis, as shown in Fig. 4.4, and most likely excitable modes other than the desired mode can also be identified. Hull-Hartree diagram is obtained from the Hull cutoff voltage and Hartree threshold voltage, as expressed in 4.1 and 4.2 [66].

$$V_c = \frac{e}{8m} B^2 r_a^2 \left(1 - \frac{r_c^2}{r_a^2}\right)^2 \tag{4.1}$$

$$V_H = \frac{r_a^2}{2}\left(1 - \frac{r_c^2}{r_a^2}\right)\frac{\omega}{n}B - \frac{r_a^2}{2}\left(\frac{m}{e}\right)\left(\frac{w}{n}\right)^2 \tag{4.2}$$

where e, m, r_c, r_a, B, V_c, and V_H are charge of the electron, mass of the electron, cathode radius, anode radius, external magnetic field, Hull cutoff voltage, and Hartree threshold voltage, respectively. n and ω are mode number and corresponding mode resonant frequency, respectively. In this analysis, n is taken as 8 for π-mode (corresponding to 16 vane cavities in anode shell). Since slot modes also have similar electric field patterns as that of π-mode, hence, the value on n can be considered as the same. The threshold voltage (4.2) is plotted for all three modes considering respective resonant frequencies in Fig. 4.4. In this analysis, anode voltage of the coaxial magnetron is assumed as 40 kV and the corresponding operating point is shown in Fig. 4.4. According to Hull-Hartree diagram, excitation of higher slot mode is not possible for the given operating point. Lower slot mode is more likely to get excited during coaxial magnetron operation. Thus, suppression of this mode is essential and mode suppression technique is discussed in Section 4.3.

4.3 Suppression Technique of Slot Modes

Suppression of slot modes is essential for the proper operation of a coaxial magnetron, and unwanted modes can be suppressed by significantly reducing the quality factors of those modes. But this mode suppression technique should not affect the operation of desired π-mode of magnetron. Q-factors are determined from eigenmode analysis. Q-factors of π-mode and lower slot mode without mode suppressor are obtained as 12300 and 2092 at 9.31 GHz and 7 GHz, respectively. A lossy dielectric ring is introduced near coupling slots inside the anode shell for the reduction of Q-factors of unwanted modes, as shown in Fig. 4.5.

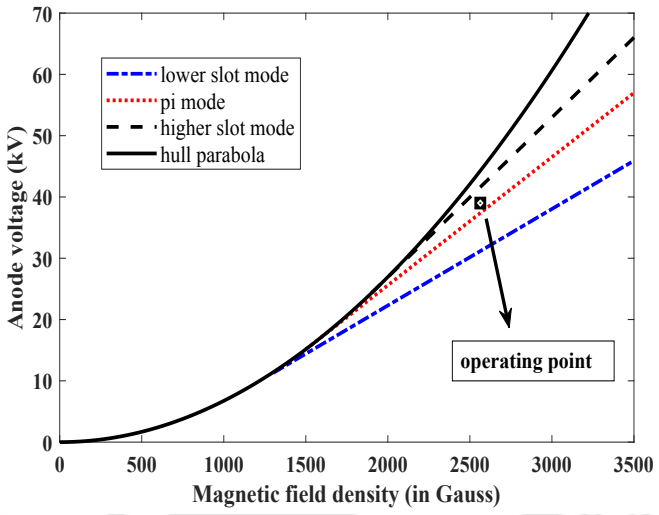

Figure 4.4: Hull-Hartree diagram of coaxial magnetron, representing threshold voltages for both slot modes and π-mode.

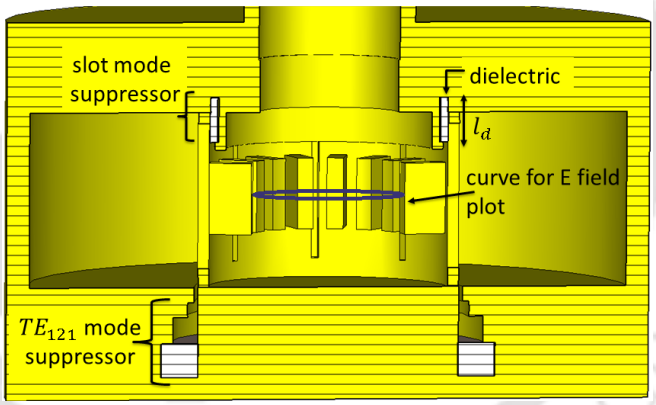

Figure 4.5: An axial cross-sectional view of the coaxial magnetron with spurious mode suppression technique. Circle indicating the curve for which E-field is plotted.

Table 4.1: Effect of dielectric constant (ϵ_r) on slot mode and π-mode

ϵ_r	f_{slot}	Q_{slot}	f_π	Q_π
16	6.5 GHz	66	9.31 GHz	5740
18	6.37 GHz	48	9.31 GHz	10020
20	6.2 GHz	37	9.31 GHz	10230
22	6.05 GHz	30	9.31 GHz	10913
24	5.86 GHz	27	9.31 GHz	9360
26	5.7 GHz	25	9.31 GHz	7810

Table 4.2: Effect of loss tangent ($\tan\delta$) on slot mode and π-mode

$\tan\delta$	f_{slot}	Q_{slot}	f_{π}	Q_{π}
0.01	6.05 GHz	141	9.31 GHz	11486
0.05	6.05 GHz	30	9.31 GHz	10913
0.1	6.05 GHz	15	9.31 GHz	8507
0.5	6.05 GHz	3	9.31 GHz	3952

In this analysis, dimensions of dielectric material (ceramic) are represented by dielectric height (l_d), and dielectric thickness is considered as 1 mm. A cylindrical choke is used to hold the dielectric. Dimensions of the dielectric ring, choke, and dielectric properties such as dielectric constant and loss tangent of the ceramic ring are optimized to damp out undesired slot mode while keeping the desired π-mode not getting affected significantly. TE_{121} mode suppressor is also shown in Fig. 4.5, which is already discussed in chapter 2. The Q-factors of π-mode and lower slot mode are calculated from eigenmode analysis in CST. Effects of the variation of loss tangent, dielectric constant, dielectric height (l_d), and coupling slot distance from the top wall of the coaxial cavity (l_a) on the Q-factors and resonant frequencies of π-mode and lower slot mode are studied. The resonant frequency of the π-mode remains unaffected by such variations. Resonant frequency of the π-mode is decided by the vane cavity and external coaxial cavity. Q-factor of π-mode (Q_{π}) increases with ϵ_r, and starts reducing after ϵ_r value of 22, as presented in Table 4.1. However, it is found that resonant frequency of lower slot mode (f_{slot}) is inversely proportional to ϵ_r and Q-factor (Q_{slot}). The optimum value of ϵ_r, can be chosen as 22, at which Q_{slot} is suppressed to 30 keeping Q_{π} is at 10913.

The resonant frequencies of both lower slot mode and π-mode have been found to remain unaffected by the variation in loss tangent value, as shown in Table 4.2. However, increment in loss tangent reduces the Q-factors, as it increases losses in the structure. The optimum value of the loss tangent is obtained as 0.05. Effects of coupling slot distance (l_a) from the top wall of coaxial cavity and dielectric height (l_d) are presented in Table 4.3 and 4.4, respectively. It is found that resonant frequency of lower slot mode (f_{slot}) is proportional to l_a, and inversely proportional to dielectric height (l_d). The optimum values of l_a and l_d are obtained as 0.5 mm and 5 mm, respectively. By this slot

Table 4.3: Effect of coupling slot distance from top wall (l_a) on slot mode and π-mode

l_a	f_{slot}	Q_{slot}	f_π	Q_π
0.5 mm	6.05 GHz	30	9.31 GHz	10913
1.5 mm	6.43 GHz	33	9.31 GHz	9749
2.5 mm	6.74 GHz	33	9.31 GHz	9200
3.5 mm	6.98 GHz	34	9.31 GHz	9227
4.5 mm	7.23 GHz	36	9.31 GHz	9290

Table 4.4: Effect of dielectric length (l_d) variation towards the vanes on slot mode and π-mode

l_d	f_{slot}	Q_{slot}	f_π	Q_π
3 mm	6.84 GHz	210	9.31 GHz	8384
4 mm	6.62 GHz	73	9.31 GHz	9563
5 mm	6.05 GHz	30	9.31 GHz	10913
6 mm	5.4 GHz	24	9.31 GHz	8599
7 mm	5.04 GHz	24	9.31 GHz	7291

mode suppressor, Q-factor of slot mode is reduced significantly by 98.56% at the cost of just 11% reduction in Q-factor of π-mode.

Excitation of slot mode also depends upon the electric field strength of the fringing field from the vane cavities. This fringing field corresponding to different modes, accelerates and decelerates electrons in the space charge region as per their field strength and phase. Electric field strength is plotted in Fig. 4.6 along with the circle (which is shown in Fig. 4.5) near the vane tips. In the coaxial magnetron, higher electric field strength is observed for π-mode as shown in Fig. 4.6. The operating point of coaxial magnetron also lies above the threshold of Hartree line of lower slot mode (Fig. 4.4). Thus, when no mode suppressor is employed, electrons start bunching as per the slot mode and magnetron gets locked into slot mode instead of desired π-mode operation. After applying the mode suppressor technique, electric field strength of the slot mode also significantly reduces as shown in Fig. 4.6(b). However, mode suppressor doesn't affect the electric field strength of π-mode,

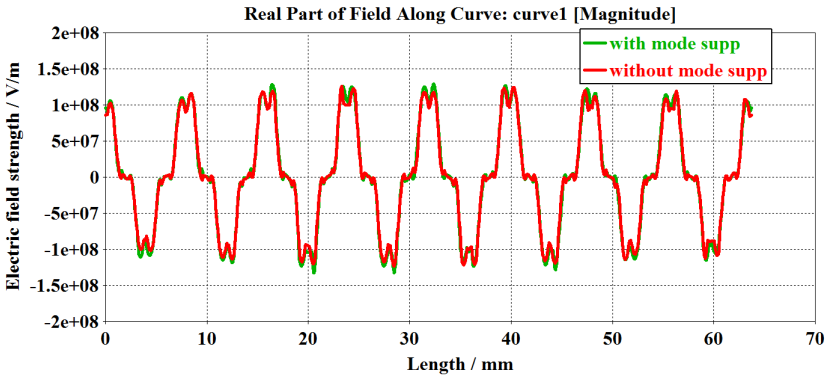

(a)

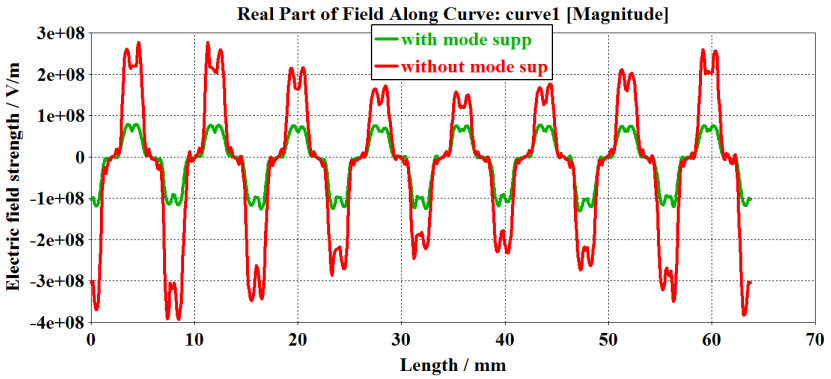

(b)

Figure 4.6: Effect of the proposed slot mode suppressor on the electric field strength of π-mode and slot mode along the circular curve near tips of vanes. (a) Effect on π-mode. (b) Effect on slot mode.

as depicted in Fig. 4.6(a).

4.4 Summary

This chapter presents a crucial aspect of coaxial magnetron design. Spurious modes' excitation make the coaxial magnetron design challenging. Suppression of slot modes is essential for the proper operation of coaxial magnetron, and it can be considered as a key design aspect of coaxial magnetron. Electric field patterns of slot modes are similar to π-mode pattern, hence, proper identification of such undesired modes is necessary. It is found that slot modes occur in pair and lower slot mode is prominent and more likely to excite than higher slot mode. A slot mode suppression technique is discussed considering a lossy dielectric ring inside the anode shell near to the coupling slots. Slot mode suppressor is designed such a way that it can effectively suppress unwanted mode without

affecting desired mode considerably. Effects of dielectric constant, loss tangent, dielectric height, slot distance from the top wall of the cavity on the resonant frequencies of the modes and quality factors are studied. Optimized values of ϵ_r, $\tan\delta$, l_a, l_d, are obtained as 22, 0.05, 0.5 mm, and 5 mm, respectively. Q-factor of slot mode is reduced after employing mode suppression technique to 30 keeping Q-factor of π-mode as 10913. Q-factor of slot mode is reduced significantly by 98.56% at the cost of just 11% reduction in Q-factor of π-mode. The slot mode suppressor also reduces the fringing field present in the slot mode while keeping the field strength of desired π-mode unaffected.

भारतीय प्रौद्योगिकी संस्थान गुवाहाटी
Indian Institute of Technology Guwahati

5

Particle-in-Cell (PIC) Simulation of Coaxial Magnetron and Efficiency Improvement

Contents

The design procedure of coaxial magnetron and cold test analysis have been presented in chapter 3. This chapter presents the output performance analysis of coaxial magnetron using particle-in-cell (PIC) simulations. The output of coaxial magnetron is taken from the standard WR112 waveguide section through a rectangular coupling slot on the outer wall of the coaxial cavity. Operating point of the magnetron is obtained from the Hull-Hartree diagram. Output power and total efficiency of the magnetron is further optimized by varying applied magnetic field in the operating region of π-mode. Some additional studies are also performed to improve the efficiency as well for understanding the effect of copper surface roughness and variation in properties of dielectric materials used in slot mode suppressor. Effect of cathode end hats' shape on output performance is studied. The shape of the cathode end hats of coaxial magnetron is found to affect the efficiency and when the shape is changed from conventional to conical, 2.74% improvement in the total efficiency is observed. The output performance of the coaxial magnetron is analyzed for the variations in dielectric properties of the slot mode suppressor. Effect of surface roughness of copper on output performance of the magnetron is studied through PIC analysis.

5.1 Introduction

Magnetrons are widely used vacuum electron devices (VEDs) because of their compact size and high-efficiency. A magnetron can be continuous wave (CW) type or pulsed power type based on output power. Magnetrons have a wide range of applications: continuous wave (CW) magnetrons have applications in heating and pulsed power magnetrons have applications in accelerators. Recently, 40-vane pulsed power coaxial magnetrons are designed for X-band operation [11, 41]. Peak output powers are reported as 1.61 MW with 50.8% efficiency [11] and 1.88 MW with 53% efficiency [41] at operating frequency of 9.3 GHz. In this chapter, a 28-vane coaxial magnetron is designed to provide a higher peak output power of 2.12 MW with higher efficiency of 62.04% at the 9.2987 GHz operating frequency. Particle-in-Cell analysis is performed using PIC solver of CST. 45 kV anode voltage is considered in PIC simulation of coaxial magnetron. Input signal from pulsar is considered having duty cycle of 0.001 with 4 μs pulse width.

The key contributions of this chapter are as follows:

- A coaxial magnetron with 28-vane anode is designed for 2.12 MW peak and 2.12 kW average output powers. The total efficiency of 62.04% is achieved at 9.2987 GHz operating frequency. Frequency tuning characteristics of the coaxial magnetron is also analyzed and frequency tuning range is found to be 40 MHz.

- The output power and efficiency of the magnetron is optimized by varying magnetic field strength. It is found that peak output power higher than 2.12 MW can also be achieved but at a slightly lower efficiency.

- Effect of cathode end hats' shape is studied. Use of conical end hats resulted in an improvement of the coaxial magnetron's efficiency by 2.74%.

This chapter is organized into six sections. The output performance of the coaxial magnetron is analyzed by particle-in-cell (PIC) simulations in Section 5.2. In this analysis, output power, total efficiency, anode current, and output frequency of the coaxial magnetron are determined. The effect of surface roughness of copper on the output performance of magnetron is also analyzed. The dielectric properties of the slot mode suppressor such as dielectric constant and loss tangent are optimized using PIC analysis in Section 5.3. Section 5.4 presents the efficiency enhancement of coaxial magnetron by modifying shape of the cathode end hats. Output power, anode current, and efficiency of the coaxial magnetron for conical end hats and conventional end hats are compared. Frequency tuning range is determined in Section 5.5. Section 5.6 summarizes this chapter.

5.2 Particle-in-Cell (PIC) Simulation

PIC analysis is carried out in CST studio using PIC solver. In this analysis, explosive emission model for particles is used. Electrons are considered with 5 eV initial kinetic energy and uniform distribution. The number of emission points are taken as 900 in the PIC simulation. A convergence analysis of output power is performed. Study is carried out by varying the number of emission points. The reported analysis is for 8.8×10^4 number of electrons for which the output becomes stable. The output performance parameters such as peak power (P_{out}), anode current (I_a), and total efficiency (η_T)

are affected by the variation in the number of particles. The output performance parameters converge for the number of particles greater than 8.8×10^4, as shown in Table 5.1.

Output of the coaxial magnetron is taken from the WR112 waveguide section. A waveguide-port is defined at the opening of the WR112 section. The waveguide-port is actually a matched termination which absorbs the RF signal that appears at the output section. A DC anode voltage of 45 kV is applied using discrete port. The DC anode voltage signal is applied for a total duration of 300 ns with 5 ns as rise time. A constant magnetic field is applied along the axis of the anode resonator. The value of magnetic field is obtained as 5795 Gauss from the Hull-Hartree diagram, as discussed in chapter 3. Since anode resonator consists of 28 vanes, 14 spokes of electrons bunches are formed in the PIC simulation because coaxial magnetron is operated in π-mode, as shown in Fig. 5.1. Emission of electrons starts at the beginning of simulation but it takes some time to form electron bunches. The shape of these spokes improves with time, as shown in Fig. 5.1. Formation of spokes due to bunching of electrons at 105 ns is better than at 40 ns. This indicates proper mode operation and efficient beam-wave energy transfer at 105 ns.

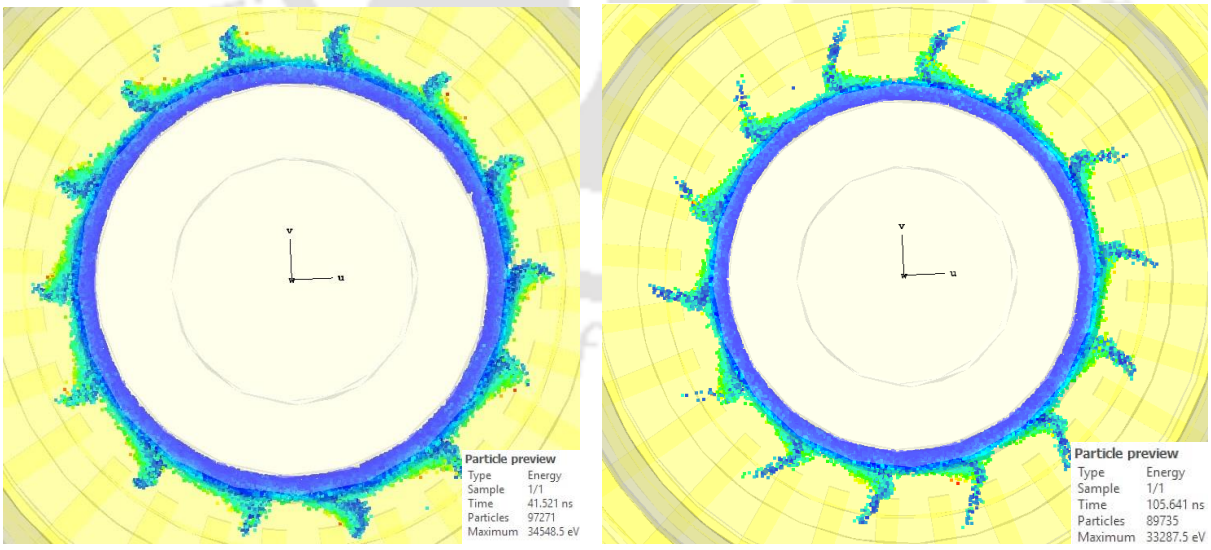

(a) (b)

Figure 5.1: Formation of electrons spokes in the desired π-mode operation. (a) Spokes formation at 40 ns. (b) Spokes formation at 105 ns.

Output power and anode current obtained from PIC simulation are presented in Fig. 5.2 (a). The output signal saturates after around 120 ns time, and 2.12 MW power is obtained with 76 Amp anode

current. Total output efficiency (η_T) is determined as 62.04%. No leakage current is observed as it is found from PIC analysis that electrons do not escape the interaction space because of cathode end hats. The operating frequency of coaxial magnetron can be determined from the plot of power spectral density (PSD) of the output signal, which is presented in Fig. 5.3 (g). Frequency spectrum shows that the maximum output power of the magnetron is obtained at 9.2987 GHz. Other competing modes have power levels which are at least 50 dB lower meaning that the magnetron is operating in single mode. Electronic efficiency (η_e) is calculated ($\eta_e = \eta_T/\eta_C$) using values of η_T and η_C (from frequency-domain analysis) as 73.86%. The initial values of η_C and I_a were assumed as 80% and 80 Amp, respectively, while calculating the initial dimensions of anode structure and the value of η_T is specified as 70% (in chapter 3). After introducing outer coaxial cavity, coupling slots in the anode shell and performing PIC analysis, η_T, and I_a are achieved as 62.04%, and 76 Amp, respectively. The proposed coaxial magnetron is a pulsed power magnetron. The input pulse signal is specified with 0.001 duty cycle and 4 μs pulse width. Thus, the average power is calculated as 2.12 kW.

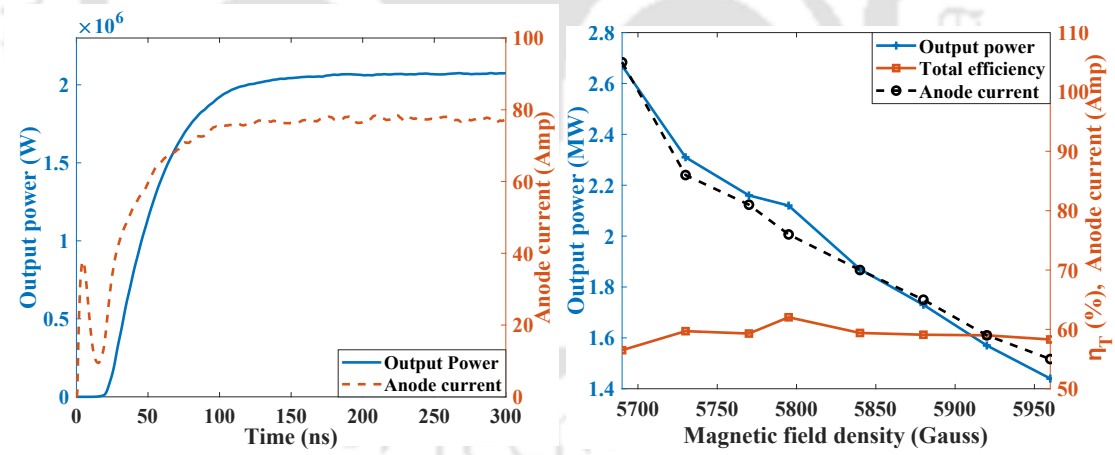

(a) (b)

Figure 5.2: Performance of the proposed coaxial magnetron. (a) Output power and anode current. (b) Effect of applied magnetic field density to output power, anode current, and total efficiency.

Efficiency (η_T) of the magnetron also depends significantly on the selection of the proper operating point in the Hull-Hartee diagram. As the anode voltage is fixed (45 kV), output efficiency of magneron can be optimized by choosing an optimal value of magnetic field (B) [34]. The effects of B on the output performance parameters such as output power, η_T, and anode current are shown in Fig. 5.2

Table 5.1: Effect of number of particles variation on PIC performance

No. of particles	P_{out} (MW)	I_a (Amp)	η_T (%)
5×10^4	2.31	90	57
6.4×10^4	2.13	79.8	59
8×10^4	2.05	76	59.88
8.8×10^4	2.12	76	62.04
9×10^4	2.12	76	62.06
1.1×10^5	2.12	76	62

Table 5.2: Effect of surface roughness of copper on PIC performance

R_q (μm)	P_{out} (MW)	I_a (Amp)	η_T (%)
0	2.12	76	62.04
0.5	2.17	81	59.5
1	2.13	85	55.8
1.5	2.098	88	53

(b). B can only be varied in the operating range of π-mode obtained from the Hull-Hartee diagram (Fig. 3.6). The maximum η_T (62.04%) is obtained at 5795 Gauss magnetic field with corresponding output power of 2.12 MW. However, the maximum output power is obtained as 2.67 MW but at a lower efficiency of 56.5% at 5690 Gauss. Further, reduction in the value of magnetic field leads to the excitation of unwanted modes. Thus, the high output power can be achieved by just modifying the applied magnetic field with a slight compromise in the efficiency as per the requirement of the application.

The effects of surface roughness of copper on the output performance of coaxial magnetron is also studied. The values of output power and efficiency decrease with the increase in the surface roughness (R_q), as presented in Table 5.2.

Information regarding computational platform, number of mesh cells, emission points, and total time taken in the simulation of the proposed coaxial magnetron is given in Appendix D.

5.3 Effects of Dielectric Constant and Loss Tangent of the Slot Mode Suppressor on the Performance

Dielectric properties such as dielectric constant and loss tangent of the slot mode suppressor are optimized using PIC analysis. These dielectric properties affect the output performance of coaxial magnetron significantly. This section presents the optimization of magnetron performance by variation of dielectric properties of the slot mode suppressor. Effects of dielectric constant (ϵ_r) variation (*e.g.* ϵ_r = 12, 16, 21, 25) are shown in Fig. 5.3. The output powers obtained from PIC simulations are shown for various cases in Fig. 5.3 (a to d) and power spectral densities (PSDs) of the output signals are shown in Fig. 5.3 (e to h). Slot mode dominates for ϵ_r = 12 case, and most of the output power is in the lower slot mode at around 7 GHz frequency, as shown in Fig. 5.3 (e), and the corresponding output power is just 250 kW (Fig. 5.3 (a)). Here, coaxial magnetron is not operating in the desired mode. Although, for ϵ_r = 16 case, π-mode is dominating and output power is also slightly more than 2 MW, but competing modes also excite along with π-mode excitation. So, ϵ_r = 16 is also not suitable for desired performance. Out of all the cases, PSD presented in Fig. 5.3 (g) has the best-unwanted mode suppression, and almost all the output power corresponds to π-mode at around 9.3 GHz frequency. Thus, the dielectric constant is chosen as 21 for the optimal performance of the slot mode suppressor. Slot mode suppressor works efficiently for this dielectric constant.

Moreover, the suppression of unwanted modes depends on the dielectric losses present in the dielectric material of mode suppressor. The output performance of coaxial magnetron is analyzed for various values of loss tangent ($\tan\delta$) such as 0.0001, 0.001, 0.01, 0.08, as shown in Fig. 5.4. For low losses, mode suppressor doesn't perform well, and unwanted modes excite instead of the desired π-mode excitation (for $\tan\delta$ = 0.0001, 0.001, 0.01 cases). However, for $\tan\delta$ = 0.08, only π-mode excites dominantly, as shown in Fig. 5.4 (h). Thus, the optimal value of $\tan\delta$ is chosen as 0.08. AlN-SiC and BeO-SiC based lossy dielectric composites are used for the vacuum electronics applications. Dielectric constant can be modified by varying content of SiC in the composite. The desired dielectric properties can be achieved by taking SiC content around 30% in the composite.

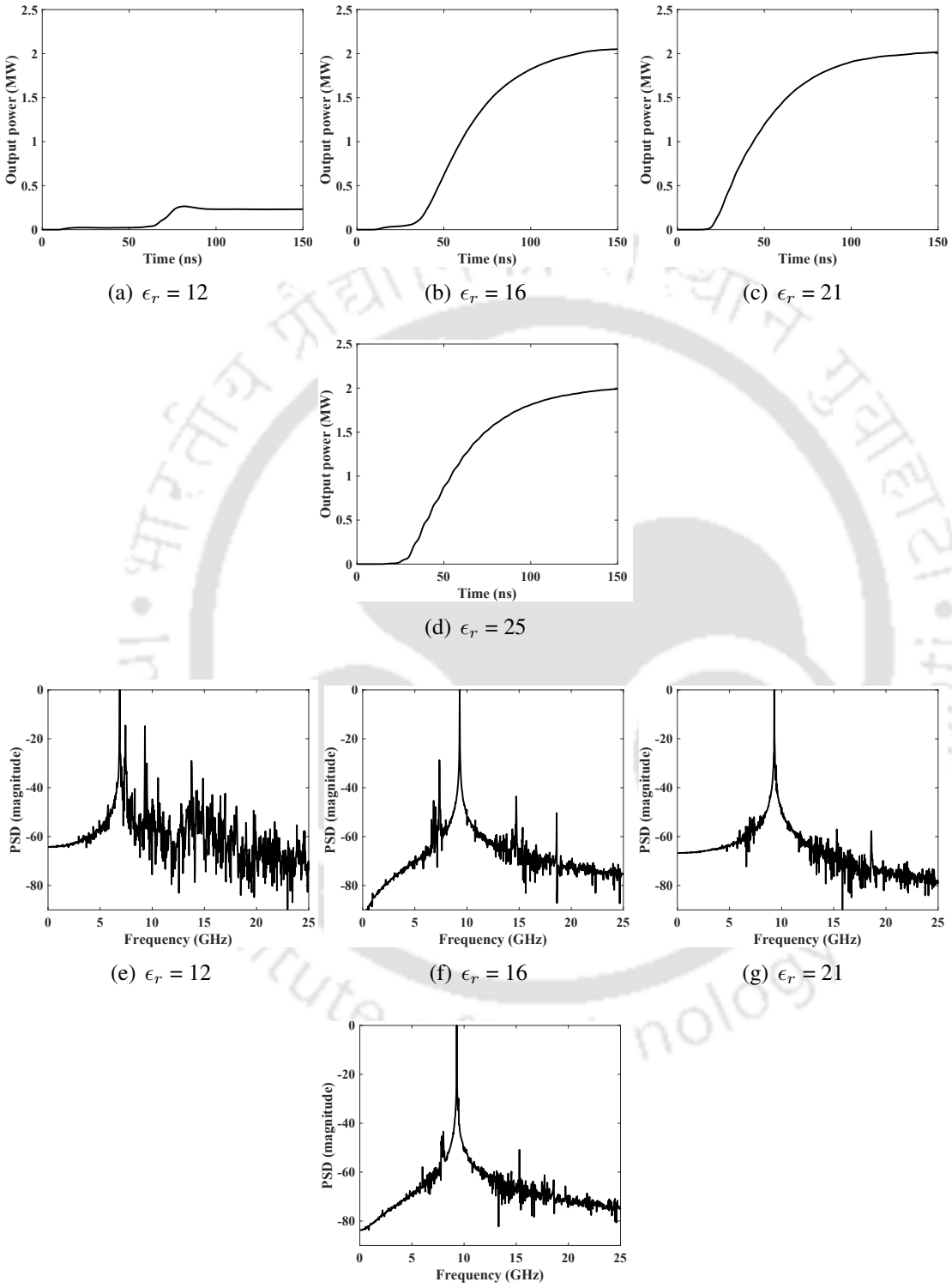

(a) ϵ_r = 12 (b) ϵ_r = 16 (c) ϵ_r = 21

(d) ϵ_r = 25

(e) ϵ_r = 12 (f) ϵ_r = 16 (g) ϵ_r = 21

(h) ϵ_r = 25

Figure 5.3: Effect of the dielectric constant of the slot mode suppressor on the output power and power spectral density (PSD) of output signal. (a-d) Effect on output power. (e-h) Effect on PSD.

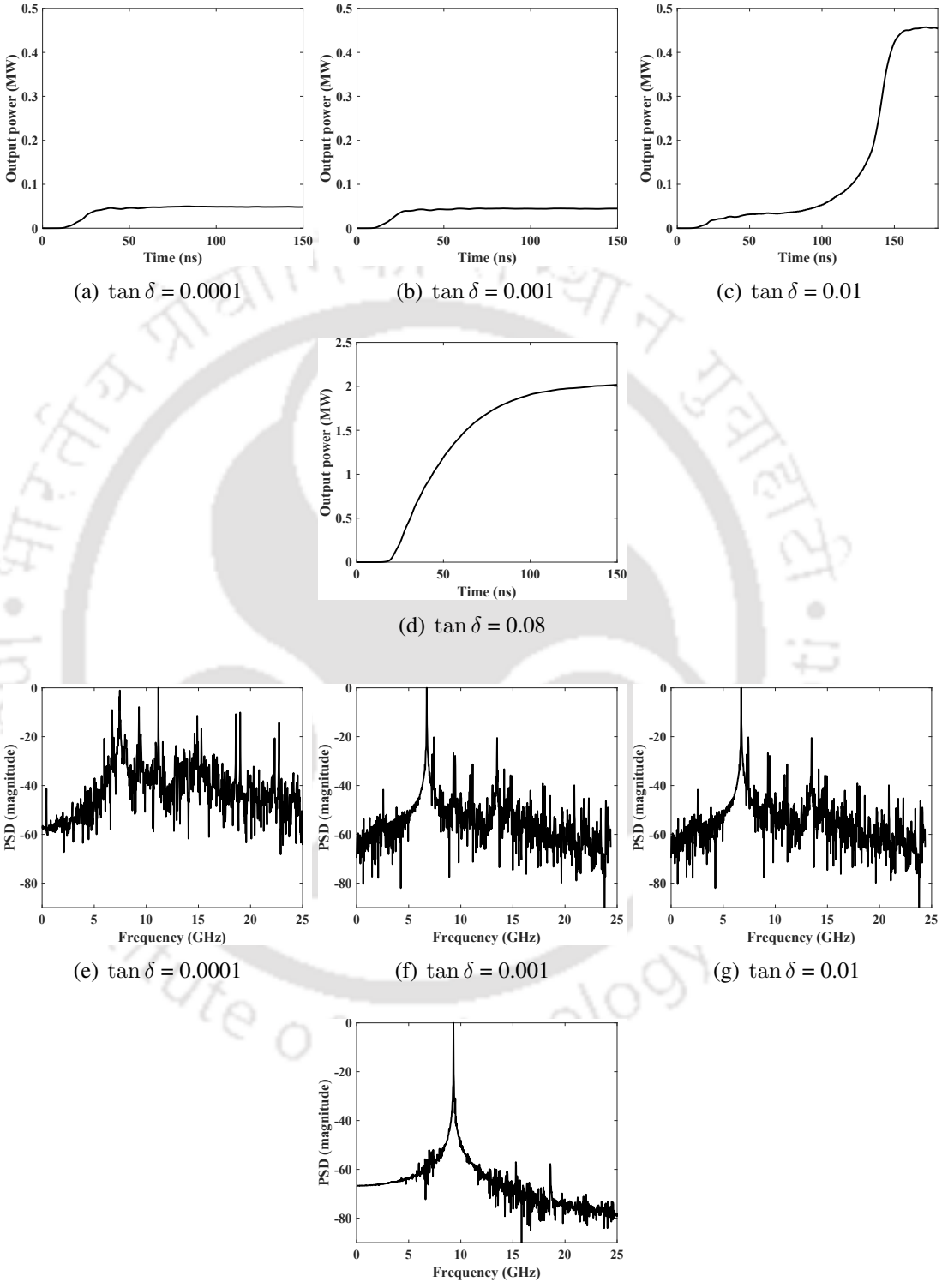

(a) $\tan\delta = 0.0001$ (b) $\tan\delta = 0.001$ (c) $\tan\delta = 0.01$

(d) $\tan\delta = 0.08$

(e) $\tan\delta = 0.0001$ (f) $\tan\delta = 0.001$ (g) $\tan\delta = 0.01$

(h) $\tan\delta = 0.08$

Figure 5.4: Effect of loss tangent $\tan\delta$ of the lossy dielectric of slot mode suppressor on the output power and power spectral density (PSD) of output signal. (a-d) Effect on output power. (e-h) Effect on PSD.

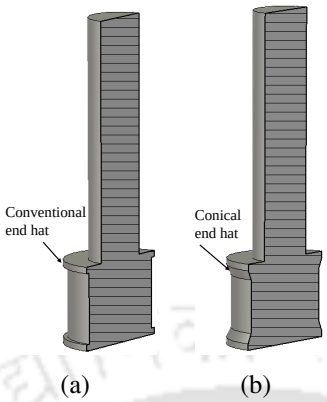

Figure 5.5: An axial cross-sectional view of cathodes (a) Cathode with conventional end hats. (b) Cathode with conical end hats.

5.4 Efficiency Improvement by Cathode End Hats' Shaping

This section deals with the efficiency enhancement of the proposed coaxial magnetron by modification of cathode end hats' shape. In conventional cathode end hat configuration, circular disks are placed at both ends of the cathode. However, in modified configuration having conical cathode end hats, disks are connected by tapering to the cathode, as shown in Fig. 5.5.

The cathode end hats are necessary to prevent the leakage of electrons from the interaction region. If end hats are not considered, electrons could escape from the interaction space, and leakage current would be observed. Cathode end hats are used to avoid such leakage/loss current. In this case, no leakage current is observed, as electrons are restricted in the interaction region after employment of the end hats. The loading effect of the conical end hats' is studied and presented in Table 5.3. Output power using cathode with conventional end hats is obtained as 2.08 MW while using conical end hats is obtained as 2.12 MW. Efficiency is also enhanced by 2.74% by introducing conical end hats. It is

Table 5.3: Effect of Cathode End Hats' Shaping

End hat shapes	Output power (MW)	I_a (Amp)	η_T
Conventional end hats	2.08	78	59.3%
Conical end hats	2.12	76	62.04%

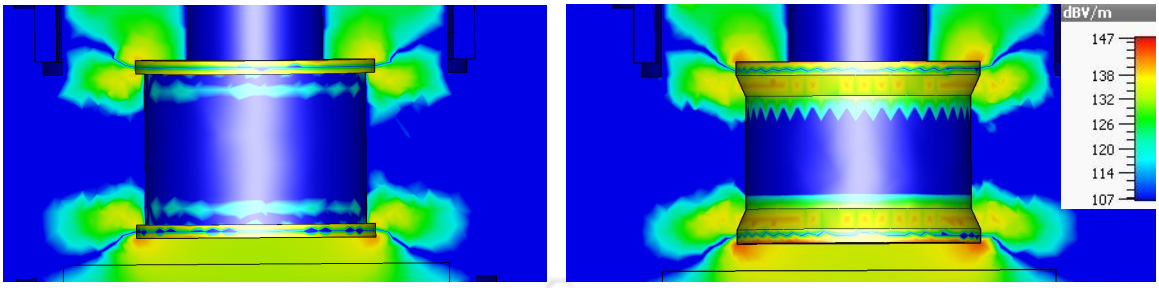

(a) (b)

Figure 5.6: Contour plot of the z-component (axial) of the static E-field. (a) Cathode with conventional end hats. (b) Cathode with conical end hats.

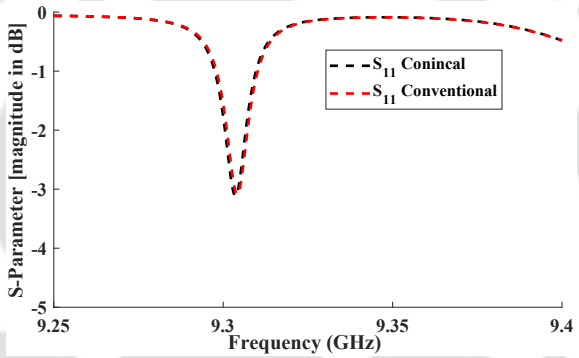

Figure 5.7: Effect of cathode end hats' shape variation on return loss.

observed that conical end hats are more efficient than conventional end hats. The axial component (z-direction) of the static electric field from anode vanes to cathode has higher value in case of conical end hats than the conventional end hats, as depicted in Fig. 5.6, which tends to move the electrons toward the interaction region. This results in an increase in electron-wave energy transfer, and higher efficiency is observed.

In order to examine the change in Q-factors because of cathode end hats' shape, the return loss is calculated in both cases, as shown in Fig. 5.7. Negligible change is observed in S_{11}, when conical cathode end hats are used instead of conventional cathode end hats. Thus, change in the shape of cathode end hats does not affect the Q-factors perceptibly. However, efficiency of the magnetron with conical cathode end hats is more because of the efficient electron-wave energy transfer, as electrons are pushed towards the interaction region.

Table 5.4: Frequency Tuning of Coaxial Magnetron

l_{cavity} (mm)	Frequency (GHz)	Output power (MW)	η_T (%)
23.60	9.2160	2.21	59.20
23.50	9.2423	2.18	59.80
23.30	9.2685	2.10	59.80
23.24	9.2783	2.12	62.00
23.10	9.2987	2.12	62.04
22.98	9.3192	2.12	62.01
22.90	9.3469	1.97	58.40
22.70	9.3735	1.89	58.50
22.60	9.3998	1.85	58.70

5.5 Frequency Tuning of Coaxial Magnetron

In this section, frequency tuning characteristics of the proposed coaxial magnetron is presented. Resonant frequency of the coaxial magnetron can be varied by changing length of the external coaxial cavity. The length of the external coaxial cavity can be varied through movement of the frequency tuner along the axial direction of the cavity, as shown in Fig. 3.3. Pushing down the frequency tuner will reduce the l_{cavity} while pulling up will increase the length of the outer coaxial cavity. The outer coaxial cavity is operated in TE_{011} mode. The resonant frequency of the desired TE_{011} mode is inversely related to the l_{cavity}, as discussed in chapter 3. The output performance is studied for various values of l_{cavity}. The effect of l_{cavity} variation is presented in Table 5.4. The output performance is studied by PIC analysis. The frequency tuning range can be decided as per the required output power and efficiency tolerance. Frequency tuning range of the coaxial magnetron is obtained as 9.2987 GHz $\pm$ 20 MHz.

5.6 Summary

The PIC analysis of a 28-vane high-power pulsed coaxial magnetron operating in X-band is presented. The coaxial magnetron is analyzed using PIC solver of CST particle studio. In this analysis, anode voltage is considered as 45 kV. The magnetic field strength is determined from the Hull-Hartree

diagram for π-mode operation. The optimal value of magnetic field is obtained as 5795 Gauss. The output peak power of 2.12 MW is achieved at 9.2987 GHz frequency with 62.04% total efficiency. The circuit efficiency and electronic efficiency of the coaxial magnetron are obtained as 84% and 73.86%, respectively. The effect of magnetic field on the output performance of the proposed coaxial magnetron is also studied. It is found that a higher output power can be achieved with a slight compromise in the efficiency at the same frequency. The maximum peak power of 2.67 MW can also be achieved at but a slightly lesser efficiency of 56.5% by just modifying magnetic field. Dielectric properties of the slot mode suppressor is optimized by PIC analysis. The efficiency of the magnetron is also affected by the shape of the cathode end hats. 2.74% efficiency improvement is observed by using conical cathode end hats. Frequency tuning range is determined as 9.2987 GHz $\pm$ 20 MHz.

6

Design and Analysis of RF Windows

Contents

Design of RF window, a critical part of the vacuum electron devices, is presented. Overmoded RF windows are designed for high-power applications such as pulsed power magnetron, klystrons, gyrotrons, and LINACs operating in X-band frequencies. Primarily, designs of RF windows for coaxial magnetron are discussed in this thesis. In this chapter, four overmoded RF windows are proposed based on the approach adopted for excitation of dominant mode. Coupled multiphysics analyses are preformed to study thermal and structural characteristics of the proposed RF windows. The sensitivity of S-parameters are analyzed to check the effects of structural deformation which is produced due to the high-pressure difference and high-power operation of the RF windows. Power handling of RF windows are limited by various factors, but chiefly multipactor restricts the operation of the RF windows. Multipactor simulations are performed to determine the multipactor threshold levels of the proposed RF windows for a safe operation.

6.1 Introduction

An RF window behaves as a barrier between vacuum and external environment. The dielectric disk plays the role of barrier in an RF window structure. RF window is a vulnerable part of vacuum devices as failure of RF window can cause permanent damage to the vacuum device. A conventional pillbox-type RF window is shown in Fig. 6.1. Power handling capacity of such RF windows are typically restricted by the multipactor effect [17]. In multipaction, avalanche of electrons occur because of the emission of secondary electrons. Secondly, operating bandwidth of these RF windows are very narrow as they generally operate in a single mode (TE_{11} mode). For such windows, the limit of multipactor threshold is enhanced by putting an antimultipactor coating at the surface of dielectric disk. A thin TiN coating is often used for antimultipaction. But the disadvantage of using TiN coating is that it can cause surface flashover on dielectric disk [19]. Hence, an alternate way is chosen which can improve the multipactor threshold without using TiN coating, and can also avoid surface flashover on the dielectric disk. The alternate method is structural modification, in which an RF window is operated in an overmoded condition instead of dominant mode. An overmoded RF window can have larger diameter of dielectric disk and thereby average power density is lowered at the disk.

Recently, an overmoded RF window having 5 MHz bandwidth is proposed for high-power klystron

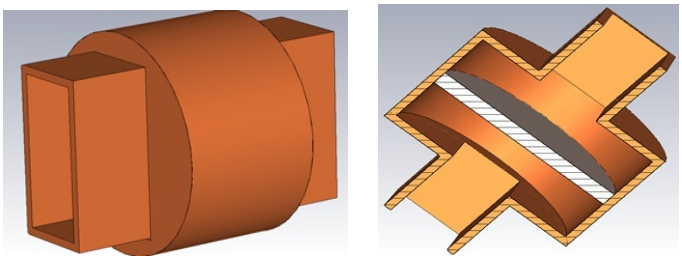

(a) (b)

Figure 6.1: Conventional pillbox-type RF window (a) Side-view (b) Cross-sectional view.

application in S-band [3]. This overmoded RF window is designed to operate in the higher order mode *i.e.* TE_{012} mode. TE_{012} mode has a circulating electric field pattern along the length of the cylindrical cavity of the RF window. TE_{012} mode RF window has a larger radius and lower electric field strength at the dielectric barrier as compared to the conventional pillbox-type RF window. The lower electric field strength at the dielectric surface reduces the breakdown possibilities, normalizes the temperature distribution and reduces localized heating. The multipactor threshold levels for such TE_{012} mode overmoded RF windows are higher even without using antimultipactor coating of TiN [3]. Another advantage of not using TiN coating in TE_{012} mode RF window is to avoid the breakdown on the coating surface or surface flashover. There is a lot of scope in the RF window design with a high multipactor threshold so that the RF window can be operated safely at high-power levels in X-band. The operating bandwidth of window can be improved by choosing a mixed mode operation over a single mode operation.

In this chapter, four types of overmoded RF windows are proposed. Out of four RF windows, three RF windows are based on the TE_{012} mode excitation approach, and one RF window is based on the excitation of TE_{022} mode in the cylindrical section of the window. For a circular waveguide TE_{11} mode is the dominant mode and TE_{01} and TE_{02} modes are higher order modes. The last index (*i.e.* 2) in TE_{012} and TE_{022} modes indicates the variation along the length, in one RF window TE_{014} mode is dominant because length is more, however, cross-sectional field is same as TE_{012} mode. These four RF windows are designed for the coaxial magnetron operating at 9.3 GHz frequency and 2 MW peak and 2 kW average power ratings, as discussed in this thesis but can also be used for

other high-power tubes such as klystron, gyrotron, and LINAC. This chapter is organized into four sections. RF window designs are discussed in Section 6.2. RF window designs are proposed based on the excitation of TE_{01} and TE_{02} modes in the cylindrical section. Simulation based studies and performance analyses are presented in Section 6.3. In simulation based analyses, frequency-domain, multiphysics, and multipactor studies are performed. Return loss, insertion loss, and VSWR of the RF windows are determined from frequency-domain simulation. In multiphysics studies, coupled electromagnetic, thermal, and structural simulations are performed. Multiphysics analyses are carried out to analyze temperature distribution and structural deformations in the RF windows. Multipactor analysis is carried out to determine multipactor thresholds of the proposed RF windows. Section 6.4 summarizes this chapter.

6.2 Proposed Overmoded RF Windows

In this section, four designs of RF windows are presented for overmoded operation in X-band. The proposed RF windows are designed mainly for the coaxial magnetron discussed in this thesis, operating at 9.3 GHz and having output from WR112 waveguide section. The proposed RF windows are based on the excitation of TE_{012} and TE_{022} modes. TE_{012} mode in a cylindrical cavity can be excited from a dominant TE_{10} mode of a rectangular waveguide in three different ways. Based on mode excitation techniques, three designs of RF window are presented in this chapter. The fourth design is based on the TE_{022} mode excitation from rectangular waveguide. Cylindrical cavity of RF windows and WR112 walls are made of copper having bulk electrical conductivity as 5.8×10^7 Sm^{-1}.

6.2.1 RF Windows Based on the Excitation of TE_{012} Mode

Based on the TE_{012} mode excitation techniques in the cylindrical cavity from a rectangular waveguide, the proposed RF windows are categorized as follows:

6.2.2 RF Window Design with Top and Bottom Wall Excitation

In this RF window design, a cylindrical cavity is designed for TE_{012} mode operation and further optimized for mixed-mode operation. Initial dimensions of the cylindrical cavity *i.e.* radius (r) and

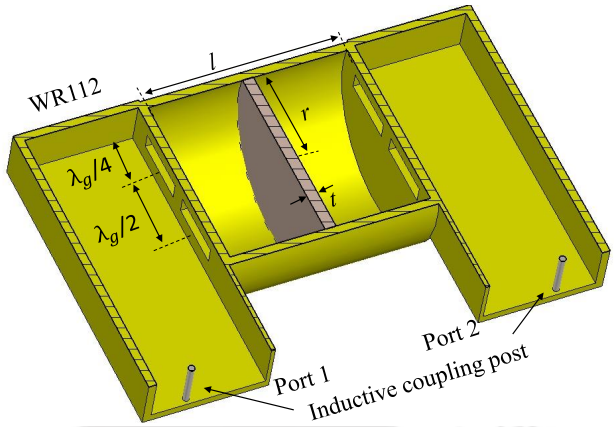

Figure 6.2: Cross-section of the RF window excited from the narrow-wall of WR112 waveguide to the end-wall of the cylindrical cavity (geometrical structure is adopted from [3]).

length (l) are calculated from (6.1). In this expression, $l = 2r$ is considered for calculating r of the cavity at resonant frequency ($f_{TE_{012}}$) of 9.3 GHz.

$$f_{TE_{012}} = \frac{1}{2\pi\sqrt{\mu_0\epsilon_0}}\sqrt{\left(\frac{2\pi}{l}\right)^2 + \left(\frac{3.832}{r}\right)^2} \tag{6.1}$$

where ϵ_0, and μ_0 represent permittivity, and permeability of free space, respectively.

In this RF window design, TE_{012} mode is excited in the cylindrical cavity from the narrow-wall of the WR112 waveguide to end-walls of the cavity through slots, as shown in Fig. 6.2. Two rectangular slots are made for the coupling from WR112 waveguide section to cavity. One rectangular slot is made at $\lambda_g/4$ distance from the end-wall of the WR112 waveguide section. The second rectangular slot is made at $\lambda_g/2$ distance apart from the center of first rectangular slot to excite TE_{012} mode in the cylindrical cavity [3]. Here, λ_g represents the guide wavelength of the dominant TE_{10} mode in WR112 waveguide section. A dielectric disk of alumina 96% with thickness t is placed at the middle of the cavity as a barrier in the RF window. The value of dielectric constant of alumina 96% is taken as 9.4 in this study. Inductive coupling posts are used at both input and output waveguide sections for impedance matching, as shown in Fig. 6.2.

6.2.3 RF Window Design with Sidewall Excitation

The excitation of desired TE_{012} mode is possible from WR112 waveguide section to sidewall of the cylindrical cavity in two different ways. In one way, the desired mode is excited from the narrow-wall of WR112 waveguide section to sidewall of the cylindrical cavity and in the second method, desired mode is excited from the end-wall of WR112 waveguide section to sidewall of the cylindrical cavity. In the first method, coupling slot is made at $\lambda_g/4$ distance from the end-wall of the rectangular waveguide, as shown in Fig. 6.3 (a). The initial dimensions of cylindrical cavity are calculated from (6.1). In the second method, the coupling slot is made at the end-wall of the WR112 waveguide section, as shown in Fig. 6.3 (b). In this RF window design (Fig. 6.3 (b)), TE_{014} mode is considered instead of TE_{012} mode to symmetrically accommodate two WR112 waveguide sections as input and output of RF window, however, the field pattern in the cross-section is same (TE_{01}). In both RF windows, alumina 99.5% is considered as the material of dielectric disk. The dielectric disk is placed at the center of the cylindrical cavity. The dielectric constant of alumina 99.5% is taken as 9.9 and disk thickness is represented by t.

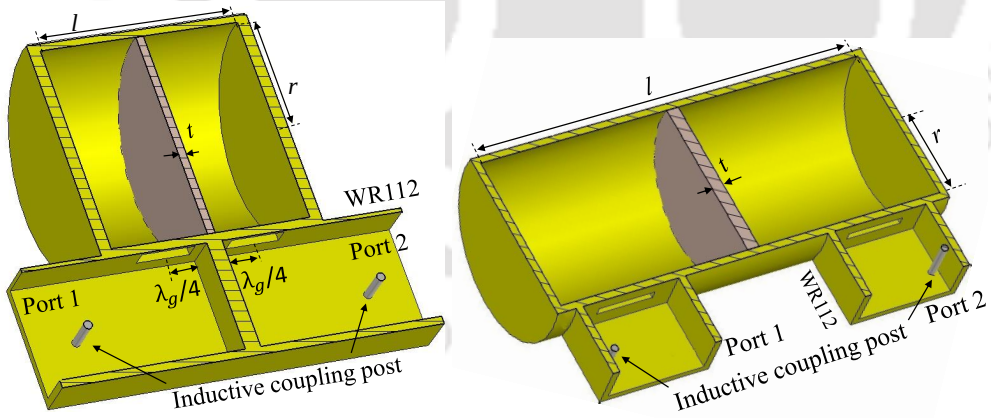

Figure 6.3: Cross-section of the RF windows with sidewall excitation. (a) Excited from the narrow-wall of the WR112 waveguide section to the sidewall of the cavity. (b) Excited from the end-wall of the WR112 waveguide section to the sidewall of the cavity

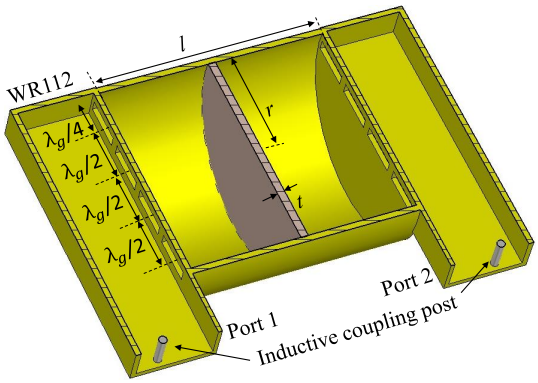

Figure 6.4: A cross-sectional view of RF window based on TE_{022} mode excitation.

6.2.4 RF Window Based on Excitation of TE_{022} Mode

In this approach, RF window is mainly operated in TE_{022} mode. The cylindrical cavity is designed to operate in TE_{022} mode at 9.3 GHz resonant frequency. The design parameters of cylindrical cavity *i.e.* radius and length are represented by r and l, respectively, as shown in Fig. 6.4. The initial dimensions are calculated from the expression given in (6.2). Here, for the determination of radius (r), cavity length (l) is considered as twice that of the radius of cavity (r) in this expression (6.2). The resonant frequency ($f_{TE_{022}}$) is considered as 9.3 GHz. The input and output sections of RF window are designed from WR112 waveguide sections.

$$f_{TE_{022}} = \frac{1}{2\pi\sqrt{\mu_0\epsilon_0}}\sqrt{\left(\frac{2\pi}{l}\right)^2 + \left(\frac{7.016}{r}\right)^2} \tag{6.2}$$

The desired TE_{022} mode is excited in the cylindrical cavity through four rectangular slots. These slots are made on the narrow wall of the rectangular waveguide. WR112 rectangular waveguide operates in the dominant TE_{10} mode. The first coupling slot is $\lambda_g/4$ distance apart from the short-circuited end-wall of the waveguide. Remaining slots are $\lambda_g/2$ distance apart from consecutive slots, as shown in Fig. 6.5. The dashed and continuous lines represent the reflected and incident waves, respectively, as depicted in Fig. 6.5. The positions of four coupling slots are chosen in such a way that the electric field directions inside the adjacent slots become opposite. Such type of electric field directions are required to excite a higher-order TE_{022} mode in the cylindrical cavity. The electric field patterns at the four rectangular slots are shown in Fig. 6.6. Every neighboring slot has opposite

Table 6.1: Design Parameters of the Proposed RF Windows

Parameters	*design 1*	*design 2*	*design 3*	*design 4*
Disk material	Alumina 96%	Alumina 99.5%	Alumina 99.5%	Alumina 99.5%
Dielectric constant	9.4	9.9	9.9	9.9
Loss tangent	0.0002	0.0001	0.0001	0.0001
Disk thickness (t)	2.806 mm	2 mm	3.492 mm	2.79 mm
Disk radius (r)	23.36 mm	27.17 mm	23.47 mm	38.91 mm
Cavity length (l)	50.44 mm	52.26 mm	115.4 mm	85.64 mm

electric field direction. Such field excites the desired circulating TE_{022} mode in the cylindrical cavity. For 2 MW peak power operation, the maximum electric field strength along the slot is determined as 5 MV/m.

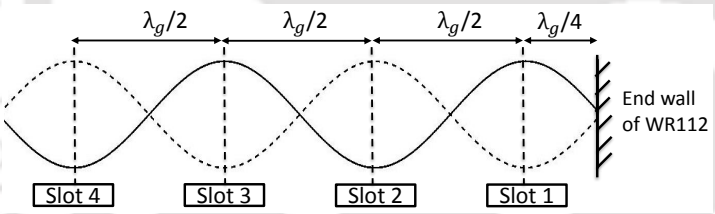

Figure 6.5: Standing wave pattern in the short-circuited WR112 waveguide section, and the corresponding positions of the coupling slots present in waveguide.

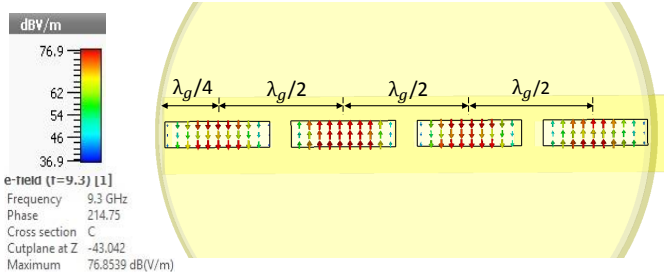

Figure 6.6: E-field direction in the rectangular coupling slots, made in the narrow wall of WR112 to excite TE_{022} mode in the cylindrical cavity.

The dielectric disk of alumina 99.5% with thickness t is placed at the center of cylindrical cavity, as shown in Fig. 6.4. The dielectric properties *i.e.* dielectric constant and loss tangent are considered

as 9.9, and 0.0001, respectively. Initial dimensions obtained analytically are further optimized for a broader bandwidth operation. In order to make the bandwidth of the RF window broader, mixed mode operation is considered instead of a single-mode operation. In this proposed RF window, TE_{022} mode is mixed with the adjacent modes *i.e.* TE_{122} mode and TE_{222} mode. For the efficient impedance matching, inductive posts are introduced at both input and output section of WR112 waveguide, as shown in Fig. 6.4.

RF windows presented in Fig. 6.2, Fig. 6.3 (a), Fig. 6.3 (b), and Fig. 6.4 are named as *design 1*, *design 2*, *design 3*, and *design 4*, respectively in this chapter. Design parameters of the proposed RF windows are presented in Table 6.1.

6.3 Simulation Results and Discussions

In this section, simulation results of the proposed RF windows are presented. The RF window designs are optimized based on the Nelder Mead Simplex Algorithm (NMSA) in CST studio. Multiphysics analyses are performed using coupled simulations using frequency-domain solver, thermal solver, and mechanical solver. Electromagnetic (EM) losses obtained from frequency-domain analysis are imported to thermal simulation, and further thermal losses are imported to structural analysis. Mechanical stress obtained from structural analysis is imported back to frequency-domain solver to perform sensitivity analysis of S-parameters. Flow diagram of the coupled analysis is shown in Fig. 6.7.

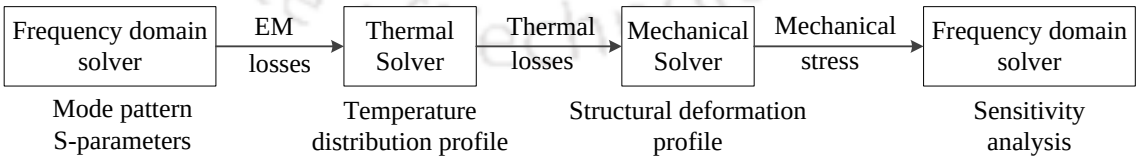

Figure 6.7: Flow diagram of the coupled simulation of RF windows.

6.3.1 Frequency-domain Analysis

Frequency-domain analysis is performed to determine return loss, insertion loss, VSWR, and operating modes of the RF windows at the desired frequency of 9.3 GHz. The operating modes are determined by analyzing electric field patterns at the given frequency. E-field patterns at the cross-

section of RF windows are shown in Fig. 6.8. These field patterns are plotted for phase variations (*i.e.* $\phi = 0°$, $120°$, and $270°$) at the same cross-section of the cavity. In Fig. 6.8 (a), Operating mode of *design 1* is shown. Here, TE_{012} mode is mixed with TE_{113} mode and TE_{213} mode. Mixed-mode operation makes the RF window broadband than the single-mode operation. The operating modes of *design 2* are shown in Fig. 6.8 (b). In *design 2* TE_{012} mode is mixed with TE_{312} mode. Middle pattern in Fig. 6.8 (b) shows the transition of TE_{312} mode from TE_{012}. *design 3* operates in the single mode, *i.e* TE_{014} type mode. Fig. 6.8 (d) presents the operating modes of *design 4*. In this design, TE_{022} mode is mixed with TE_{122} and TE_{222} modes.

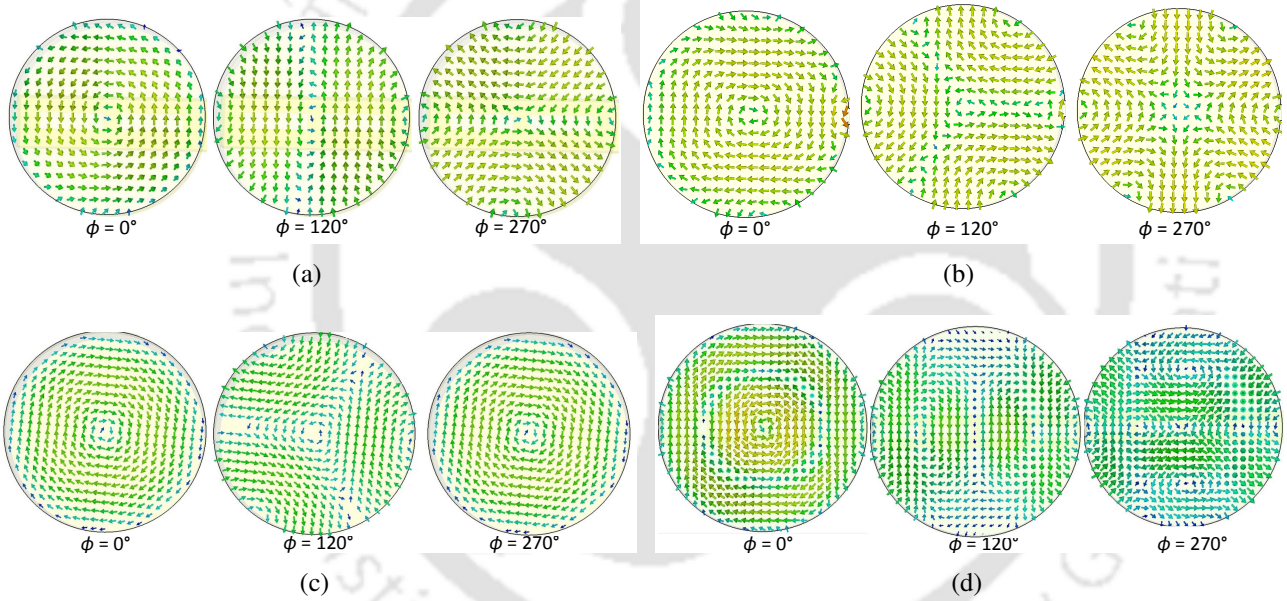

Figure 6.8: Phase variations of E-field patterns in the cross-section of cylindrical cavity. (a) *design 1*. (b) *design 2*. (c) *design 3*. (d) *design 4*.

S-parameters of the proposed RF windows are shown in Fig. 6.9. Return losses and insertion losses of the RF windows obtained from CST simulations are verified with the simulation results in HFSS. Results obtained from HFSS are in good agreement with the results obtained from the CST. Performance parameters *i.e.* return loss, insertion loss, VSWR, and bandwidth (for VSWR ≤ 1.05) obtained from CST simulations are presented in Table 6.2.

The sensitivity of S-parameters to dielectric properties of window disks are studied. For this, the studies on the effects of dielectric constant and loss tangent ($\tan\delta$) variations of alumina 99.5% on

Table 6.2: Frequency-domain analysis of RF windows (at 9.3 GHz)

Parameters	*design 1*	*design 2*	*design 3*	*design 4*
Return loss	55.04 dB	51.52 dB	53.92 dB	52.76 dB
Insertion loss	0.054 dB	0.07 dB	0.194 dB	0.06 dB
VSWR	1.0035	1.005	1.004	1.004
Bandwidth (VSWR $\leq$ 1.05)	79.6 MHz	40.8 MHz	4.1 MHz	41.4 MHz

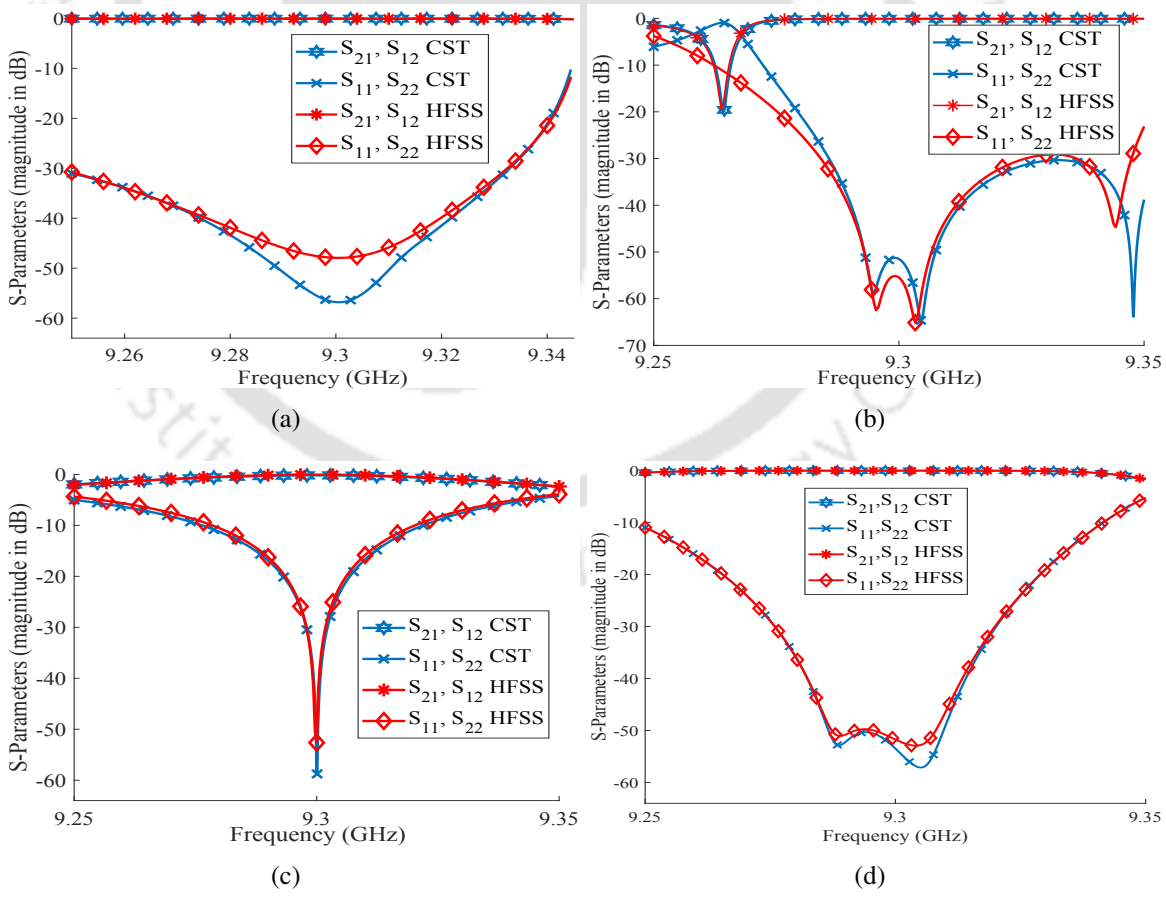

Figure 6.9: *S*-parameters of the proposed RF windows. (a) *design 1*. (b) *design 2*. (c) *design 3*. (d) *design 4*.

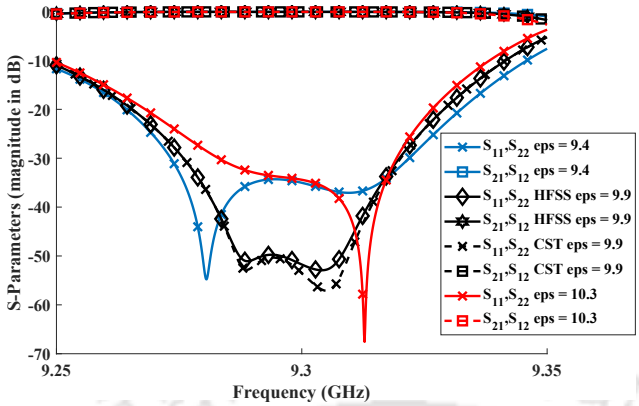

Figure 6.10: Effect of dielectric constant variation on S-parameters of *design 4*.

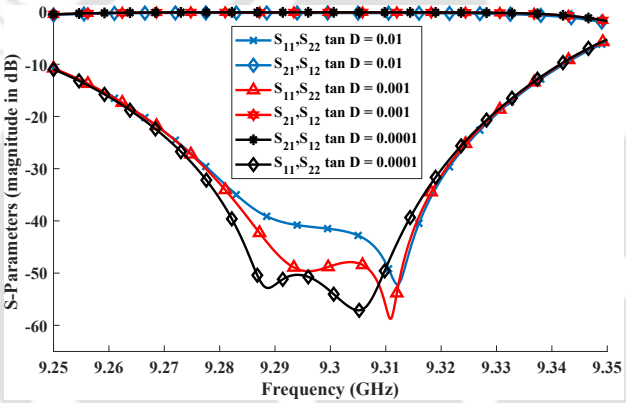

Figure 6.11: Effect of loss tangent ($\tan\delta$) variation on S-parameters of *design 4*.

the S-parameters of *design 4* are presented. The sensitivity of S-parameters of rest of the proposed RF windows have also been studied and the results follow the same trend. In *design 4*, the dielectric constant of alumina 99.5% is varied from 9.4 to 10.3 and the S-parameters for dielectric constant 9.4 and 10.3 are compared with the S-parameters of *design 4* for dielectric constant 9.9, as shown in Fig. 6.10. The optimum performance is obtained at the dielectric constant of 9.9. S-parameters of the RF window obtained in CST are compared with the results of HFSS, and are in good agreement, as shown in Fig. 6.10.

Similarly, the effects of loss tangent variation of alumina 99.5% on the S-parameters of *design 4* are also studied. S-parameters for loss tangent's values of 0.0001, 0.001, 0.01 are determined, as shown in Fig. 6.11. The return loss variation is within the tolerable limits for the desired application

at 9.3 GHz, even when loss tangent is varied 10 times, from 0.0001 to 0.001.

6.3.2 Thermal Analysis

Coupled simulations are performed to obtain thermal distribution profiles of RF windows. EM analysis is coupled to thermal simulations. RF windows are studied for various average input power levels. A scaling factor is needed to set the desired average input power levels while applying the EM field as a source in the thermal analysis. Windows are considered in normal cooling environment in this analysis. RF windows are assumed to be placed in the air surrounding. Free air convection is considered at the outer surface of the RF window for thermal analysis with heat transfer coefficient of 15 $Wm^{-2}K^{-1}$. Thermal properties of the materials used in RF windows *i.e.* copper and alumina are considered as per the material library of CST, as presented in Table 6.3. In practice, the ceramic disk is brazed with the copper cylinder. In the thermal analysis, thermal contact between ceramic disk and metal is modeled by specifying a 20 micron thickness of the brazing material, which is basically a silver copper eutectic. Although, thermal conductivities of silver and copper are 429 $WK^{-1}m^{-1}$ and 401 $WK^{-1}m^{-1}$, respectively, thermal conductivity of the thermal contact is considered to be 200 $WK^{-1}m^{-1}$, to have safety factor. Thermal distribution profiles of the proposed RF windows for 4 kW average input power are shown in Fig. 6.12. The maximum temperature at steady state appears at the center of the dielectric disk because of the cooling from the outer surrounding. Multimode operation of RF windows helps to prevent localized heating and spreads the heating to larger surface area at the disk. The maximum temperature for 4 kW average input power at the disk is obtained as 32.7° C, 48.7° C, 36.1° C, and 26° C for *design 1*, *design 2*, *design 3*, and *design 4*, respectively as depicted in Fig. 6.12.

Table 6.3: Thermal properties of the materials used in RF Windows

Properties	Copper	Alumina 96%	Alumina 99.5%
Thermal conductivity ($WK^{-1}m^{-1}$)	401	25	30
Heat capacity ($kJK^{-1}kg^{-1}$)	0.39	0.88	0.88
Thermal expansion ($\times 10^{-6}K^{-1}$)	17	7	7.9

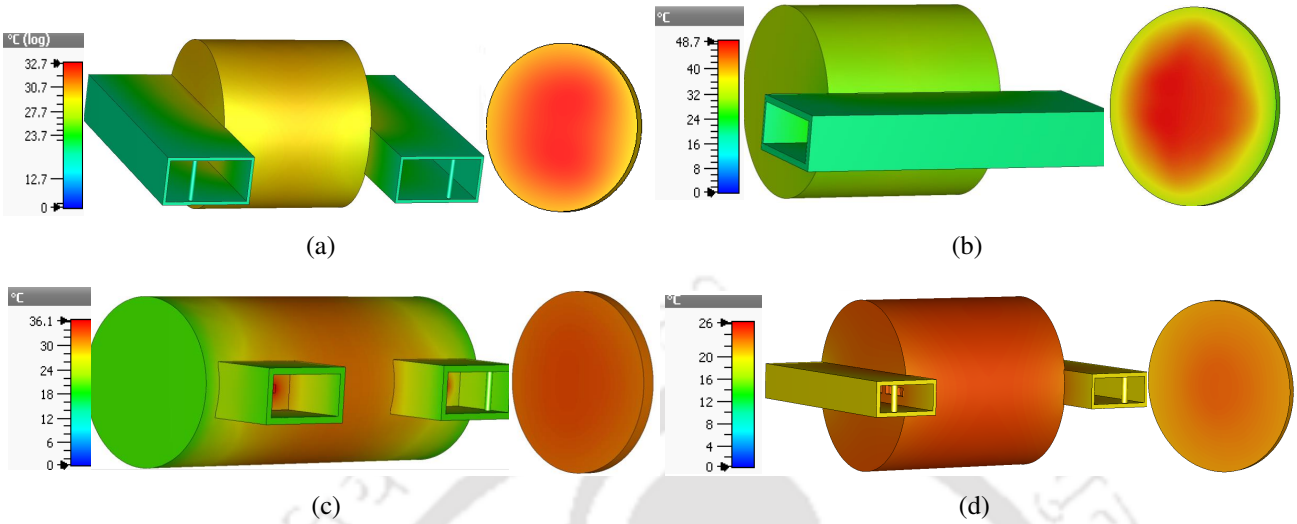

Figure 6.12: Thermal distribution profiles of the proposed RF windows. (a) *design 1*. (b) *design 2*. (c) *design 3*. (d) *design 4*.

The temperature distribution of RF windows are determined for various average input powers such as 2 kW, 4 kW, 10 kW, 20 kW, and 50 kW. Variations of the maximum steady state temperatures with average input powers are plotted in Fig. 6.13 for all four RF windows. It is observed that the maximum temperature attained at the steady state varies linearly with the average input power.

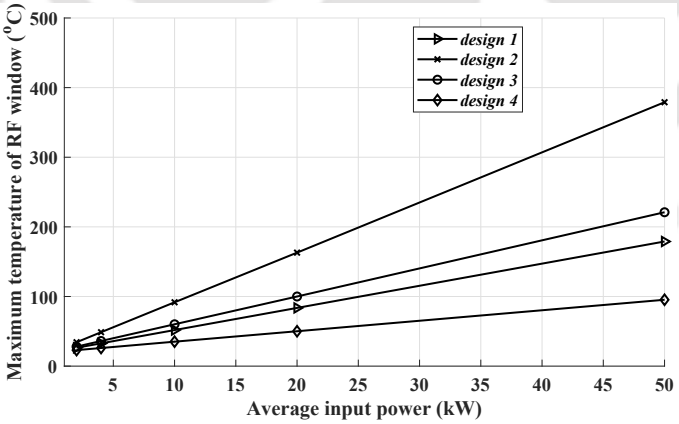

Figure 6.13: Variations of the maximum temperatures attained at the steady state of the proposed RF windows with average input powers.

6.3.3 Structural Analysis

The coupled structural analysis is performed to study deformation appeared in the RF window structures. Thermal losses are imported to mechanical solver. In this analysis deformations appeared

in the structures due to the pressure difference and temperature distribution are studied. On one side of the dielectric disk, ultra-high vacuum is considered, and on the other side pressurized gas environment with 30 psi pressure is considered. In this analysis, input and output ports of the windows are kept fixed. The thickness of the copper cylinder where it will be brazed with the alumina disk and its vicinity is made purposefully thin, as shown in Fig. 6.14 to reduce the thermal stress appeared due to the dissimilar thermal expansion of copper and ceramic during brazing at around 800°. To avoid stress and rupture due to the dissimilar thermal expansion during the brazing process, molybdenum wire is wrapped around and tighten at the thin section of the copper cylinder. As the molybdenum has less thermal expansion coefficient than copper, which prevent expansion of copper material. During the cooling process copper contracts and eventually, the joint is under compression at room temperature, which is desirable to ceramic to metal joint.

The maximum deformation of 0.02 mm is obtained at the middle of the disk in *design 1*, as shown in Fig. 6.14 for 4 kW average input power. This type of analysis is also carried out for *design 2*, *design 3*, and *design 4* and the maximum deformation is obtained at the center of the disk as 0.043 mm, 0.018 mm, and 0.051 mm, respectively. Mechanical properties of the copper and dielectric are considered from the CST library, Table 6.4.

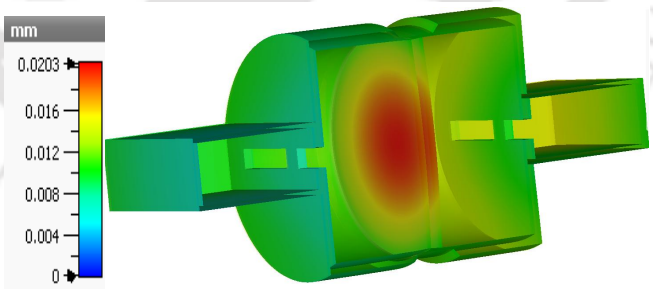

Figure 6.14: Displacement profile of the *design 1* RF window. A cut in the outer material near the alumina disk is introduced for considering fabrication point of view.

The Effects of the deformation on the S-parameters are also analyzed to check the sensitivity of the RF window. Since the mechanical deformation is very less so change in the S-parameters is negligible,as shown in Fig. 6.15 for *design 1*. The same trend follows for *design 2*, *design 3*, and *design 4*, negligible deformation due to the pressure difference and thermal stress doesn't affect the performance of the proposed RF windows.

Table 6.4: Mechanical properties of the materials used in RF Window

Properties	Copper	Alumina 99.5%
Young's modulus (GPa)	120	370
Poisson's ratio	0.33	0.22
Material density (Kg m^3)	8930	3900

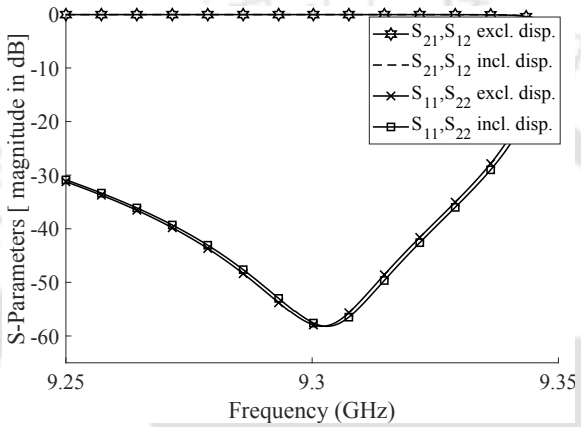

Figure 6.15: Effect of mechanical deformation on S-parameters of the *design 1*.

6.3.4 Multipactor Analysis

In this section, multipactor analysis is performed to determine multipactor threshold of the proposed RF windows. SPARK3D simulator is used for this analysis. For Secondary Electron Yield (SEY) characterization of materials, Vaughan model is used in SPARK3D [73, 74]. RF window walls are made of copper (ECSS) from the material library of the SPARK3D is used for this analysis. Multipactor analysis is very sensitive to the SEY properties of the material. SEY properties considered in the multipactor analysis is shown in Table 6.5. Multipactor analysis results are shown in Fig. 6.16. Growth of electrons is plotted with time. Multipactor analysis is carried out for various input power levels for determining multipactor threshold. Exponential growth of electrons are observed when multipaction occurs. But for lower power levels the number of electrons vanish. Multipactor thresholds of *design 1*, *design 2*, *design 3*, and *design 4* are obtained as 10 MW, 16 MW, 2.35 MW, and 20.75 MW, respectively, as shown in Fig. 6.16.

RF windows can be operated without multipaction below these multipactor thresholds of the re-

Table 6.5: SEY Parameters Considered in Multipactor analysis of RF Window

Parameters	Values
Maximum secondary emission coefficient	2.3
Secondary emission coefficient below lower crossover	0.5
Lower crossover electron energy (eV)	35
Electron energy at maximum SEY (eV)	165

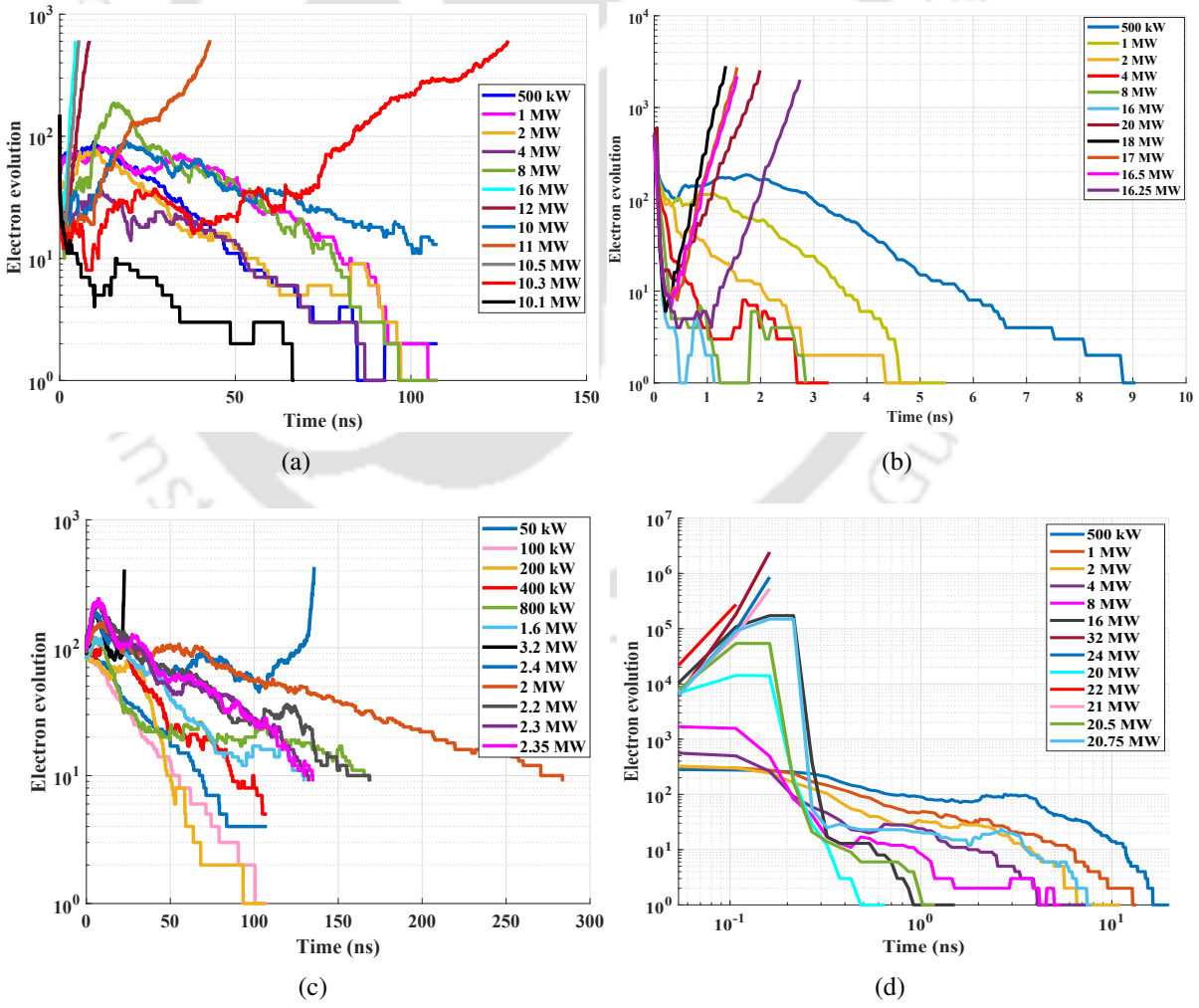

Figure 6.16: Multipactor analysis of RF windows. (a) *design 1*. (b) *design 2*. (c) *design 3*. (d) *design 4*

spective RF windows. The type of multipactor is double surface, as it occurs in the vicinity of the coupling slots. Coupling slots are the region of multipactor discharge when input power exceeds from the multipactor breakdown threshold. RF window structure has input and output rectangular waveguides which are coupled to cylindrical waveguide through coupling slots. This region is the potential vulnerable area in the RF window. Since the proposed RF windows are mainly designed for a coaxial magnetron with 2 MW peak and 2 kW average powers at 9.3 GHz operating frequency, multipactor thresholds are higher than the desired operating conditions of RF windows. RF windows can be safely operated. Sometimes, antimultipactor coating *i.e.* TiN is used on the dielectric surface to increase the multipactor thresholds levels.

CAD designs of the proposed RF windows are presented in the Appendix E for the feasibility of the fabrication. Impact of tolerance of radius and position of the inductive coupling post is also discussed in Appendix E.

6.4 Summary

In this chapter, four ingenious designs of overmoded high-power RF windows are presented for X-band applications. Proposed RF windows are mainly designed for a coaxial magnetron having 2 MW peak and 2 kW average powers at 9.3 GHz with WR112 output section but can also be used in other VEDs *e.g.* klystron, gyrotron, and LINAC. Multiphysics analyses of RF windows are performed for EM, thermal, and structural behavior of the RF windows. In these analyses, EM, thermal, and structural simulations are coupled together to analyze the temperature distribution profiles and mechanical deformation appeared in the structures caused by the thermal and mechanical stresses. Operating modes of *design 1* and *design 2* are primarily TE_{012} type. This mode is mixed with TE_{113} and TE_{213} for the *design 1*, and TE_{312} for the *design 2*. *design 3* operates in TE_{014} mode. *design 4* operates in TE_{022} mode, mixed with TE_{122} and TE_{222} modes. Mixed mode operation allows an RF window to operate with broader bandwidth than single mode operation. *design 1* has 79.6 MHz bandwidth which is much larger than the other three designs. *design 3* is almost single mode and has the narrowest bandwidth. Return losses of the design 1, design 2, design 3, and design 4 are obtained as 55.04 dB, 51.52 dB, 53.92 dB, and 52.76 dB, respectively. Return losses obtained in CST are verified

in HFSS, and are in good agreement. Variation of the maximum temperature with input power is analyzed and it is observed that relation is linear. Sensitivity analysis is also performed to analyze the effect of the mechanical deformation produced by the thermal stress and pressure difference on the performance of the RF windows. Negligible displacement doesn't affect the S-parameters considerably. Multipactor study is carried out in SPARK3D, and multipactor threshold is determined for the proposed RF windows.

Although all the four presented designs perform quite well, from the performance analysis presented in this chapter it can be seen that *design 1* is marginally better in terms of bandwidth. However, from the compactness point of view *design 2* is slightly better as compared to others. The *design 3* is presented here to show an alternate way of exciting higher order mode in the cavity. In fact, this window operates with a single mode only which limits its bandwidth performance as compared to multiband designs as presented in *design 1*, *design 2*, and *design 4*. This also shows the importance of operating the cavity in multimode when a broadband operation is desired. *design 4* has the highest multipactor breakdown threshold as compared to other three designs.

7

A New Approach of High-Power Coaxial Magnetron using Stacked Anode Resonators

Contents

In this chapter, a new design approach for high-power coaxial magnetron is presented. In this approach, the coaxial magnetron is modified with multiple anode resonators. Anode resonators are placed in a stacked configuration in the proposed modified coaxial magnetron. The advantage of this approach is to enhance the output power of a coaxial magnetron without the requirement of additional circuitry for power combining. Power generated from stacked multiple resonators are combined within the coaxial magnetron itself. The modified coaxial magnetron design is proposed with two different cathode configurations: in one configuration, separate cathodes are considered, and in the other case, connected cathodes are considered. The proposed modified coaxial magnetron is analyzed using the PIC simulations. The performance of modified coaxial magnetron with both types of cathode configurations are compared.

7.1 Introduction

High-power microwave (HPM) source at high-frequency has various applications. However, HPM from the single magnetron becomes challenging at high-frequencies because of the geometrical constraints. For such applications, output powers from multiple magnetrons are combined in an array configuration [75]. However, a magnetron has phase inconsistency in the output and it is a noisy oscillator. The power combining in the magnetron array becomes cumbersome because of the random phase of its output [14, 76]. To overcome this phase inconsistency, phase-locking techniques are required in magnetron arrays for power combining [17, 50–55]. Phase-locking makes the magnetron sources coherent in magnetron arrays. However, these phase-locking methods require complex external circuitry, including hybrid couplers, solid-state devices, hence, increasing the cost of the system and making the whole system bulkier.

The output power enhancement in a coaxial magnetron using stacked anode resonators is not reported in any earlier literature to the best of the knowledge of the author. In the modified coaxial magnetron, the outer coaxial cavity is used to internally couple the power generated from the stacked anode resonators. This proposed power combining technique doesn't require complex external circuitry, as it combines power internally and also maintains the compactness of the structure.

The key contributions of this chapter are as follows:

- A novel design of the coaxial magnetron using the approach of stacked anode resonators is proposed for generation of high-power. The modified coaxial magnetron is proposed for operation in the X-band. A drastic improvement of 272.6% and 368% in the output peak powers are achieved in dual anode resonators and triple anode resonators, respectively, as compared to the conventional coaxial magnetron with single anode resonator.

- The modified coaxial magnetron is designed using two different configurations of the cathodes. In one arrangement, two separate cathodes are employed with two anode resonators. This design can have two types of cathode excitation: both cathodes are excited simultaneously, and only one of the cathode is excited at a time. Three different output power levels can be obtained based on the ways the cathodes are excited. In the second arrangement, both cathodes are connected. In the connected cathode arrangement, more than two anode resonators can be employed. In the present chapter, the proposed magnetron configuration has been tested up to three anode resonators.

- The output performances of the modified coaxial magnetrons with both types of cathode arrangements are compared using PIC simulations.

Section 7.2 presents the concept and design of the proposed modified coaxial magnetron with stacked anode resonators. The modified coaxial magnetron design is presented with both types of cathode arrangements. The simulation of the coaxial magnetron is presented in Section 7.3. The proposed designs are analyzed by eigenmode simulation, frequency-domain simulation, and particle-in-cell (PIC) simulation. Section 7.4 is about the comparison of the coaxial magnetron design with both types of cathode arrangements. Section 7.5 concludes this chapter.

7.2 Concept and Design of a Coaxial Magnetron with Stacked Anode Resonators

The idea of the proposed modified coaxial magnetron design is to couple the generated powers from multiple anode resonators placed in a stack configuration by coupling of the fields through the external coaxial cavity. In the conventional coaxial magnetron, an anode resonator is coupled to the

outer coaxial cavity operating in TE_{011} mode through longitudinal coupling slots in the alternate vane cavities, as discussed in chapter 3. However, in the proposed structure, two anode resonators, namely the upper anode resonator, and the lower anode resonator, are coupled through external TE_{012} mode coaxial cavity, as shown in Fig. 7.1, and in Fig. 7.2. The purpose of introducing outer coaxial cavity operating in the TE_{012} mode is to accommodate two stacked anode resonators and having the similar circulating electric field pattern as the TE_{011} mode of the conventional coaxial magnetron with single anode resonator. The circulating electric field in the outer coaxial cavity provides stability to the desired π-mode. In a conventional coaxial magnetron, the output is taken from the rectangular waveguide connected through a coupling slot in the middle of the outer wall of the coaxial cavity, where the electric field of TE_{011} mode is maximum along the length of the cavity, as discussed in chapter 3. However, in the modified coaxial magnetron, the electric field vanishes at the middle of the external coaxial cavity for TE_{012} mode, and the maximum values occur in the middle of the upper and lower halves of the coaxial cavity. The rectangular coupling slot for the output section in the external coaxial cavity wall is made at the location of the maximum electric field strength for the efficient coupling, as shown in Fig. 7.1, and Fig. 7.2. The phases of the electric fields in the two stacked vane cavities, in the upper and lower anode resonators are opposite because the corresponding direction of the electric field in the outer TE_{012} mode cavity is opposite along the length of the coaxial cavity.

Two designs are proposed for the modified coaxial magnetron with two anode resonators placed in a stack, based on the cathode configuration: *design 1* and *design 2*. The design with stacked anode resonators with two separate cathodes is named as *design 1*, and stacked anode resonators with two connected cathodes is named as *design 2* in this chapter.

7.2.1 *Design 1*: Stacked Anode Resonators with Two Separate Cathodes

In this design configuration, two separate cathodes are considered for the two anode resonators placed in a stack arrangement, as shown in Fig. 7.1. Here, anode resonators are represented as upper anode resonator and lower anode resonator. Each anode resonator has 28 vanes. Similar to the conventional coaxial magnetron structure, alternate vane cavities of both the anode resonators are coupled to the outer coaxial cavity through coupling slots. The outer coaxial cavity is designed to

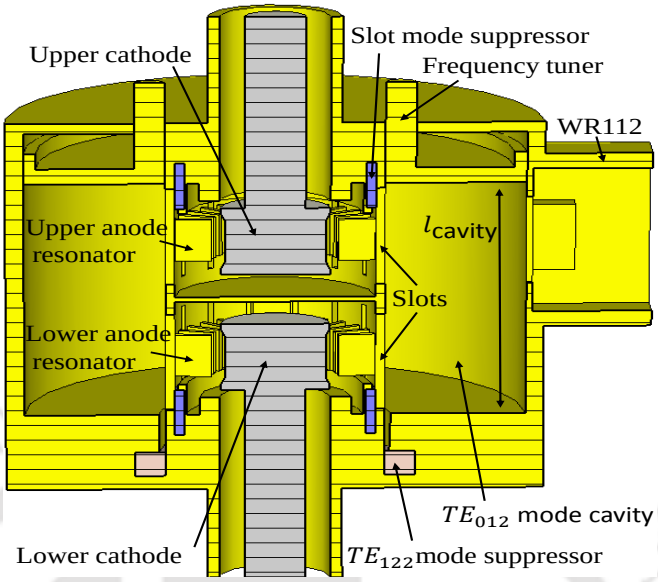

Figure 7.1: A cross-sectional view of the proposed modified coaxial magnetron with *design 1* configuration having two separate cathodes.

operate in TE_{012} mode. The length of the coaxial cavity is represented by l_{cavity}. The dimensions of various sub-parts of the modified coaxial magnetron *i.e.* cathode radius, anode radius, vane length, vane thickness, and vane height, are determined in accordance with the conventional coaxial magnetron, as discussed in chapter 3. It may be noted that conical shaped cathode end hats have been used in the proposed modified coaxial magnetron, as discussed in chapter 5. In the proposed design, two slot mode suppressors are employed in the vicinity of coupling slots, for the suppression of unwanted slot modes, as shown in Fig. 7.1. In this design, TE_{122} mode is the competing mode to the desired mode in the coaxial cavity instead of TE_{121} mode, which is one of the dominant interfering competing mode in the conventional coaxial magnetron, as discussed in chapter 2. Suppression of unwanted modes *i.e.* slot modes and TE_{122} mode is necessary for proper operation of the modified coaxial magnetron. Unwanted mode suppressors for TE_{122} mode and slot modes are designed as per the conventional coaxial magnetron, as discussed in previous chapters (chapter 2 and chapter 4).

The output of the modified coaxial magnetron is taken from the WR112 waveguide section through a rectangular coupling slot made in the outer wall of the coaxial cavity. The coupling slot is made in the middle of the upper half of the outer coaxial cavity, as shown in Fig. 7.1. The operating frequency can be tuned by changing l_{cavity} from the mechanical movement of the frequency tuner.

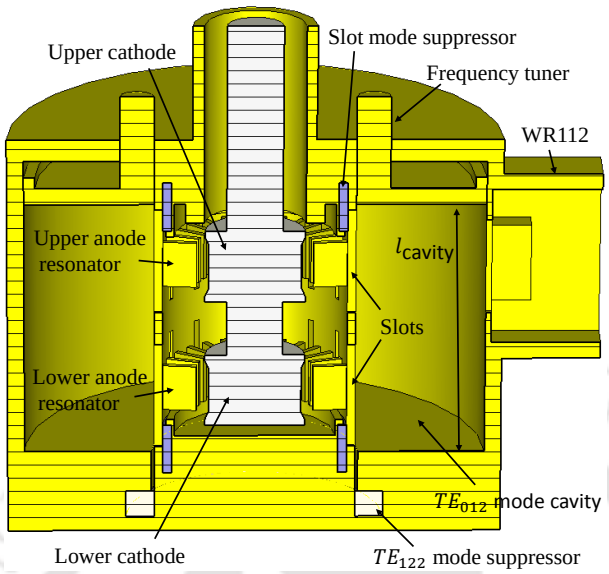

Figure 7.2: A cross-sectional view of the proposed modified coaxial magnetron with *design 2* configuration having two connected cathodes.

7.2.2 *Design 2*: Stacked Anode Resonators with Two Connected Cathodes

In this design approach of the modified coaxial magnetron, two connected cathodes are considered instead of two separate cathodes, as shown in Fig. 7.2. Both cathodes are connected to single cathode support. The rest of the structure is same as the structure of coaxial magnetron with *design 1* configuration. The connected cathodes configuration has an advantage over the separate cathodes configuration; it can also be used with more than two numbers of stacked anode resonators. A coaxial magnetron can be designed with three stacked anode resonators with three connected cathodes and outer coaxial cavity operating in TE_{013} mode, as shown in Fig. 7.3. This arrangement can be further extended to more number of stacked anode resonators. For n number of anode resonators, outer coaxial cavity can be designed for TE_{01n} mode operation.

7.3 Simulation Results and Discussion

Simulation results of the modified coaxial magnetron with *design 1* and *design 2* configuration are presented in this section. The modified coaxial magnetron is analyzed using eigenmode, frequency-domain, and PIC simulations in CST Studio.

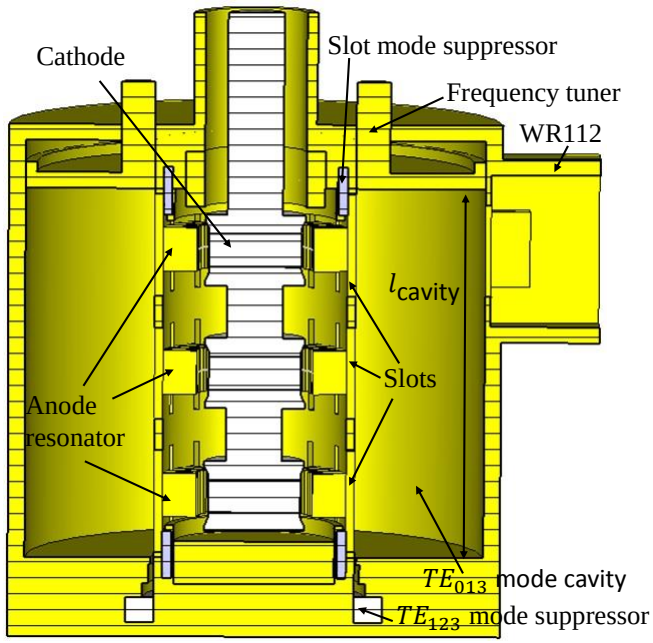

Figure 7.3: A cross-sectional view of the extended structure of *design 2* configuration having three anode resonators.

7.3.1 Analysis of *design 1*

Operating mode, return loss, and cold test parameters are determined using eigenmode and frequency-domain analyses. Output performance parameters *i.e.* output power, anode current, efficiency, and operating frequency are determined using particle-in-cell (PIC) analysis.

7.3.1.1 Eigenmode and Frequency-domain Simulation

The operating mode of a magnetron can be determined by observing the electric field pattern at the desired frequency. The electric field vector plots of the cross-sections of both upper and lower anode resonators of *design 1* are shown in Fig. 7.4. The anode resonators of the modified coaxial magnetron operate in the π-mode, and the external coaxial cavity operates in the circulating TE_{012} mode at 9.31 GHz, as shown in Fig. 7.4. The electric field patterns of upper and lower anode resonators are shown in Fig. 7.4 (a), and Fig. 7.4 (b), respectively. It is observed that the directions of electric field in the corresponding stacked vane cavities of the upper and lower anode resonators are opposite. Similarly, electric field directions in the upper and lower halves of the external coaxial cavity are also opposite, as shown in Fig. 7.4, because external coaxial cavity operates in the TE_{012} mode. The circulating field

of the outer coaxial cavity changes the directions of fields in the upper and lower anode resonators. Output of the modified coaxial magnetron is taken from the WR112 waveguide section, which is operating in dominant TE_{10} mode, as shown in Fig. 7.4 (a).

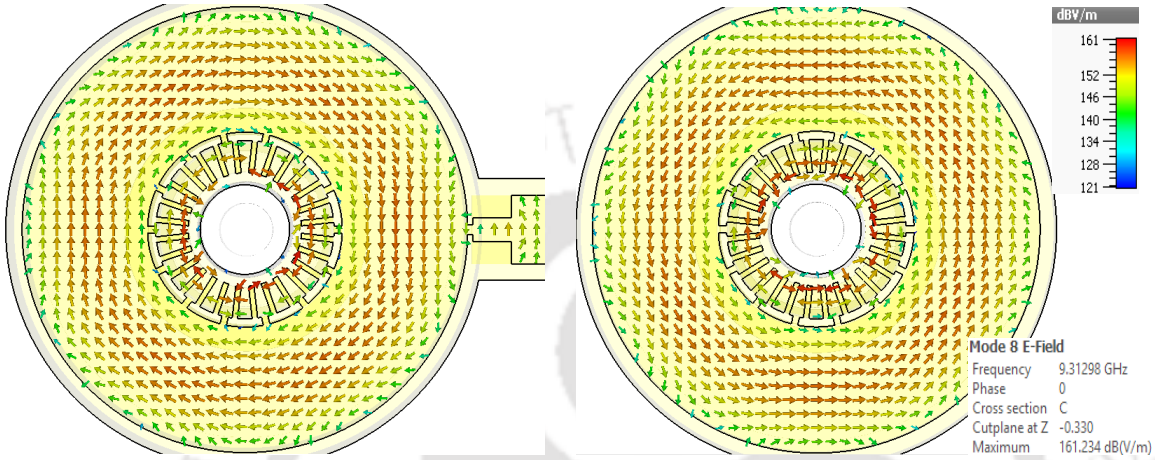

(a) (b)

Figure 7.4: The electric field vector plots of the operating mode at 9.31 GHz. (a) At a cross-section of upper anode resonator. (b) At a cross-section of lower anode resonator.

The return loss determined from the frequency-domain analysis of *design 1* is shown in Fig. 7.5. Here, return losses of the desired π-mode and nearby competing mode are shown in Fig. 7.5. For π-mode, 3.54 dB return loss is obtained at the 9.3 GHz. The competing mode *i.e.* TE_{122} mode is at 9.41 GHz having 15.1 dB return loss. The cold test parameters *i.e.* coupling coefficient (β), unloaded quality factor (Q_0), loaded quality factor (Q_l), external quality factor (Q_{ext}), and circuit efficiency (η_C) of the modified coaxial magnetron are calculated from the S-parameter. The values of β, Q_0, Q_l, Q_{ext}, and η_C are determined as 4.97, 8173, 1368, 1643, and 83%, respectively, based on the method discussed in chapter 3. The coupling coefficient ($\beta > 1$) ensures the overcoupling operation, which is desired for the proper magnetron operation.

7.3.1.2 Particle-in-Cell (PIC) Simulation

PIC analysis is carried out to determine output performance of the proposed modified coaxial magnetron. In this study, explosive emission model is considered for particles' emission. As discussed earlier, *design 1* with separated cathodes configuration can be operated in two different ways: first,

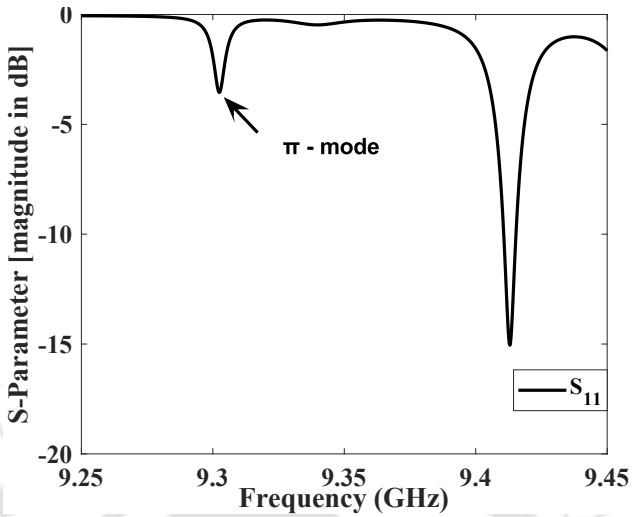

Figure 7.5: S_{11} parameter of the proposed coaxial magnetron with *design 1* configuration.

when both the cathodes are excited simultaneously, and second, when either lower or upper cathode is excited at a time. In the first type of excitation, 45 kV DC anode voltage is applied at both upper and lower cathodes by using two discrete ports. The operating point of the magnetron is determined from the Hull-Hartree diagram, and the value of magnetic field is further optimized for the maximum efficiency of the magnetron, as discussed in chapter 5. The optimal value of magnetic field is obtained as 5795 Gauss. This operating point is same as considered in the conventional coaxial magnetron with single anode resonator, as discussed in chapter 5. A waveguide-port is defined for collecting the generated RF at the opening of WR112 waveguide section. A waveguide-port is a matched termination and it absorbs the incident RF power without reflection. In the modified coaxial magnetron, it is desired that all the anode resonators operate in the π-mode at the same operating frequency. The π-mode operation is determined by the number of electrons spokes formation. Since upper and lower anode resonators have 28 vanes, for the π-mode operation, 14 electrons spokes are formed in both upper and lower anode resonators in the steady-state operation, as shown in Fig. 7.6. These electrons spokes of both anode resonators are not aligned because electrons spokes are formed according to the direction of the electric field in the vane cavities. Since upper and lower anode resonators have a 180° phase shift in the electric field direction, therefore, a shift in electrons spokes is also observed in both upper and lower stacked anode resonators, as shown in Fig. 7.6. The side-view and top-view of the electrons bunching are shown in Fig. 7.6 (a) and (b), respectively.

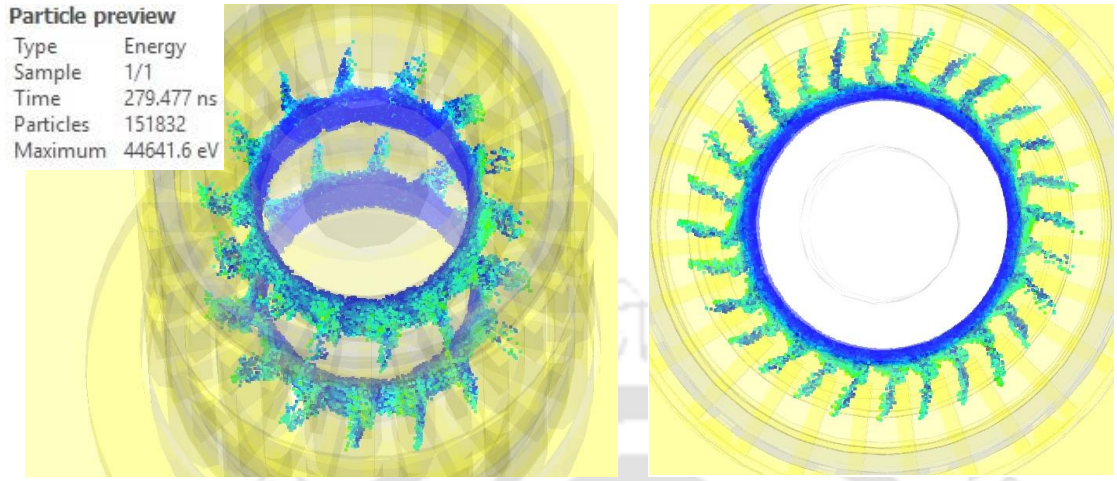

(a) (b)

Figure 7.6: The formation of 14 electrons spokes in the desired π-mode operation in the upper and lower anode resonators. (a) Side-view. (b) Top-view.

In this study, PIC simulation is carried out for a duration of 400 ns with 5 ns rise time. 5.78 MW output power with 49.4% total efficiency (η_T) at the operating frequency of 9.2906 GHz is obtained for the steady-state operation. The anode currents obtained at the upper and lower anode resonators are represented as I_{upper} and I_{lower}, respectively. Output power, I_{upper}, and I_{lower} are shown in Fig. 7.7; both currents have the same values as 130 Amp. The total anode current is determined as 260 Amp from the summation of the I_{upper} and I_{lower}. The operating frequency of the modified coaxial magnetron can be determined from the power spectral density (PSD) of the output signal, as shown in Fig. 7.8. Here, the desired π-mode and the other competing modes are shown. Other competing modes are well below 55 dB as compared to the π-mode, which shows the efficient suppression of unwanted modes. The second harmonic of the π-mode is at 18.58 GHz, which is twice the π-mode operating frequency (9.29 GHz), and is below 55 dB as compared to the π-mode. The electronic efficiency (= η_T/η_C) of the modified coaxial magnetron is calculated as 59.5%.

It is observed that the output power of the modified coaxial magnetron with double anode resonators is increased drastically by about 2.73 times as compared to the conventional coaxial magnetron (2.12 MW) with single anode resonator, as shown in chapter 5.

Similar to the conventional coaxial magnetron, discussed in the chapter 5, operating frequency of

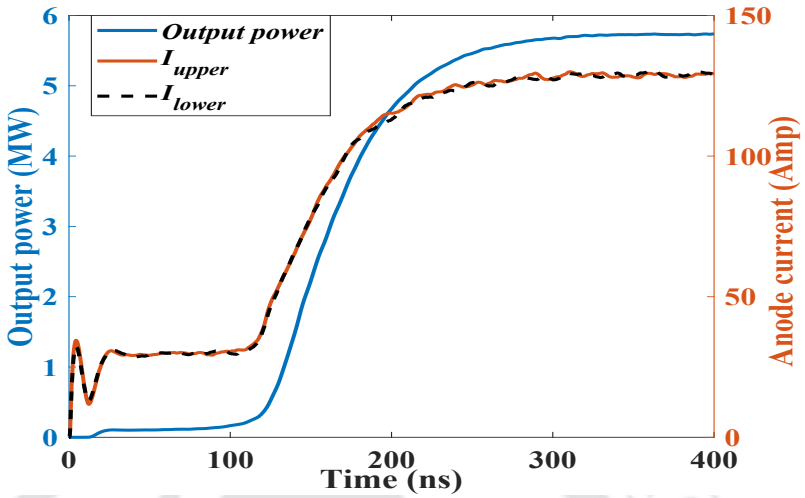

Figure 7.7: The output power and anode current of the *design 1* when both the cathodes are excited simultaneously.

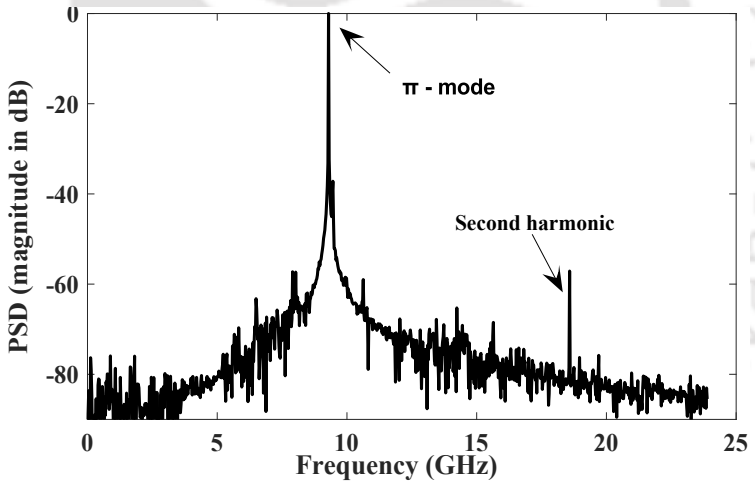

Figure 7.8: The power spectral density (PSD) plot of the output signal of *design 1*.

the modified magnetron can also be varied by changing the length of the outer coaxial cavity. The frequency tuning characteristics of the modified coaxial magnetron are studied by changing l_{cavity} through the positioning of frequency tuner and presented in Table 7.1. The frequency of the coaxial cavity is inversely related to the length of the cavity (l_{cavity}) as discussed in chapter 3. For the same output power levels, the proposed magnetron can be tuned from 9.284 GHz to 9.3145 GHz. Hence, the frequency tuning range of 30.5 MHz is obtained for the modified coaxial magnetron configuration for the *design 1*.

Table 7.1: Frequency Tuning Characteristics of the *design 1* Coaxial Magnetron

l_{cavity}	Frequency	Output power	η_T
46.40 mm	9.2667 GHz	5.61 MW	46.12%
46.30 mm	9.2840 GHz	5.78 MW	48.40%
46.20 mm	9.2906 GHz	5.78 MW	49.40%
46.05 mm	9.3145 GHz	5.78 MW	47.57%
45.95 mm	9.3280 GHz	5.12 MW	33.00%

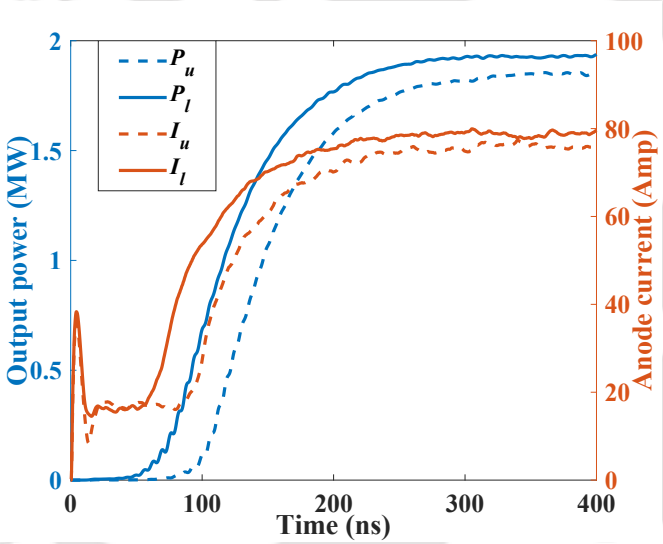

Figure 7.9: The output power and anode current of the *design 1* when either upper or lower cathode is excited at a time.

7.3.2 Output Performance of *design 1* when Only Single Cathode is Excited

As discussed earlier, *design 1* can also be excited with single cathode. For this, either the lower or upper cathode is excited at a time with a DC discrete port. The DC input of 45 kV and 5795 Gauss magnetic field is applied, same as per the previous case. The output performance is obtained from PIC analysis. The output power and anode current obtained from PIC simulation are shown in Fig. 7.9. Here, P_u and I_u are the output power and anode current obtained, respectively, when only the upper cathode is excited, and P_l and I_l are the output power and anode current obtained, respectively, when only the lower cathode is excited. 1.926 MW output power with 53.5% total efficiency and 80 Amp

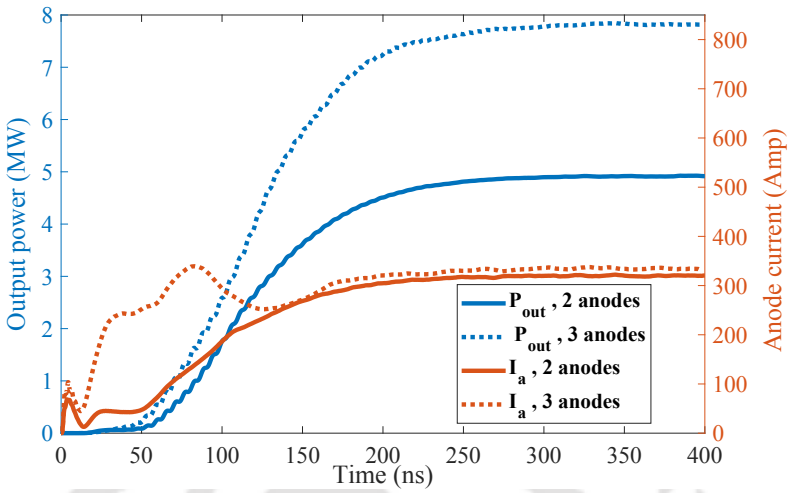

Figure 7.10: The output power and anode current of the *design 2*.

anode current is obtained when only lower cathode is excited. However, when only the upper cathode is excited, 1.85 MW output power is obtained with 54% total efficiency and 76 Amp anode current. Here, the output performances of both single cathode excitations are not same. The difference occurs because of the loading effect of the output waveguide in the output section. The position of the output waveguide is not symmetrical along the length of the coaxial cavity, as shown in Fig. 7.1. Output is taken from the upper half of the outer coaxial cavity through rectangular coupling slot in the cavity wall, so the position of coupling slot is asymmetric along the cavity length.

7.3.3 PIC Simulation of *design 2*

Modified coaxial magnetron configuration for *design 2*, which has two connected cathodes can be excited by one discrete port. The operating point is chosen same, as in the *design 1 i.e.* 45 kV DC voltage and 5795 Gauss magnetic field. The output power of 4.91 MW with a total efficiency of 34.1%, and 320 Amp anode current is obtained for the modified coaxial magnetron with this configuration, as shown in Fig. 7.10. The efficiency of the *design 2* is significantly less than the efficiency of the *design 1*, as anode current of the *design 2* is much higher. However, *design 2* can also house more than two anode resonators and output power can be further improved. In order to demonstrate the same, *design 2* is further extended for three anode resonators and peak output power of 7.8 MW with 52% total efficiency, and 334 Amp anode current is obtained, as shown in Fig. 7.10.

Table 7.2: Performance Comparison of the Proposed *design 1* and *design 2* Coaxial Magnetrons

Parameters	*design 1*	*design 2*
Output power	5.78 MW	4.91 MW
Output efficiency	49.4%	34.1%
Pulse modulator requirements	130 Amp	320 Amp
Multiple output power levels	Three	One
Anode resonators' possibility	Only two	More than two

7.4 Output Performances Comparison of *design 1* and *design 2*

The modified coaxial magnetron with both types of cathode configurations *i.e.* *design 1* and *design 2* are compared, as shown in Table 7.2. *design 1* has an advantage over *design 2* in terms of higher output power and efficiency when two anode resonators are considered in the modified coaxial magnetron structure. *design 1* can be operated in three output power levels: when both cathodes are excited simultaneously, and either lower or upper cathode is excited at a time. However, *design 2* can only have one type of excitation because cathodes are connected and it can have single output power level. The *design 1* requires pulse modulator with 45 kV and 130 Amp current (2 numbers) specifications, while *design 2* requires 45 kV with 320 Amp current specification. However, the advantage of *design 2* over *design 1* is that it can also have more than two anode resonators in stacked configuration, which can produce higher power than two anode resonators, as shown in Fig. 7.10. The proposed modified coaxial magnetron is also tested for three anode resonators in *design 2* cathode configuration. 7.8 MW peak power with 52% total efficiency is achieved with three anode resonators.

Output performances of the proposed *design 1* and *design 2* are compared with the available coaxial magnetrons in Table 7.3. Output peak powers of the proposed modified coaxial magnetrons with double and triple anode resonators are much higher than the conventional coaxial magnetrons with single anode resonator.

Information regarding computational platform, number of mesh cells, emission points, and total time taken in simulations of the proposed modified coaxial magnetrons is given in Appendix D.

Table 7.3: Comparison of the Output Performances of Various Coaxial Magnetrons

Magnetrons	freq. (GHz)	V_a (kV)	B (G)	P_{out} (MW)	η_T (%)	No. of anode resonators
design 1	9.29	45	5795	5.78	49.4	Two
design 2	9.29	45	5795	4.91	34.1	Two
design 2 extension	9.29	45	5795	7.8	52	Three
Lee *et al.* [41]	9.3	36	5900	1.88	53	One
Qiu *et al.* [11]	9.3	41	4800	1.61	50.8	One
L6170 [39]	9.275	38	-	1.75	52	One
VMX3095 [40]	9.3	37	-	1.5	50.6	One

7.5 Summary

A new technique of realizing high-power coaxial magnetron is proposed in which stacked anode resonators are introduced. Power generated from multiple anode resonators are coupled through outer coaxial cavity. This novel technique combines the power generated from multiple anode resonators internally within the device itself and avoids the requirement of external circuitry for power combining. A drastic improvement in the output power of a coaxial magnetron is observed when stacked anode resonators are considered. The modified coaxial magnetron design is proposed based on two cathode configuration: *design 1* and *design 2*. *design 1* has two separate cathode arrangements and can be operated in two different ways: when both cathodes are excited simultaneously, and when either upper or lower cathode is excited at a time.

The output power of 5.78 MW with 49.4% total efficiency and 260 Amp anode current at 9.2906 GHz is obtained when both cathodes are excited simultaneously. In this case, circuit efficiency and electronic efficiency are obtained as of 83% and 59.5%, respectively. Frequency tuning range of 30.5 MHz is achieved from 9.284 GHz to 9.3145 GHz. The output power of 1.926 MW with 53.5% total efficiency and 80 Amp anode current are obtained when only lower cathode is excited, and the output power of 1.85 MW with 54% total efficiency and 76 Amp anode current are obtained when only

upper cathode is excited. The difference in the output performance occurs because of the loading effect of the output section. The position of the output waveguide is asymmetric and it is placed in the upper half of the outer coaxial cavity. *design 2* has two connected cathodes with two anode resonators placed in a stack, and can be excited in only one way. The output power of 4.91 MW with a total efficiency of 34.1% and anode current of 320 Amp are obtained. 7.8 MW peak power with 52% total efficiency, and 334 Amp anode current is obtained when three anode resonators are considered in the modified coaxial magnetron.

design 1 has better output power and efficiency than *design 2* with two anode resonators. The *design 1* can deliver 3 output power levels, while *design 2* has one output power level. However, *design 2* has the possibility for housing more than two anode resonators in the stack, and higher output power can be obtained.

8

Conclusion and Future Work

Contents

In this thesis, the design and analysis of the megawatt-class pulsed power X-band coaxial magnetrons are presented. Overmoded X-band RF windows are proposed for high-power applications. A new method of output power combining is also proposed for magnetrons, in which, the power is combined within the device itself without the requirement of complex external circuitry. This chapter presents a summary of the thesis and discusses the future scopes of extending the works reported in this thesis.

8.1 Thesis Conclusion

An overview of the research carried out and key contributions is as follows:

✓ **A systematic design procedure of the sub-parts of coaxial magnetron**

A design procedure of the primary parts of coaxial magnetron such as a coaxial cavity, anode resonators, output section, mode suppressors are presented. The coaxial cavity is optimized for the maximum Q-factor, which provides mode stability to the desired π-mode. Identification and suppression of unwanted modes such as slot mode and TE_{121} mode are presented. Suppression of the spurious modes is essential for the proper operation of coaxial magnetron.

✓ **Design, output performance analysis and efficiency improvement of X-band coaxial magnetron**

A 28-vane pulsed power X-band coaxial magnetron is designed for high-power applications. Eigenmode analysis of the coaxial magnetron is carried out to determine the mode separation between competing modes and desired mode. The dispersion diagram of the coaxial magnetron is also presented. The Cold test parameters such as Q-factors, circuit efficiency, and coupling coefficient are determined. Output performance is analyzed using particle-in-cell simulation. The maximum total efficiency of 62.04% is obtained at 9.2987 GHz, having 2.12 MW peak output power for stable π-mode operation. π-mode operation is identified by 14 spokes of electrons in PIC simulation. The effects of dielectric constant and loss tangent of the slot mode suppressor on output performance are studied. The frequency tuning characteristics of the magnetron are also analyzed, and the tuning range is obtained as 9.2987 GHz $\pm$ 20 MHz. Total efficiency

is improved by 2.74% by changing the shape of the cathode end hats from conventional to conical.

✓ **Design and analysis of X-band overmoded RF windows**

Four overmoded RF windows are presented in this thesis for high-power applications. Although RF windows are designed here for a coaxial magnetron having 2 MW peak and 2 kW average powers at 9.3 GHz with WR112 output section, RF windows can also be used in various high-power VEDs such as klystron, gyrotron, LINAC. Multiphysics analyses are performed for the RF windows. In these analyses, EM, thermal, and structural analysis are coupled together to analyze the temperature distribution and structural deformation caused by the thermal and mechanical stresses. The mixed-mode operation allows an RF window to operate with broader bandwidth as compared to single-mode operation. Return losses and insertion losses obtained in CST are verified in HFSS, and the results are in good agreement. Sensitivity analysis is also carried out to analyze the effect of mechanical deformation produced by the thermal stress and pressure difference on the performance of the RF windows. Displacement produced is found to be negligible and it doesn't affect the S-parameters considerably. Multipactor analysis is also performed to determine the safe operating power level. Multipactor threshold is determined using SPARK3D.

✓ **A New Approach of High-Power Coaxial Magnetron using Stacked Anode Resonators**

The design of a high-power coaxial magnetron having multiple anode resonators placed in a stacked configuration with two different cathode arrangements is proposed. Output power of the coaxial magnetron can be enhanced significantly by introducing the concept of stacked anode resonators. This ingenious design enhances the output power of a coaxial magnetron without the requirement of complex external circuitry for phase-locking. By using this approach, 272.6% and 368% increments in the output peak powers are achieved with two anode resonators and three anode resonator, respectively as compared to the conventional coaxial magnetron with single anode resonator. The coaxial magnetron design is presented with two different cathode arrangements: with two separate cathodes, and with two connected cathodes. One of the de-

signs has the capability of operating at multiple power levels based on type of excitation chosen. The proposed coaxial magnetron is analyzed using the particle-in-cell (PIC) simulations. The output is taken from a WR112 waveguide.

8.2 Scopes for Future Extension

The possible future research directions in which present work can be extended are listed as:

- ☞ The concept of stacked anode resonators in the coaxial magnetron is proposed for the first time in this thesis. Further investigation is required to enhance the total efficiency of the modified coaxial magnetron system. In the present work, the concept of stacked anode resonator has been verified through simulation studies. Experimental verification of the proposed designs and studying in detail the issues related to practical implementation are major scopes of extending the work.

- ☞ There is a scope of investigation of the coaxial magnetron realization with stacked anode resonators in mm-wave and THz frequencies. Nowadays, mm-wave and THz sources are in high demand for various applications. By using multiple anode resonators, the high output power can be achieved.

- ☞ Modified coaxial magnetron operating in S-band can also be used in Solar Power Satellites (SPS) for Wireless Power Transfer (WPT). Since typically, magnetrons have higher efficiency than klystron, but the phase of the output signal is random, and so, power combining in magnetron array is quite involved. The modified coaxial magnetron doesn't require external circuitry for phase-locking, and power is combined within the device itself. Thus, there is a scope of further investigation of this technique in the S-band, so that the problem of power combining could be solved for Solar Power Satellites (SPS) applications.

- ☞ Although present-day commercial simulators are quite accurate, however, fabrication of the proposed X-band coaxial magnetron, slot mode suppressor, and RF windows are suggested for future work, and reported simulation results can be verified with the measured results.

A

Solution of wave equation for TE_{nsp} mode in coaxial cavity

A. Solution of wave equation for TE$_{nsp}$ mode in coaxial cavity

Wave equation (2.1) can be rewritten in terms of cylindrical coordinate system (ρ, ϕ, z) from [59] as

$$\left[\frac{\partial^2}{\partial\rho^2}+\frac{1}{\rho}\frac{\partial}{\partial\rho}+\frac{1}{\rho^2}\frac{\partial^2}{\partial\phi^2}+\frac{\partial^2}{\partial z^2}+\omega^2\mu\epsilon\right]H_z(\rho,\phi,z)=0. \tag{A.1}$$

Equation (A.1) can be solved by method of separation of variables by writing H_z in terms of ρ, ϕ, and z separately as

$$H_z(\rho,\phi,z)=\boldsymbol{R}(\rho)\boldsymbol{P}(\phi)\boldsymbol{Z}(z). \tag{A.2}$$

Substituting (A.2) into (A.1), expression can be obtained as

$$\frac{1}{\boldsymbol{R}}\frac{\partial^2\boldsymbol{R}}{\partial\rho^2}+\frac{1}{\boldsymbol{R}\rho}\frac{\partial\boldsymbol{R}}{\partial\rho}+\frac{1}{\rho^2\mathbf{P}}\frac{\partial^2\mathbf{P}}{\partial\phi^2}+\frac{1}{\boldsymbol{Z}}\frac{\partial^2\boldsymbol{Z}}{\partial z^2}+\omega^2\mu\epsilon=0. \tag{A.3}$$

Assume,

$$\frac{1}{\mathbf{P}}\frac{\partial^2\mathbf{P}}{\partial\phi^2}=-n^2, \qquad \text{and} \qquad \frac{1}{\mathbf{Z}}\frac{\partial^2\mathbf{Z}}{\partial z^2}=-k_z^2. \tag{A.4}$$

Equation (A.3) can be rewritten as

$$\rho^2\frac{\partial^2\mathbf{R}}{\partial\rho^2}+\rho\frac{\partial\mathbf{R}}{\partial\rho}+\left(k_c^2\rho^2-n^2\right)=0. \tag{A.5}$$

Where, $k_c^2=\omega^2\mu\epsilon-k_z^2$ and n, k_z, k_c are the constants. General solution of the differential equations (A.4, A.5) can be expressed as

$$\boldsymbol{R}(\rho) = AJ_n(k_c\rho)+BY_n(k_c\rho), \tag{A.6}$$

$$\boldsymbol{P}(\phi) = C\cos(n\phi)+D\sin(n\phi), \tag{A.7}$$

$$\boldsymbol{Z}(z) = E\cos(k_z z)+F\sin(k_z z). \tag{A.8}$$

Here, A, B, C, D, E, and F are the arbitrary constants which can be determined by applying boundary conditions. Substituting (A.8) into (A.2),

$$H_z=\boldsymbol{R}(\rho)\boldsymbol{P}(\phi)\left(E\cos(k_z z)+F\sin(k_z z)\right) \tag{A.9}$$

Assume, walls of the cavity are perfect electric conductor. Hence, H_z vanishes at z = 0 and l.

$$\Rightarrow E = 0, \quad \text{and} \quad k_z = \tfrac{p\pi}{l}, \text{ here, } p \text{ is an integer constant,}$$

$$\Rightarrow H_z = \boldsymbol{R}(\rho)\boldsymbol{P}(\phi)F\sin(\frac{p\pi}{l}z). \tag{A.10}$$

Field expressions can be represented for TE mode in terms of H_z from [59] as

$$\begin{aligned} E_z &= 0, \\ E_\rho &= -\frac{j\omega_0\mu_0}{\rho k_c^2}\frac{\partial H_z}{\partial \phi}, & H_\rho &= \frac{1}{k_c^2}\frac{\partial^2 H_z}{\partial \rho \partial z}, \\ E_\phi &= \frac{j\omega_0\mu_0}{k_c^2}\frac{\partial H_z}{\partial \rho}, & H_\phi &= \frac{1}{\rho k_c^2}\frac{\partial^2 H_z}{\partial \phi \partial z}. \end{aligned} \tag{A.11}$$

From (A.10) and (A.11),

$$E_\phi = \frac{j\omega_0\mu_0}{k_c}\left(AJ_n^{'}(k_c\rho) + BY_n^{'}(k_c\rho)\right)\boldsymbol{P}(\phi)F\sin(\frac{p\pi}{l}z). \tag{A.12}$$

E_ϕ vanishes at ρ = a and b, for perfect electric conductor cylindrical surface. This results in a characteristic equation for TE mode of coaxial cavity (2.8). From (A.12, 2.8) and applying boundary condition,

$$\because E_\phi = 0|_{\phi=a} \Rightarrow \frac{B}{A} = -\frac{J_n^{'}(k_c a)}{Y_n^{'}(k_c a)}. \tag{A.13}$$

Cavity has azimuthal symmetry. Either $C = 0$ or $D = 0$, in (A.7). It depends on the excitation of the cavity. In this work, D is chosen as zero.

$$\Rightarrow \boldsymbol{P}(\phi) = C\cos(n\phi). \tag{A.14}$$

Equation (A.6) can be expressed after substituting (A.13) as

$$\boldsymbol{R}(\rho) = \frac{A}{Y_n^{'}(k_c a)}\left[J_n(k_c\rho)Y_n^{'}(k_c a) - J_n^{'}(k_c a)Y_n(k_c\rho)\right]. \tag{A.15}$$

Therefore, complete solution of $H_z(\rho, \phi, z)$ can be expressed as

$$H_z(\rho,\phi,z) = A^{'}\left[J_n(k_c\rho)Y_n^{'}(k_c a) - J_n^{'}(k_c a)Y_n(k_c\rho)\right]\cos(n\phi)\sin(\frac{p\pi}{l}z). \tag{A.16}$$

Substituting (A.16) into set of equations (A.11), remaining fields of TE mode can be determined which is expressed by (2.2-2.7).

A. Solution of wave equation for TE$_{nsp}$ mode in coaxial cavity

B

Calculation of Q-factor for TE_{011} mode of coaxial cavity

B. Calculation of Q-factor for TE$_{011}$ mode of coaxial cavity

Average stored electric energy (W_e) can be expressed in cylindrical coordinates from (2.18) as:

$$W_e = \frac{\epsilon_0}{4}\int_0^l\int_0^{2\pi}\int_a^b \left(|E_r|^2 + |E_\phi|^2 + |E_z|^2\right) r\, dr\, d\phi\, dz. \tag{B.1}$$

Substituting expressions of field components from (2.10) in (B.1)

$$W_e = \frac{\epsilon_0}{4}\frac{\omega_0^2\mu_0^2A_0^2}{k_c^2}\int_0^l\int_0^{2\pi}\int_a^b \left(Z_0'^2\sin^2(\frac{\pi}{l}z)\right) r\, dr\, d\phi\, dz, \tag{B.2}$$

where, $Z_0' = J_0'(k_cr)Y_0'(k_ca) - J_0'(k_ca)Y_0'(k_cr)$

$$\Rightarrow W_e = \frac{\epsilon_0}{4}\frac{\omega_0^2\mu_0^2A_0^2\pi l}{k_c^2}\int_a^b Z_0'^2 r\, dr. \tag{B.3}$$

$\because J_0'(x) = -J_1(x)$ and $Y_0'(x) = -Y_1(x)$, [59],

$$\Rightarrow Z_0' = J_1(k_cr)Y_1(k_ca) - J_1(k_ca)Y_1(k_cr). \tag{B.4}$$

Equation (B.3) can be simplified by substituting (B.4) and following relations [77],

$$\int xJ_1^2(x)\, dx = \frac{x}{2}\left[xJ_0^2(x) + xJ_1^2(x) - 2J_0(x)J_1(x)\right],$$
$$\int xY_1^2(x)\, dx = \frac{x}{2}\left[xY_0^2(x) + xY_1^2(x) - 2Y_0(x)Y_1(x)\right],$$
$$\int xJ_1(x)Y_1(x)\, dx = \frac{x^2}{2}\left[J_0(x)Y_0(x) - \frac{1}{x}J_0(x)Y_1(x) - \frac{1}{x}J_1(x)Y_0(x) + J_1(x)Y_1(x)\right],$$
$$Y_n(x)J_{n+1}(x) - J_n(x)Y_{n+1}(x) = \frac{2}{\pi x}. \tag{B.5}$$

Simplified average stored electric energy can be obtained as:

$$W_e = \frac{\epsilon_0\omega_0^2\mu_0^2A_0^2\pi l}{4k_c^2}\left[\frac{-2}{\pi^2k_c^2} + \frac{b^2}{2}\left[Y_1(k_ca)J_0(k_cb) - J_1(k_ca)Y_0(k_cb)\right]^2\right]. \tag{B.6}$$

Power loss occurs at the two metallic end plates of the cavity and at the two metallic cylindrical surfaces (inner surface, at r = a and the outer surface, r = b). Average power loss can be determined

by solving expression of P_c from (2.19) as:

$$P_c = \frac{R_s}{2}\left[2\int_0^{2\pi}\int_a^b |H_r|^2\, r\, dr\, d\phi + \int_0^{2\pi}\int_0^l |H_z\,|_{\text{at } r=a}|^2\, a\, dz\, d\phi + \int_0^{2\pi}\int_0^l |H_z\,|_{\text{at } r=b}|^2\, b\, dz\, d\phi\right] \quad \text{(B.7)}$$

Substituting expressions from (2.10) and using relation (B.5), (B.7) can be simplified as:

$$P_c = \frac{R_s}{2}\frac{\pi A_0^2}{k_c^2}\left[\frac{4\pi^2}{l^2}\left(\frac{-2}{\pi^2 k_c^2} + \frac{b^2}{2}\left[Y_1(k_c a)J_0(k_c b) - J_1(k_c a)Y_0(k_c b)\right]^2\right)\right.$$
$$\left. + \frac{4l}{\pi^2 a} + lbk_c^2\left[Y_1(k_c a)J_0(k_c b) - J_1(k_c a)Y_0(k_c b)\right]^2\right]. \quad \text{(B.8)}$$

From (B.6, B.8), Q-factor for TE_{011} mode can be determined as expressed by (2.21).

B. Calculation of Q-factor for TE_{011} mode of coaxial cavity

C

Rectangular Waveguide to Cylindrical Cavity Mode Launcher for TE_{011} Mode

Contents

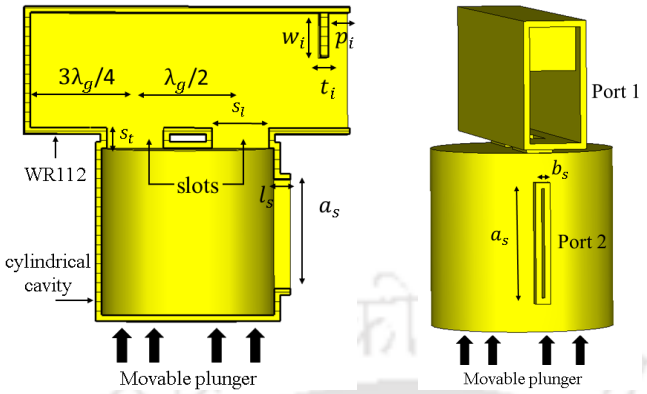

Figure C.1: The proposed mode launcher to excite TE_{011} mode in a cylindrical cavity. (a) An axial cross-section of the mode launcher with design parameters. (b) Side-view of the mode launcher with port definition.

A mode launcher is proposed to excite TE_{011} mode in the cylindrical cavity. TE_{011} mode is excited from the top-wall of the cylindrical cavity from a rectangular waveguide operating in the dominant TE_{10} mode. WR112 rectangular waveguide section is used for this analysis. WR112 section is short-circuited at the one end, as shown in Fig. C.1. Rectangular waveguide is coupled to the cylindrical cavity through two rectangular slots in the narrow wall of the WR112. The dimensions of the coupling slots are represented by slot length (s_l), slot width (s_w), and slot thickness (s_t), as shown in Fig. C.1(a) and Fig. C.2(a). The coupling slots are kept $\lambda_g/2$ distant from each other, here λ_g represents the guide wavelength of the dominant TE_{10} mode in the rectangular waveguide at operating frequency of 9.3 GHz. The position of one coupling slot is $3\lambda_g/4$ distant from the short-circuited end-wall of the rectangular waveguide, as shown in Fig. C.1(a). Such positions are chosen to make electric fields of both coupling slots 180° out of phase. Opposite field directions are needed to excite the desired TE_{011} mode in the cylindrical cavity.

For the impedance matching, an inductive iris is introduced near the input port in WR112 waveguide section, as shown in Fig. C.1. The dimensions of the inductive iris are represented by iris width (w_i) and iris thickness (t_i). The length of the iris is same as the width of narrow wall of WR112 waveguide section. The position of the inductive iris is p_i distance apart from the port 1. p_i and w_i are optimized for fine-tuning of impedance matching. The values of optimized geometrical parameters are presented in Table C.1. Output is taken from the rectangular port, which is defined at the sidewall

Table C.1: Geometrical parameters of the TE_{011} mode launcher

Geometrical parameters	Values (mm)
Slot length (s_l)	14
Slot width (s_w)	3.5
Slot thickness (s_t)	5
Iris width (w_i)	13
Iris thickness (t_i)	2

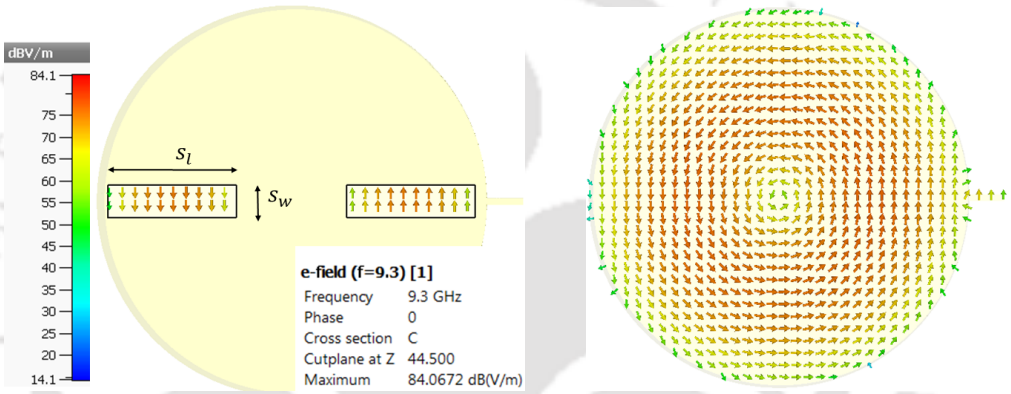

Figure C.2: TE_{011} mode excitation from the mode launcher at operating frequency of 9.3 GHz. (a) E-field pattern at the cross-section of coupling slots. (b) E-field pattern at the cross-section of the cylindrical cavity.

of the cylindrical cavity. In a coaxial magnetron structure, vane resonators present in the anode shell are coupled to the outer coaxial cavity through longitudinal rectangular slots in cylindrical wall of the anode shell, as discussed in chapter 3. These coupling slots are similar to the output port defined as port 2 in Fig. C.1(b). The dimensions of output port (port 2) are chosen in accordance with the dimensions of the longitudinal coupling slots present in the cylindrical anode shell of a typical coaxial magnetron. Geometrical parameters of port 2 are represented by width of the narrower wall (b_s), width of the broader wall (a_s), and the depth of the slot (l_s). The values of b_s, a_s, and l_s are chosen as 0.7 mm, 27 mm, and 4 mm, respectively in this analysis.

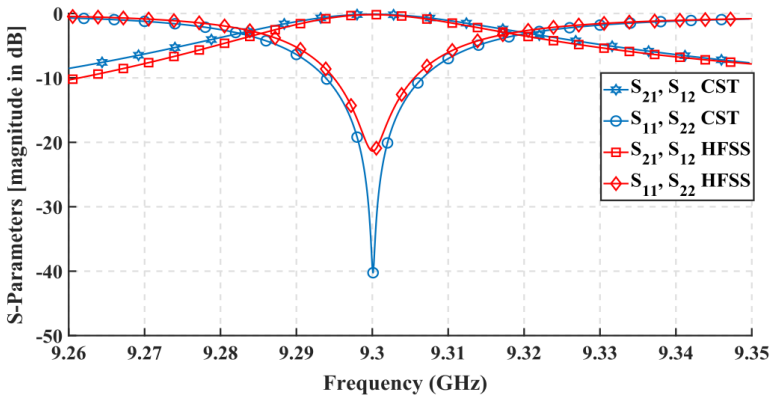

Figure C.3: S-parameters of the TE_{011} mode launcher.

C.1 Simulation Results

In this analysis, input port is taken as port 1, which is defined at the opening of WR112 waveguide section. Port 2 is considered as output port, defined at sidewall of the cylindrical cavity. The simulation is carried out in frequency-domain solver of CST Studio. TE_{011} mode is excited in cylindrical cavity from the rectangular waveguide. The excitation of desired TE_{011} mode is confirmed by observing the electric field pattern at the operating frequency of 9.3 GHz, as shown in Fig. C.2. Here, electric field pattern is shown at the cross-section of coupling slots and cylindrical cavity. Both coupling slots have opposite electric field pattern, as depicted in Fig. C.2(a).

The S-parameters of the proposed top-wall mode launcher is presented in Fig. C.3. S_{11} and S_{21} are obtained as -40.24 dB and -0.12 dB, respectively. Results obtained from CST simulation are compared with the results obtained from HFSS simulation. Return losses are less than 20 dB for both cases at the desired operating frequency of 9.3 GHz. Insertion losses obtained from both solvers are same.

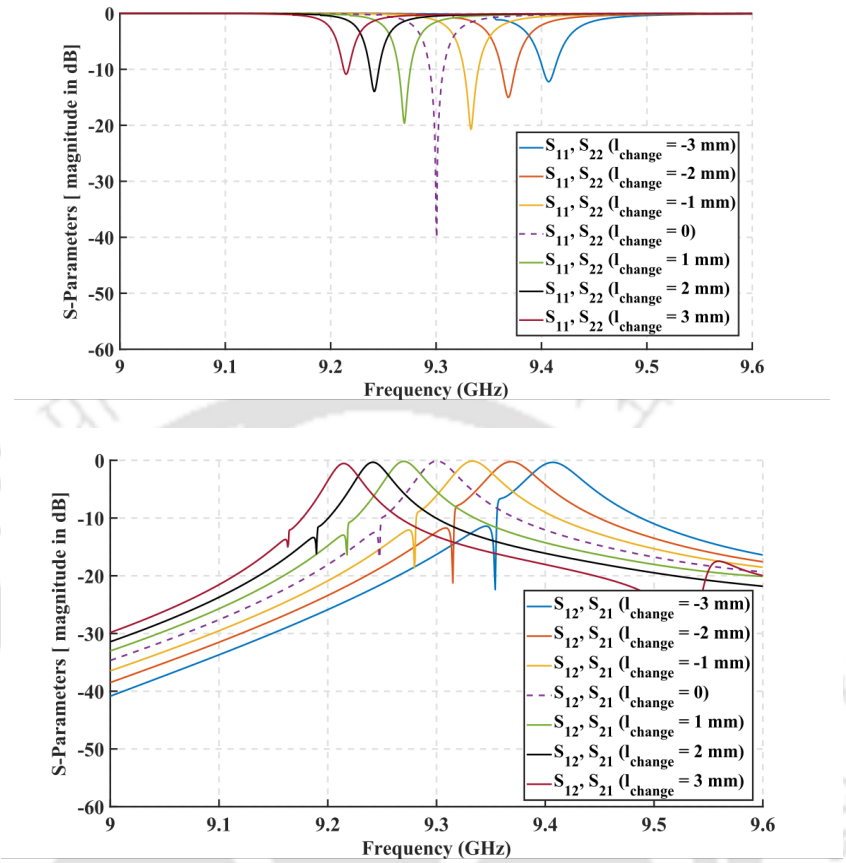

Figure C.4: Effect of the length variation on S-parameters. (a) Tuning of S_{11}, S_{22} parameters. (b) Tuning of S_{21}, S_{12} parameters.

Frequency tuning characteristics of the mode launcher is also studied. Resonant frequency of a cylindrical cavity depends on the cavity length, frequency can be tuned by varying length of the cavity. Since TE_{011} mode has negligible surface current at the junctions of sidewall and end-walls (both top and bottom walls), small perturbation in the length of the cavity doesn't affect the operation of TE_{011} mode of cylindrical cavity. Length of the cavity can easily be varied by employing a movable plunger at the bottom wall of the cavity, as shown in Fig. C.1. The electric field pattern of TE_{011} mode remains unchanged by this small length variation. Effect of frequency tuning by length variation is shown in Fig. C.4. The length of cavity variation is defined by l_{change}. The effect of l_{change} variation is presented for -3 mm to 3 mm in Fig. C.4. The resonant frequency is found to shift inversely with the variation in cylindrical cavity length. It is found that return loss is below 10 dB from 9.213 GHz to 9.413 GHz. The matching gets poor beyond -3 mm to 3 mm variation in l_{change} and fine-tuning

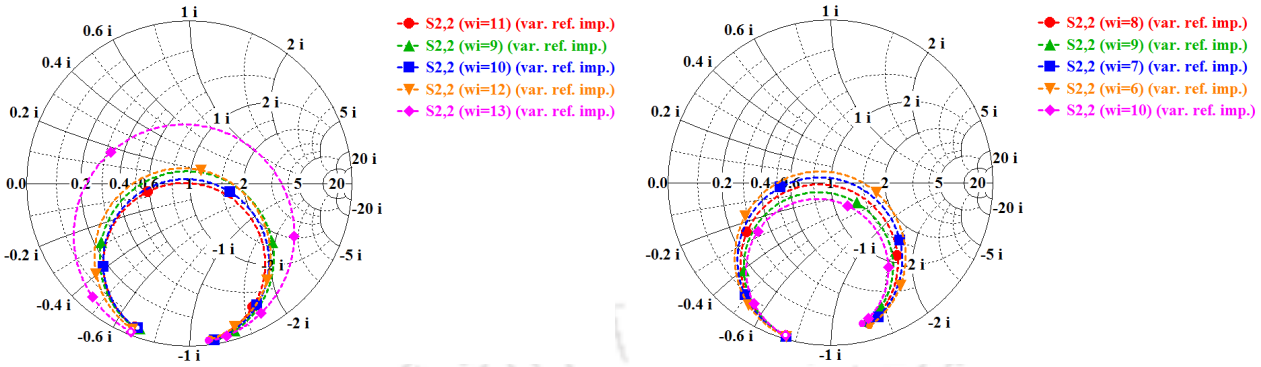

Figure C.5: Effect of the iris width (w_i) variation on S-parameter on impedance Smith chart. (a) Proposed top-wall mode launcher. (b) Conventional sidewall mode launcher.

Table C.2: Comparison of the results of proposed top wall and conventional sidewall mode launchers

Parameters	Proposed launcher	Conventional launcher
Return loss	40.24 dB	36.82 dB
Insertion loss	0.12 dB	0.17 dB
Frequency tunability (l_{change} from -3mm to 3 mm)	200 MHz	180 MHz

of the inductive iris is further required to make the better impedance match after that. The optimal matching is observed at 9.3 GHz.

C.2 Performance Comparison of the Proposed Top-wall Mode Launcher with the Sidewall Mode Launcher

In this section, performance of the proposed top-wall mode launcher is compared with the conventional sidewall mode launcher [78]. The performance comparison is carried out based on the parameters such as return loss, insertion loss, coupling coefficient (β), quality factors, and circuit efficiency (η_C). Proposed top-wall mode launcher has better performance than the conventional sidewall mode launcher [78] in terms of return loss, insertion loss, and frequency tunability as presented in Table C.2. Proposed mode launcher has better tuning range when length of the cylindrical cavity is varied from -3 mm to 3 mm.

Table C.3: Performance of the proposed top-wall mode launcher

w_i (mm)	f_r (GHz)	Lower 3 dB freq. (GHz)	Q_0	Q_l	Q_{ext}	β	η_C (%)
9	9.304	9.286	566.67	261.6	468.07	1.16 (Over coupling)	53.8
10	9.303	9.284	517.9	251.6	489.1	1.06 (Over coupling)	51.4
11	9.3	9.282	516.4	258.2	516.4	1 (Critical coupling)	50
12	9.297	9.282	660.4	299.4	547.9	1.2 (Over coupling)	54
13	9.296	9.280	868.2	277	406.8	2.1 (Over coupling)	68

Identification of the type of coupling is important for any coupler. The coupling can be over coupling, critical coupling, and under coupling based on the value of coupling coefficient (β). For the maximum power transfer from mode launcher to cavity, critical coupling is desired. Coupling type of the mode launchers are determined from the impedance Smith chart, as shown in Fig. C.5. Iris width (w_i) is varied to analyze the effect on coupling type, and S-parameters are plotted on impedance Smith chart for both the mode launchers, as shown in Fig. C.5. The proposed top-wall mode launcher is over coupled for all the shown variations in iris width (w_i), except for w_i = 11 mm (critically coupled and passes through 1), as depicted in Fig. C.5(a). However, conventional sidewall mode launcher is under coupled for $w_i > 8$ mm, over coupled for $w_i < 8$ mm, and critically coupled for w_i = 8 mm. Coupling coefficient (β), circuit efficiency (η_C), loaded quality factor, unloaded quality factor, and external quality factor (Q_0, Q_l, and Q_{ext},) are determined, and are presented in Table C.3 (for proposed top-wall mode launcher) and Table C.4 (for conventional sidewall mode launcher). Proposed top-wall mode launcher has higher Q-factors than conventional sidewall mode launcher at the desired operating frequency of 9.3 GHz.

The performance of top-wall mode launcher is slightly better than the conventional sidewall mode

Table C.4: Performance of the conventional sidewall mode launcher

w_i (mm)	f_r (GHz)	Lower 3 dB freq. (GHz)	Q_0	Q_l	Q_{ext}	β	η_C (%)
6	9.308	9.281	363.37	169.59	318.01	1.14 (Over coupling)	53.32
7	9.302	9.274	342.52	166.11	322.5	1.06 (Over coupling)	51.5
8	9.3	9.271	320.7	160.34	320.7	1 (Critical coupling)	50
9	9.297	9.267	290.89	154.44	329.25	0.88 (Under coupling)	46.9
10	9.294	9.264	277.84	153.37	342.33	0.81 (Under coupling)	44.8

launcher.

C.3 Summary

A mode launcher design is proposed to excite higher order mode, TE_{011} in a cylindrical cavity. TE_{011} mode is excited from WR112 rectangular waveguide section operating in the dominant TE_{10} mode. WR112 waveguide section is coupled to the cylindrical cavity from top-wall through two coupling slots. Excitation of the desired TE_{011} mode is confirmed by observing the electric field pattern in the cylindrical cavity at the operating frequency of 9.3 GHz. Frequency tuning characteristics of the mode launcher is also studied. The resonant frequency is varied from 9.213 GHz to 9.413 GHz by changing length of the cylindrical cavity from -3 mm to 3 mm. Frequency tuning range of 200 MHz is observed. Cylindrical cavity operating in TE_{011} mode can be useful for analyzing and designing the coupling slots between the anode shell and external coaxial cavity in a coaxial magnetron.

D

Computational Information about Simulation

Contents

Table D.1: Simulation Indications (chapter 5)

Magnetrons	No. of mesh cells	No. of emission points	Total simulation time
Coaxial magnetron (chapter 5)	2,512,692	900	10,702 s [2 h, 58 m, 22 s]

Table D.2: Simulation Indications (chapter 7)

Magnetrons	No. of mesh cells	No. of emission points	Total simulation time
design 1	3,781,184	1800	19,464 s [5 h, 24 m, 24 s]
design 2	3,576,639	1800	15,860 s [4 h, 24 m, 20 s]
design 2 extension	4,144,272	2700	20,507 s [5 h, 37 m, 37 s]

D.1 Part A

In this section, computational information of simulation analysis of coaxial magnetron discussed in chapter 5 is presented. For the optimal case (2.12 MW peak power and 62.04% efficiency), computational information including number of mesh cells, number of emission points, and total simulation time are presented in Table D.1. In this analysis, workstation having Intel Xeon Phi processor with 24 GB NVIDIA Tesla K80 GPU, and 512 GB RAM is used to perform simulation.

D.2 Part B

In this section, computational information of simulation analysis of modified coaxial magnetron discussed in chapter 7 is presented. Simulation indications for *design 1*, *design 2*, and *design 2* extension are presented in Table D.2. In this analysis, workstation having Intel Xeon Phi processor with 24 GB NVIDIA Tesla K80 GPU, and 512 GB RAM is used to perform simulation.

E

CAD Designs of RF Windows and Impact of Tolerance for Radius and Position of Coupling Post

Contents

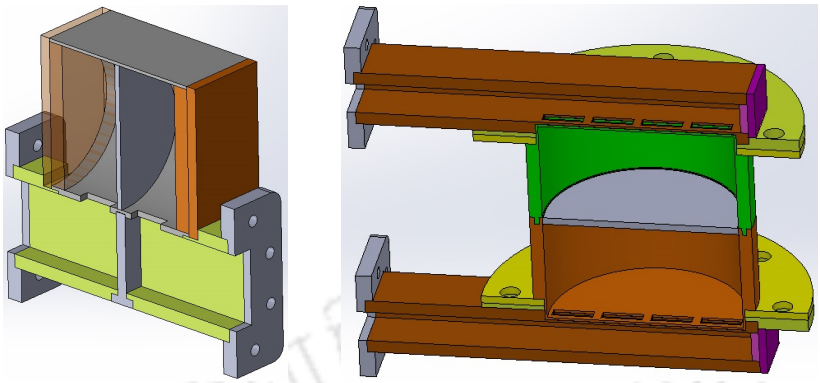

(a) (b)

Figure E.1: CAD design models for fabrication. (a) *design 2*. (b) *design 4*.

Table E.1: Effect of small variation in the radius of coupling post (r_{post})

Change in r_{post}	S_{11} (magnitude in dB)
-0.54%	-42.78
-0.82%	-40.00
-1.48%	-33.20
+0.40%	-40.30
+0.85%	-35.00
+1.30%	-32.00

E.1 CAD Designs of RF Windows

Mechanical designs of the proposed RF windows are prepared and since fabrication and measurement processes are quite involved, it is included in the future work. The CAD design models of two RF windows (*design 2* and *design 4*) are shown in Fig. E.1. CAD models of rest of the proposed windows can also be made for the easy fabrication process.

E.2 Impact of Tolerance for Radius and Position of Coupling Post

Tolerance studies of the radius and position of the inductive coupling post are carried out. Effects of radius and position of the coupling post variation in *design 2* on the return loss are presented in

Table E.2: Effect of small variation in the position of coupling post

Change in position		S_{11} (magnitude in dB)
Δx	Δy	
+0.5%	0	-31.00
-0.5%	0	-34.45
-0.8%	0	-28.10
0	-0.5%	-29.80
0	+0.5%	-30.00
-0.5%	-0.5%	-24.60
+0.5%	+0.5%	-24.40

Table E.1 and Table E.2, respectively. The position of coupling post can be varied by moving it in x and y directions.

E. CAD Designs of RF Windows and Impact of Tolerance for Radius and Position of Coupling Post

Bibliography

[1] R. G. Carter, *Microwave and RF vacuum electronic power sources*. Cambridge University Press, 2018.

[2] A. D. Grigoriev, V. A. Ivanov, and S. I. Molokovsky, *Microwave electronics*. Springer, 2018, vol. 61.

[3] Y. Joo, B.-J. Lee, S.-H. Kim, H.-S. Kong, W. Hwang, S. Roh, and J. Ryu, "Development of new S-band RF window for stable high-power operation in linear accelerator RF system," *Nuclear Instruments and Methods in Physics Research Section A: Accelerators, Spectrometers, Detectors and Associated Equipment*, vol. 866, pp. 1–8, 2017.

[4] "CST Studio 2018," accessed 2019-12-3. [Online]. Available: https://www.3ds.com/products-services/simulia/products/cst-studio-suite/

[5] "MAGIC3D," accessed 2019-12-3. [Online]. Available: https://www.northropgrumman.com/Capabilities/PICCodeSoftware/MAGIC/Pages/About-Magic.aspx

[6] R. G. Carter, "Conceptual design of a 1 MW 175 MHz CW magnetron," in *2009 IEEE International Vacuum Electronics Conference*. IEEE, 2009, pp. 550–551.

[7] T. P. Fleming, M. Lambrecht, and P. Mardahl, "Design and simulation of a megawatt class non-relativistic magnetron," *IEEE Transactions on Plasma Science*, vol. 40, no. 6, pp. 1563–1568, 2012.

[8] T. P. Fleming, M. R. Lambrecht, P. J. Mardahl, and J. D. Keisling, "A high-efficiency megawatt-class non-relativistic magnetron," *IEEE transactions on plasma science*, vol. 40, no. 9, pp. 2112–2118, 2012.

[9] L. Ma, X. Chen, M. Esterson, P. Lindsay, P. Burleigh, and M. Brady, "3D computer modelling of an experimental X band magnetron," in *4th IEEE International Conference on Vacuum Electronics, 2003*. IEEE, 2003, pp. 281–282.

[10] H. J. Kim, J. U. Shin, and J. J. Choi, "Particle-in-cell code simulations on a rising-sun magnetron oscillator," *IEEE Transactions on plasma science*, vol. 30, no. 3, pp. 956–961, 2002.

[11] Q. Jiaqi, C. Huaibi, and T. Chuanxiang, "PIC simulation of the coaxial magnetron for low energy X-band linear accelerators," in *Proc of1st International Particle Accelerator Conference*, 2010, pp. 232–234.

[12] V. D. Naumenko, "Survey of existing designs of millimeter wave band magnetrons," *Radioelectronics and Communications Systems*, vol. 60, no. 4, pp. 141–160, 2017.

[13] A. B. Cutting, *Coaxial versus conventional magnetrons*. The Coaxial Magnetron EMI Varian Booklet, 1971-72.

[14] A. Gilmour, *Klystrons, traveling wave tubes, magnetrons, crossed-field amplifiers, and gyrotrons*. Artech House, 2011.

[15] B. Prokofiev and M. Martynenko, "A simple pillbox-type mixed-mode window for high-power microwave devices," in *Vacuum Electronics Conference (IVEC), 2017 Eighteenth International*. IEEE, 2017, pp. 1–2.

[16] E. Chojnacki, T. Hays, J. Kirchgessner, H. Padamsee, M. Cole, and T. Schultheiss, "Design of a high average power waveguide window," in *Proceedings of the 1997 Particle Accelerator Conference (Cat. No. 97CH36167)*, vol. 3. IEEE, 1997, pp. 3177–3179.

[17] Z. Liu, X. Chen, J. Wan, P. Wu, M. Yang, K. Huang, and C. Liu, "Phase-shifterless power controlled combining based on 20-kw S-band magnetrons with an asymmetric injection," *IEEE Electron Device Letters*, vol. 39, no. 9, pp. 1425–1428, 2018.

[18] R. L. Ives, D. Zeller, G. Lucovsky, E. Schamiloglu, D. Marsden, G. Collins, K. Nichols, and R. Karimov, "Multipactor coating for sapphire RF windows using remote plasma-assisted deposition," *IEEE Transactions on Plasma Science*, vol. 43, no. 8, pp. 2571–2580, 2015.

[19] Y. Saito, S. Michizono, S. Anami, and S. Kobayashi, "Surface flashover on alumina RF windows for high-power use," *IEEE transactions on electrical insulation*, vol. 28, no. 4, pp. 566–573, 1993.

[20] W. Fowkes, R. Callin, E. Jongewaard, D. Sprehn, S. Tantawi, A. Vlieks *et al.*, "Design considerations for very high-power RF windows at X-band," 1998.

[21] W. Fowkes *et al.*, "Reduced field TE_{01} X-band travelling-wave window," in *Proceedings of the 1995 Particle Accelerator Conference (IEEE, New York, 1995) pp*, pp. 1587–1589.

[22] M. Thumm, "MPACVD-diamond windows for high-power and long-pulse millimeter wave transmission," *Diamond and Related Materials*, vol. 10, no. 9-10, pp. 1692–1699, 2001.

[23] R. Heidinger, G. Dammertz, A. Meier, and M. K. Thumm, "CVD diamond windows studied with low-and high-power millimeter waves," *IEEE transactions on plasma science*, vol. 30, no. 3, pp. 800–807, 2002.

[24] E. Jaynes and M. Forrer, "Resonant modes in waveguide windows," *IRE Transactions on Microwave Theory and Techniques*, vol. 8, no. 2, pp. 147–150, 1960.

[25] R. Z. Gerlack, "Small ceramic windows for large waveguides," *Microwave Journal*, vol. 37, no. 11, pp. 110–113, 1994.

[26] H. Obata, H. Miyamoto, and K. Furumoto, "State-of-the-art advanced magnetron for accelerator RF power source," 2017.

[27] S. K. Vyas, S. Maurya, R. K. Verma, and V. P. Singh, "Synthesis and simulation studies of a 10-kW 2.45-GHz CW magnetron," *IEEE Transactions on Plasma Science*, vol. 43, no. 10, pp. 3615–3619, 2015.

[28] A. Bamford, W. Gerard, and C. Scullin, "A 1 MW L-band coaxial magnetron with separate cavity," *IEEE Transactions on Electron Devices*, vol. 14, no. 12, pp. 844–851, 1967.

[29] G. Blanchette, B. Guss, and M. Doherty, "Development of a long life Ka-band inverted coaxial magnetron for use in an airborne military radar system," in *2006 IEEE International Vacuum Electronics Conference held Jointly with 2006 IEEE International Vacuum Electron Sources*. IEEE, 2006, pp. 567–568.

[30] M. Song, T. Hu, Y. Yong, L. Meng, H. Li, and B. Wang, "Tuning characteristics analysis of a Ka-band coaxial magnetron," in *2019 International Vacuum Electronics Conference (IVEC)*. IEEE, 2019, pp. 1–2.

[31] I. Araz, A. Dursun, E. Demirci, E. Korkmaz, and K. Yegin, "Simulation of an 18-vane magnetron in CST-PIC," in *2011 XXXth URSI General Assembly and Scientific Symposium*. IEEE, 2011, pp. 1–4.

[32] T. Isenlik and K. Yegin, "Tutorial on the design of hole-slot-type cavity magnetron using CST particle studio," *IEEE transactions on plasma science*, vol. 41, no. 2, pp. 296–304, 2013.

[33] T. P. Fleming, M. R. Lambrecht, P. J. Mardahl, and J. D. Keisling, "High efficiency, low voltage, low L-band, mega-watt class magnetron," Nov. 4 2014, US Patent 8,878,433.

[34] J.-H. Han, T.-H. Kim, and S.-K. Ryu, "Design of MW-class L-band magnetron with TE_{11} to TE_{10} mode converter," in *2019 International Vacuum Electronics Conference (IVEC)*. IEEE, 2019, pp. 1–2.

[35] A. Cook, J. Drexler, and F. Feulner, "A 1.5 megawatt, high efficiency, X-band CEM* coaxial magnetron," in *1961 International Electron Devices Meeting*. IEEE, 1961, pp. 10–12.

[36] A. C. Johnson, W. A. Gerard, and R. A. Washburn, "Development of a 250 kW, X-band, accusweep magnetron," in *International Electron Devices Meeting 1991 [Technical Digest]*. IEEE, 1991, pp. 601–604.

[37] V. D. Yeryomka and V. P. Dzyuba, "Coaxial cold-cathode magnetron," in *Technical Digest of the 17th International Vacuum Nanoelectronics Conference (IEEE Cat. No. 04TH8737)*. IEEE, 2004, pp. 168–169.

[38] V. D. Yeryomka, M. A. Kopot, P. N. Melezhik, V. P. Dzyuba, and O. N. Tokovenko, "X-band coaxial magnetron with field and secondary emitters," in *2010 20th International Crimean Conference" Microwave & Telecommunication Technology"*. IEEE, 2010, pp. 301–304.

[39] "L6170, L3 Communication," accessed 2019-12-3. [Online]. Available: https://www2.l3t.com/edd/pdfs/datasheets/L6170.pdf

[40] "VMX3095, Communications & Power Industries (CPI)," accessed 2019-12-3. [Online]. Available: https://www.cpii.com/docs/datasheets/291/VMX3095%20FINAL.pdf

[41] J.-H. Lee, G.-J. Kim, S. Kim, Y.-S. Lee, I. S. Kim, and J.-I. Kim, "Investigation of X-band coaxial magnetron using three-dimensional particle-in-cell simulation," in *2019 International Vacuum Electronics Conference (IVEC)*. IEEE, 2019, pp. 1–2.

[42] G. Liu, Y. Song, G. Chen, Y. Zhao, X. Zhang, and M. Xu, "Design and analysis of RF window for a superconducting cyclotron," *IEEE Transactions on Nuclear Science*, vol. 65, no. 9, pp. 2615–2619, 2018.

[43] A. Mikhailichenko, "RF window for high-power in S and X-band," *Nuclear Instruments and Methods in Physics Research Section A: Accelerators, Spectrometers, Detectors and Associated Equipment*, vol. 355, no. 2-3, pp. 645–647, 1995.

[44] Y. Otake, S. Tokumoto, and H. Mizuno, "Design and high-power test of a TE_{11}-mode X-band RF window with taper transitions," in *Proceedings Particle Accelerator Conference*, vol. 3. IEEE, 1995, pp. 1590–1592.

[45] W. Fowkes, R. Callin, E. Jongewaard, D. Sprehn, S. Tantawi, and A. Vlieks, "Recent advances in high-power RF windows at X-band," in *AIP Conference Proceedings*, vol. 474, no. 1. AIP, 1999, pp. 289–295.

[46] S. Tokumoto, Y. Chin, H. Mizuno, K. Ohya, S. Yamaguchi, J. S. Kazakov, R. R. Loewen, R. Fowkes, A. Menegat, A. Vlieks *et al.*, "High-power testing results of the X-band mixed-mode RF windows for linear colliders," *arXiv preprint hep-ex/0008039*, 2000.

[47] O. Lamba, D. Pal, D. Kant, T. Giri, M. Verma, S. Nangru, and L. Joshi, "Design and optimization of asymmetric RF window for 6 MW pulse power S-band klystron," in *2008 International Conference on Recent Advances in Microwave Theory and Applications*. IEEE, 2008, pp. 44–46.

[48] L. Christie and S. Dutta, "Design and comparison of waveguide windows," *Procedia Computer Science*, vol. 93, pp. 243–250, 2016.

[49] Y. M. Jain, P. Sharma, H. V. Dixit, A. Jadhav, and P. Parmar, "Design and multiphysics analysis of a high-power RF window for LHCD system of tokamaks," in *2017 Progress in Electromagnetics Research Symposium-Fall (PIERS-FALL)*. IEEE, 2017, pp. 2888–2894.

[50] T. Treado, P. Brown, T. Hansen, and D. Aiguier, "Phase locking of two long-pulse, high-power magnetrons," *IEEE Transactions on Plasma Science*, vol. 22, no. 5, pp. 616–625, 1994.

[51] A. Dexter, G. Burt, R. Carter, I. Tahir, H. Wang, K. Davis, and R. Rimmer, "First demonstration and performance of an injection locked continuous wave magnetron to phase control a superconducting cavity," *Physical review special topics-accelerators and beams*, vol. 14, no. 3, p. 032001, 2011.

[52] G. Kazakevich, R. Johnson, G. Flanagan, F. Marhauser, V. Yakovlev, B. Chase, V. Lebedev, S. Nagaitsev, R. Pasquinelli, N. Solyak *et al.*, "High-power magnetron transmitter as an RF source for superconducting linear accelerators," *Nuclear Instruments and Methods in Physics Research Section A: Accelerators, Spectrometers, Detectors and Associated Equipment*, vol. 760, pp. 19–27, 2014.

[53] C. Liu, H. Huang, Z. Liu, F. Huo, and K. Huang, "Experimental study on microwave power combining based on injection-locked 15-kW S-band continuous-wave magnetrons," *IEEE Transactions on Plasma Science*, vol. 44, no. 8, pp. 1291–1297, 2016.

[54] Y. Zhang, K. Huang, D. K. Agrawal, T. Slawecki, H. Zhu, and Y. Yang, "Microwave power system based on a combination of two magnetrons," *IEEE Transactions on Electron Devices*, vol. 64, no. 10, pp. 4272–4278, 2017.

[55] T. Hu, M. Song, Y. Yon, B. Wang, H. Li, and L. Meng, "A novel phase-locking structure applied to millimeter-wave magnetrons," in *2019 International Vacuum Electronics Conference (IVEC)*. IEEE, 2019, pp. 1–2.

[56] "ANSYS HFSS 2015," accessed 2019-12-3. [Online]. Available: https://www.ansys.com/products/electronics/ansys-hfss

[57] S. Yue, Z. Zhang, and D. Gao, "3D particle-in-cell simulation of continuous wave magnetron," in *Vacuum Electronics Conference (IVEC), 2016 IEEE International*. IEEE, 2016, pp. 1–2.

[58] S. Yue, Z. Zhang, and D. Gao, "Equivalent circuit method of resonant system of magnetron with sector-and-slot resonant cavities," *IEEE Transactions on Plasma Science*, vol. 42, no. 12, pp. 3968–3974, 2014.

[59] D. M. Pozar, *Microwave engineering*. John Wiley & Sons, 2009.

[60] R. F. Harrington, "Time-harmonic electromagnetic fields," *IEEE press New York*, 2001.

[61] S. M. Rao, "Design and experimental evaluation of the coaxial cavity of circular electric mode magnetron," *Master of Technology dissertation, BHU, Varanasi, India*, 1981.

[62] J. Cochran, "Further formulas for calculating approximate values of the zeros of certain combinations of bessel functions (correspondence)," *IEEE Transactions on Microwave Theory and Techniques*, vol. 11, no. 6, pp. 546–547, 1963.

[63] C. Kou, J. Huang, and C. Tsai, "Experimental study of a slot antenna excited by a TE_{011} mode coaxial cavity," *International journal of infrared and millimeter waves*, vol. 20, no. 5, pp. 897–911, 1999.

[64] J. Feinstein and R. Collier, "Circular electric mode magnetron," *Crossed-Field Microwave Devices, Academic Press, New York*, vol. 2, pp. 123–134, 1961.

[65] G. B. Collins, *Microwave magnetrons*. McGraw-hill Book company, 1948, vol. 6.

[66] S. Y. Liao, *Microwave Devices and Circuits*. Prentice-HallInc, New Jersey, 2002.

[67] T. Berenc and C. Deibele, "Simulation and measurement considerations for resonant cavity couplers and extrapolating results to multiple cells and varying conductivities," *Fermilab RFNote*, vol. 5.

[68] G. Gold and K. Helmreich, "Surface impedance concept for modeling conductor roughness," in *2015 IEEE MTT-S International Microwave Symposium*. IEEE, 2015, pp. 1–4.

[69] M. V. Lukic and D. S. Filipovic, "Modeling of 3D surface roughness effects with application to μ-coaxial lines," *IEEE transactions on microwave theory and techniques*, vol. 55, no. 3, pp. 518–525, 2007.

[70] D. Gamzina, H. Li, L. Himes, R. Barchfeld, B. Popovic, P. Pan, R. Letizia, M. Mineo, J. Feng, C. Paoloni *et al.*, "Nanoscale surface roughness effects on THz vacuum electron device performance," *IEEE Transactions on Nanotechnology*, vol. 15, no. 1, pp. 85–93, 2015.

[71] C. Chua, J. M. Tsai, S. Aditya, M. Tang, S. W. Ho, Z. Shen, and L. Wang, "Microfabrication and characterization of W-band planar helix slow-wave structure with straight-edge connections," *IEEE Transactions on Electron Devices*, vol. 58, no. 11, pp. 4098–4105, 2011.

[72] T. E. Ruden and G. E. Dombrowski, "A field analysis for identification of the spurious modes of the coaxial magnetron," in *Microwave Conference, 1981. 11th European*. IEEE, 1981, pp. 650–654.

[73] J. R. M. Vaughan, "Multipactor," *IEEE Transactions on electron devices*, vol. 35, no. 7, pp. 1172–1180, 1988.

[74] "SPARK3D 2018," accessed 2018-12-24. [Online]. Available: http://www.fest3d.com/spark3d.php

[75] N. Shinohara and H. Matsumoto, "Research on magnetron phased array with mutual injection locking for space solar power satellite/station," *Electrical Engineering in Japan*, vol. 173, no. 2, pp. 21–32, 2010.

[76] N. Shinohara, J. Fujiwara, and H. Matsumoto, "Development of active phased array with phase-controlled magnetrons," in *PROCEEDINGS OF THE INTERNATIONAL SYMPOSIUM ON ANTENNAS AND PROPAGATION JAPAN*, vol. 2, 2000, pp. 713–716.

[77] W. Rosenheinrich, "Tables of some indefinite integrals of bessel functions," *University of Applied Sciences Jena, Jena, Germany*, 2012.

[78] *M. K. Joshi and R. Bhattacharjee, "Design of a rectangular waveguide to cylindrical cavity mode launcher for TE_{011} mode with maximum quality-factor," *International Journal of RF and Microwave Computer-Aided Engineering*, p. e21825.

* Author's own publication

List of Publications

Patent

1. **M. K. Joshi**, R. Bhattacharjee, S. K. Vyas, T. Tiwari "**High-power coaxial magnetron using stacked anode resonators with multi-cathode arrangement**," patent application filed on Dec. 06, 2019, *Indian Patent* 201931050517.

Journal Publications

1. **M. K. Joshi**, S. K. Vyas, T. Tiwari, R. Bhattacharjee, "**Particle-in-Cell Simulation and Analysis of 28-Vane Megawatt-class Pulsed Power Coaxial Magnetron in X-band**," in Special Issue - High Power Microwave Generation - 2020, *IEEE Transactions on Plasma Science*, vol. 48, no. 6, pp. 1886-1893, June 2020.

2. **M. K. Joshi**, S. K. Vyas, T. Tiwari, R. Bhattacharjee, "**A New Approach for High-Power Coaxial Magnetron Using Stacked Anode Resonators**," *IEEE Transactions on Electron Devices* vol. 67, no. 4, pp. 1808-1813, April 2020.

3. **M. K. Joshi**, N. Nayek, T. Tiwari, J. Pidanic, Z. Nemec, R. Bhattacharjee, "**Multiphysics and Multipactor Analyses of TE_{022} Mode High-Power X-band RF Window**," in *IEEE Microwave and Wireless Components Letters*, vol. 30, no. 3, pp. 272-275, March 2020.

4. **M. K. Joshi**, N. Nayek, T. Tiwari, R. Bhattacharjee, "**Design and Analysis of Overmoded RF Window for High-Power Applications in X-band**," *IEEE Transactions on Plasma Science*, vol. 48, no. 1, pp. 127-132, January 2020.

5. **M. K. Joshi**, R. Bhattacharjee, "**Design of a Rectangular Waveguide to Cylindrical Cavity Mode Launcher for TE_{011} Mode with Maximum Quality-Factor**," *International Journal of RF and Microwave Computer-Aided Engineering*, vol. 29, no. 9, pp. e21825, May 2019.

6. **M. K. Joshi**, S. K. Vyas, T. Tiwari, R. Bhattacharjee, "**Optimal Design of a Coaxial Cavity Based on Quality-Factor Maximization for High-Power Coaxial Magnetron in X-band**," *IEEE Transactions on Plasma Science*, vol. 46, no. 3, pp. 503-510, March 2018.

Conference Publications

1. **M. K. Joshi**, T. Tiwari, and R. Bhattacharjee, "**Design and Multipactor Analysis of High Power RF Window**," *20th International Vacuum Electronics Conference (IVEC 2019)* pp 1-2, IEEE, 2019 in Busan, South Korea.

2. **M. K. Joshi**, S. K. Vyas, T. Tiwari, J. Pidanic, Z. Nemec, R. Bhattacharjee, "**Identification and Suppression of Slot Modes in a Coaxial Magnetron**," *Microwave and Radio Electronics Week 2019*, Pardubice, pp 1-5, 2019, IEEE, Czech Republic.

3. **M. K. Joshi**, S. K. Vyas, T. Tiwari, and R. Bhattacharjee, "**Study of High Power X-band RF Window**," in *National symposium on Vacuum Electronic Devices and Applications (VEDA), 2018*. IIT Guwahati, Guwahati, India, 22-24 November, 2018, pp. 1–4.

4. **M. K. Joshi**, S. K. Vyas, T. Tiwari, R. Bhattacharjee, "**Design of Coaxial Cavity for High Power Magnetron**,", *Microwave and Radio Electronics Week 2017*, Brno, Czech Republic, April 19-21, 2017.